

# POLITECNICO DI TORINO

Master's Degree  
in Nanotechnologies for ICTs

Master's Degree Thesis

## Gold-C<sub>28</sub> molecular junction gas sensor: A simulation study



### Supervisors

prof. Graziano Mariagrazia  
prof. Mo Fabrizio  
prof. Piccinini Gianluca

### Candidate

Gullino Davide

Academic Year 2020-2021



# Summary

The purpose of this thesis is the creation of a molecule based system to be used for the detection of gases in the environment. Structures of this kind represent a shift in perspective from industry leading semiconductor based systems towards devices in which the behaviour is strictly connected to the choice of the molecule employed.

In order to gain more insight and to understand the role which may be played in the future by molecular systems, the introductory chapter is envisioned to provide a brief history of standard electronic systems to locate the framework in which molecular ones are placed. The definition of moletronics and the technological advancements, as well as the advantages and disadvantages related to their use, are also presented, along with the particular characteristics required by a sensor.

As far as the concrete portion of the work is concerned, this is divided in two parts: in the first, the theory behind the electronic structure and transport through molecular systems is reported. The idea is to review all the important steps for understanding how the simulations work and how to interpret the results, going from a very simple model, that is based on strong assumptions, to then discuss the equations practically solved by the tools employed, starting from the most general expression of the Hamiltonian of the system and moving to the non equilibrium Green's function approach; in the second, the structure of the system and its behaviour are studied.

In particular, great attention is posed on the analysis of possible geometries believed to be stable, with a systematic approach involving different isomers of the employed molecule, orientations and distances with respect to the electrodes, exploiting the Slater-Koster semi-empirical method. Among the various molecular junctions resulting stable enough one is fixed and used for an in-depth characterization at equilibrium. This analysis allows to validate the goodness of the semi-empirical methods and the ability of the device of changing its properties due to the interaction with other species. Then, the system is brought out of equilibrium in the presence of free air species, allowing to make predictions on some possible pollutants which may be selectively detected and to definitely check the sensing ability of the molecular junction.

In the conclusive part of the thesis the analysis is focused on the interaction

with various dangerous species for human health to search for a possible analyte for the sensor. Moreover, these results are also compared to those of another sensor exploiting a similar molecule, to try finding a common behaviour.



# Contents

<b>List of Tables</b>	VIII
<b>List of Figures</b>	X
<b>Acronyms</b>	XVII
<b>1 Introduction</b>	1
1.1 History of standard electronic systems . . . . .	1
1.2 Beyond Moore . . . . .	4
1.3 Molecular electronics . . . . .	5
1.3.1 Definition . . . . .	5
1.3.2 History of moletronics . . . . .	6
1.3.3 Advantages and disadvantages . . . . .	6
1.3.4 Gas sensor . . . . .	8
1.4 Structure of the work . . . . .	12
<b>2 Simplified model for transport in molecular systems</b>	14
2.1 Review of basics concepts of quantum mechanics . . . . .	15
2.1.1 Free particle in 1D system . . . . .	17
2.1.2 Confinement and bounding box approximation . . . . .	18
2.2 Density of states in quantum confined systems . . . . .	20
2.2.1 Density of states in 2D structures . . . . .	21
2.2.2 Density of states in 1D structures . . . . .	22
2.2.3 Density of states in 0D structures . . . . .	23
2.3 Transport model . . . . .	24
2.3.1 Broadening of levels . . . . .	28
2.3.2 Capacitative model of quantum dot . . . . .	28
2.3.3 Charging effect . . . . .	29
2.3.4 Self-consistent loop . . . . .	30
2.3.5 Gate effect . . . . .	30
2.4 Complete simplified model . . . . .	30

<b>3</b>	<b>Complete description of molecular systems</b>	<b>32</b>
3.1	Wave function based models . . . . .	33
3.1.1	Born-Oppenheimer approximation . . . . .	34
3.1.2	Mean Field Approach . . . . .	34
3.1.3	Hartree model . . . . .	35
3.1.4	Slater determinant . . . . .	35
3.1.5	Variational approach . . . . .	36
3.2	Semi Empirical methods . . . . .	39
3.2.1	Extended Hückel Theory . . . . .	40
3.2.2	Slater-Koster model . . . . .	42
3.3	Density functional theory . . . . .	43
3.3.1	Kohn-Sham scheme . . . . .	44
3.4	Final considerations . . . . .	46
<b>4</b>	<b>Non-Equilibrium Green's Function</b>	<b>48</b>
4.1	Matrix representation of Schrödinger equation . . . . .	50
4.2	Equilibrium analysis . . . . .	52
4.2.1	One contact case . . . . .	53
4.2.2	Additional quantities . . . . .	55
4.2.3	Two contacts case . . . . .	60
4.3	Out of equilibrium analysis . . . . .	60
4.3.1	Density matrix out of equilibrium . . . . .	61
4.3.2	Inflow/outflow . . . . .	62
4.3.3	Landauer-Büttiker . . . . .	63
4.3.4	Effect of voltage on the device . . . . .	64
4.4	NEGF in ATK . . . . .	64
<b>5</b>	<b>System design</b>	<b>66</b>
5.1	Fullerene C <sub>28</sub> . . . . .	66
5.2	Introduction on configuration analysis . . . . .	68
5.3	D <sub>2</sub> symmetry configurations . . . . .	72
5.3.1	Weak coupling configurations . . . . .	73
5.3.2	Strong coupling configurations . . . . .	75
5.4	T <sub>d</sub> symmetry configurations . . . . .	77
5.5	Chosen structure . . . . .	79
<b>6</b>	<b>Free air performance</b>	<b>80</b>
6.1	Clean sensor . . . . .	82
6.2	Performance at equilibrium . . . . .	84
6.2.1	DFT results . . . . .	86
6.2.2	Slater-Koster results . . . . .	88

6.2.3	EHT results . . . . .	89
6.3	Analysis out of equilibrium . . . . .	92
6.3.1	Oxygen molecule induced current variation . . . . .	95
<b>7</b>	<b>Target research</b>	<b>100</b>
7.1	Possible targets analysis . . . . .	101
7.2	Comparison of results with a fullerene C <sub>60</sub> based sensor . . . . .	108
7.2.1	Free air species interaction . . . . .	109
7.2.2	Interaction with pollutants . . . . .	111
<b>8</b>	<b>Conclusions and recommendations</b>	<b>115</b>
8.1	Conclusions . . . . .	115
8.2	Future works . . . . .	116
<b>A</b>	<b>Additional design pictures</b>	<b>119</b>
A.1	D <sub>2</sub> symmetry additional graphs . . . . .	120
A.2	T <sub>d</sub> symmetry additional graphs . . . . .	122
<b>B</b>	<b>Additional free air analysis pictures</b>	<b>126</b>
B.1	DFT settings quick comparison . . . . .	126
B.2	Mulliken population . . . . .	127
B.3	Free air additional graphs . . . . .	129
B.3.1	Van Der Waals spheres . . . . .	129
B.3.2	TS and DOS . . . . .	133
<b>C</b>	<b>Additional pollutants analysis information</b>	<b>138</b>
C.1	Positions of pollutants . . . . .	138
	<b>Bibliography</b>	<b>145</b>

# List of Tables

1.1	Advantages and disadvantages of molecular electronics . . . . .	8
5.1	Device calculator settings. If not specified, default settings have been used. . . . .	70
5.2	Geometry optimization settings. If not specified, default settings have been used. . . . .	70
6.1	EHT settings. If not specified, default settings have been used. . . .	81
6.2	DFT settings. If not specified, default settings have been used. . . .	81
6.3	Average percentage difference between the integrals of the TS of DFT and EHT or Slater-Koster for 2 V of applied voltage, starting from 0.4 V. . . . .	91
6.4	IV curve block settings. If not specified, default settings have been employed. . . . .	93
B.1	Distance of Ar with respect to the carbon atoms of figure B.7. . . .	129
B.2	Distance of CO <sub>2</sub> with respect to the carbon atoms of figure B.7. . .	130
B.3	Distance of O <sub>2</sub> with respect to the carbon atoms of figure B.7. . . .	130
B.4	Distance of N <sub>2</sub> with respect to the carbon atoms of figure B.7. . . .	130
B.5	Distance of H <sub>2</sub> O (O down) relative to the carbon atoms of figure B.7.	130
B.6	Distance of H <sub>2</sub> O (O up) relative to the carbon atoms of figure B.7. .	131
B.7	Average percentage difference between the integrals of the TS of DFT and EHT and Slater-Koster for 6 V of applied voltage, starting from 0.04 V. . . . .	136
C.1	Distance of CO with respect to the carbon atoms of figure B.7, in the case of oxygen pointing downwards. . . . .	138
C.2	Distance of CO with respect to the carbon atoms of figure B.7, in the case of oxygen pointing upwards. . . . .	139
C.3	Distance of NO with respect to the carbon atoms of figure B.7, in the case of nitrogen pointing downwards. . . . .	139

C.4	Distance of NO with respect to the carbon atoms of figure B.7, in the case of nitrogen pointing upwards. . . . .	140
C.5	Distance of NO <sub>2</sub> with respect to the carbon atoms of figure B.7, in the case of nitrogen pointing upwards. . . . .	140
C.6	Distance of NO <sub>2</sub> with respect to the carbon atoms of figure B.7, in the case of nitrogen pointing downwards. . . . .	140
C.7	Distance of CH <sub>4</sub> with respect to the carbon atoms of figure B.7. . .	140
C.8	Distance of the highlighted atoms of figure C.1 (related to C <sub>6</sub> H <sub>6</sub> ) with respect to the carbon atoms of figure B.7. . . . .	141
C.9	Distance of the highlighted atoms of figure C.2 (related to C <sub>7</sub> H <sub>8</sub> ) with respect to the carbon atoms of figure B.7. . . . .	141
C.10	Distance of the highlighted atoms of figure C.3 (related to C <sub>8</sub> H <sub>10</sub> ) with respect to the carbon atoms of figure B.7. . . . .	143
C.11	Distance of PbO with respect to the carbon atoms of figure B.7, in the case of lead pointing down. Notice that the distance of lead is bigger than the one usually employed as its Van der Waals radius is bigger. . . . .	143
C.12	Distance of PbO with respect to the carbon atoms of figure B.7, in the case of lead pointing up. . . . .	143
C.13	Distance of PbSO <sub>4</sub> with respect to the carbon atoms of figure B.7, in the case of lead pointing down. . . . .	144
C.14	Distance of PbSO <sub>4</sub> with respect to the carbon atoms of figure B.7, in the case of lead pointing upwards. . . . .	144

# List of Figures

2.1	Graphical representation of the $k_x, k_y$ plane. The green box is the area occupied by a single state. . . . .	21
2.2	Graphical representation of the $k_z$ plane. . . . .	23
2.3	Comparison of the density of states in 3D (grey line), 2D (red line, notice the energy independent behavior), 1D (green line) and 0D (blue lines). . . . .	24
2.4	Considered system in the case in which the energy of the level is lower (left) or higher (right) with respect to the Fermi level of source and drain. . . . .	25
2.5	Structure under analysis with an applied voltage $V_{DS}$ , creating a bias window (yellow strip). . . . .	26
2.6	Complete structure for the simplified model in a figurative point of view (left) and in the corresponding circuitual representation (right). . . . .	31
5.1	$T_d$ symmetry . . . . .	68
5.2	$D_2$ symmetry . . . . .	68
5.3	Initial configuration for the fullerene placed at 3.36 Å from the nearest gold atom. . . . .	73
5.4	Configuration of the device after relaxation has occurred. Notice the displacement of gold atoms especially in the right contact. . . . .	73
5.5	MPSH relative to the highest occupied system orbital. . . . .	74
5.6	MPSH relative to the lowest unoccupied system orbital. . . . .	74
5.7	MPSH analysis of the structure (zoom on the middle region) . . . . .	74
5.8	Initial configuration with rotated fullerene at 2.20 Å. . . . .	76
5.9	Final configuration after geometry relaxation. . . . .	76
5.10	Initial configuration for the structure with the adatom present. . . . .	76
5.11	Relaxed structure. Notice the elongation of the fullerene. . . . .	76
5.12	Initial configuration with the fullerene at 2.30 Å from gold. . . . .	77
5.13	Final configuration after relaxation. Strong deformation of the contacts occurred. . . . .	77
5.14	<i>MJI</i> junction initial configuration. The Au-C distance is 2.25 Å. . . . .	78

5.15	Structure resulting from optimization. . . . .	78
5.16	<i>MJ2</i> junction initial configuration. . . . .	78
5.17	Final configuration after relaxation. . . . .	78
6.1	Comparison between the DOS at equilibrium evaluated by DFT, EHT and Slater-Koster. Notice that the 0 eV energy level corresponds to the Fermi level. . . . .	82
6.2	Comparison between the TS at equilibrium evaluated by DFT, EHT and Slater-Koster. . . . .	83
6.3	Mulliken population of the sensor (zoom in the middle region) as evaluated by Slater-Koster. Notice the four carbon atoms slightly negatively charged. . . . .	86
6.4	Density of states as evaluated by DFT in the presence of free air species. Notice that the peak at $-1.6$ eV is cut to keep the image comparable to the following ones and to allow a better visualization of the DOS. A complete image can be found in appendix B. . . . .	87
6.5	Transmission spectrum as evaluated by DFT in the presence of free air species. . . . .	87
6.6	Density of states as evaluated by Slater-Koster in the presence of free air species. . . . .	88
6.7	Transmission spectrum as evaluated by Slater-Koster in the presence of free air species. . . . .	89
6.8	Density of states as evaluated by EHT in the presence of free air species. . . . .	90
6.9	Transmission spectrum as evaluated by EHT in the presence of free air species. . . . .	90
6.10	Current flowing as a function of the voltage applied in the presence of external species interacting with the channel using the EHT method. . . . .	93
6.11	Current variations (left) and percentage variations (right) at each bias point in the presence of external species naturally found in the environment. . . . .	95
6.12	Comparison of the transmission spectrum at 1.5 V for the clean sensor and the sensor in the presence of oxygen. The dashed blue vertical line is fixed at $-0.04$ eV, the green one at $0.42$ eV and the yellow one at $0.68$ eV. . . . .	96
6.13	Transmission pathways for $E = -0.04$ eV. Colors are related to the direction of propagation, so that blue arrows represent motion from left to right whereas red ones from right to left. . . . .	97
6.14	Transmission eigenstates at $E = -0.04$ eV for the highest eigenvalue, equal to $2.14e-1$ (left) and the following one, equal to $1.55e-6$ (right), for applied voltage of 1.5 V in the presence of oxygen. . . . .	97

6.15	Transmission eigenstates and pathways at $E = 0.42$ eV for the highest eigenvalue considering the clean sensor (left) and the presence of oxygen (right) for applied voltage of 1.5 V. . . . .	98
7.1	Currents (left) and current variations (right) at each bias point in the presence of carbon monoxide. . . . .	101
7.2	Currents (left) and current variations (right) at each bias point in the presence of nitrogen monoxide. . . . .	102
7.3	Currents (left) and current variations (right) at each bias point in the presence of nitrogen dioxide. . . . .	103
7.4	Currents (left) and current variations (right) at each bias point in the presence of sulfur dioxide. . . . .	104
7.5	Currents (left) and current variations (right) at each bias point in the presence of ammonia. . . . .	105
7.6	Currents (left) and current variations (right) at each bias point in the presence of different hydrocarbons of interest. . . . .	106
7.7	Currents (left) and current variations (right) at each bias point in the presence of lead monoxide. . . . .	107
7.8	Currents (left) and current variations (right) at each bias point in the presence of lead sulfate. . . . .	108
7.9	Currents (left) and current variations (right) at each bias point in the presence of free air species, for the $C_{60}$ based sensor. . . . .	109
7.10	Transmission pathways in the $C_{60}$ sensor for the highest peak in the transmission spectrum, located at 0.4 eV, with 1.4 V of applied voltage and in the absence of external molecules. As usual, colors represent the direction of motion. . . . .	110
7.11	Current variations for NO (left) and $NO_2$ (right) at each bias point for the $C_{60}$ based sensor. . . . .	112
7.12	Current variations for $PbCl_2$ (left) and PbO (right) at each bias point for the $C_{60}$ based sensor. . . . .	113
A.1	Constraints applied during relaxation for all devices in absence of an adatom (left) and in the presence of it (right). The highlighted layers are fixed whereas the others are free to move. Notice that the adatom is free to move as well. . . . .	119
A.2	Position of the gold adatom for the configurations requiring it (the highlighted atom is the adatom, whereas the others belong to the underlying layers). . . . .	120
A.3	Distance between the fullerene and the contacts for the $D_2$ symmetry configuration of figure 5.3. . . . .	120
A.4	Initial geometry with distance of 3.46 Å. . . . .	121

A.5	Final geometry. . . . .	121
A.6	Initial structure with distance of 3.26 Å. . . . .	121
A.7	Geometry after relaxation. . . . .	121
A.8	These configurations are equal to the one of figure 5.3, but with different distances. None of them is expected to be stabler. . . . .	121
A.9	Initial configuration with the fullerene placed at 2.31 Å from the gold contacts. . . . .	121
A.10	Configuration after relaxation occurred. Notice the extreme deformation of the contacts. . . . .	121
A.11	Starting Au-C bond length. . . . .	122
A.12	Final Au-C bond length. Little deformation occurred in the distance. . . . .	122
A.13	Initial extension of the fullerene. . . . .	122
A.14	Final fullerene extension. . . . .	122
A.15	Second <i>MJ1</i> configuration (it is the one of figure 5.14). This is not expected to be a stable configuration. . . . .	122
A.16	Starting configuration for the <i>MJ1</i> system. . . . .	123
A.17	Structure at the end of the relaxation process. . . . .	123
A.18	Starting Au-C bond length. . . . .	123
A.19	Final bond length. Little deformation occurred in the distance. . . . .	123
A.20	Initial extension of the fullerene. . . . .	123
A.21	Final fullerene extension. . . . .	123
A.22	First <i>MJ1</i> configuration. This is not expected to be a stable configuration, due to the great elongation of the fullerene. . . . .	123
A.23	Starting configuration for the system. . . . .	124
A.24	Structure at the end of the relaxation process. . . . .	124
A.25	Initial distance between carbon and gold atoms, set at 2.24 Å. . . . .	124
A.26	The optimized structure suggests an Au-C bonding distance in the order of 10% bigger than the initial one. . . . .	124
A.27	First <i>MJ2</i> configuration. This is not expected to be stabler than the one of chapter 5. . . . .	124
A.28	Au-C distance in the initial configuration (left) and in the final one final (right) for the second <i>MJ2</i> (the one of figure 5.16). . . . .	124
A.29	<i>MJ3</i> junction initial configuration. . . . .	125
A.30	Final configuration after relaxation. . . . .	125
A.31	MPSH analysis of the chosen structure (see figure 5.16) on the first HOSO level (left) and LUSO level (right). A good delocalization is present. . . . .	125
B.1	Comparison of the density of states. The analysis is performed with the sensor in presence of O <sub>2</sub> molecule, to simulate the presence of Van Der waals interaction. . . . .	127

B.2	Comparison of the transmission spectrum. The analysis is performed with the sensor in presence of O <sub>2</sub> . . . . .	127
B.3	Mulliken population analysis with GGA-BLYP functional, PseudoDojo pseudopotential and Ultra basis set settings. . . . .	128
B.4	Mulliken population analysis with GGA-BLYP functional, FHI pseudopotential and DZP basis set settings. . . . .	128
B.5	Mulliken population analysis with HGGA functional, PseudoDojo pseudopotential and Ultra basis set settings. . . . .	128
B.6	Mulliken population analysis as evaluated by Slater-Koster. The result is compatible with the others. . . . .	128
B.7	Schematic of the carbon atoms pentagon. . . . .	129
B.8	Sensor in the presence of Argon (cyan sphere). . . . .	132
B.9	Sensor in the presence of CO <sub>2</sub> (the red spheres are related to oxygen atoms). . . . .	132
B.10	Sensor in the presence of water vapor (hydrogen in light gray, oxygen in red). Notice that the O atom is placed down, whereas hydrogen is up. . . . .	132
B.11	Sensor in the presence of water vapor (hydrogen in light gray, oxygen in red). Notice that the O atom is placed up, whereas hydrogen is down. . . . .	132
B.12	Sensor in the presence of N <sub>2</sub> (blue spheres). . . . .	132
B.13	Sensor in the presence of O <sub>2</sub> . . . . .	132
B.14	Graphical representation of the Van Der waals spheres. . . . .	132
B.15	Comparison of the DOS evaluated by DFT, EHT and Slater-Koster in the presence of external species nearby the sensor. From top left to bottom right: Ar, CO <sub>2</sub> , H <sub>2</sub> O (O down), H <sub>2</sub> O (O up), N <sub>2</sub> , O <sub>2</sub> . . .	133
B.16	Comparison of the TS evaluated by DFT, EHT and Slater-Koster in the presence of external species nearby the sensor. From top left to bottom right: Ar, CO <sub>2</sub> , H <sub>2</sub> O (O down), H <sub>2</sub> O (O up), N <sub>2</sub> , O <sub>2</sub> . . .	134
B.17	Full picture of the free air DOS evaluated by DFT. Notice the peak in the HOSO side. . . . .	135
B.18	Comparison of the integrals of the TS as evaluated by DFT (continued lines), Slater-Koster (starred lines) and EHT (marked lines). Notice the increase in variation starting from 2V. . . . .	135
B.19	Transmission eigenstate at 0.42 eV (zoom on the middle region of the system). . . . .	136
B.20	MPSH for the HOSO state (left) and for the LUSO (right) for the fullerene in the presence of oxygen. Notice how the transmission eigenstate reported in figure B.19 closely resembles the HOSO level of the system. . . . .	137

C.1	Sensor in the presence of $C_6H_6$ (zoom in the middle region). The two highlighted atoms are the ones which distances are provided. . .	141
C.2	Sensor in the presence of $C_7H_8$ (zoom in the middle region). The two highlighted atoms are the ones which distances are provided. . .	142
C.3	Sensor in the presence of $C_8H_{10}$ (zoom in the middle region). The two highlighted atoms are the ones which distances are provided. . .	142
C.4	Current variation for the $C_{60}$ sensor in the presence of hydrocarbons (methane and butane) . . . . .	144



# Acronyms

<b>AFM</b>	Atomic Force Microscope
<b>CNDO</b>	Complete Neglect of Differential Overlap
<b>DFT</b>	Density Functional Theory
<b>DIBL</b>	Drain Induced Barrier Lowering
<b>DOS</b>	Density Of States
<b>EHT</b>	Extended Hückel Theory
<b>EM</b>	ElectroMigration
<b>EUV</b>	Extreme Ultraviolet
<b>FIB</b>	Focused Ion Beam
<b>FCC</b>	Face-Centered cubic
<b>GGA</b>	Generalized Gradient Approximation
<b>HF</b>	Hartree-Fock
<b>HGGA</b>	Hybrid Generalized Gradient Approximation
<b>HOSO</b>	Highest Occupied System Orbital
<b>IC</b>	Integrated Circuit
<b>INDO</b>	Intermediate Neglect of Differential Overlap
<b>IPR</b>	Isolated Pentagon Rule
<b>IRDS</b>	International Roadmap for Devices and Systems
<b>ITRS</b>	International Technology Roadmap for Semiconductors
<b>LCAO</b>	Linear Combination of Atomic Orbitals
<b>LCD</b>	Liquid Crystal Display
<b>LDA</b>	Local Density Approximation
<b>LDOS</b>	Local Density Of States
<b>LGAA</b>	Lateral Gate All Around
<b>LSI</b>	Large-Scale Integration

<b>LUSO</b>	Lowest Unoccupied System Orbital
<b>MCBJ</b>	Mechanically Controllable Break-Junction
<b>MEMS</b>	Micro Electro-Mechanical System
<b>MGGA</b>	Meta Generalized Gradient Approximation
<b>MPSH</b>	Molecular Projected Self-consistent Hamiltonian
<b>MSI</b>	Medium-Scale Integration
<b>NDDO</b>	Neglect of Differential Diatomic Overlap
<b>NEGF</b>	Non-Equilibrium Green Function
<b>OLED</b>	Organic Light-Emitting Diode
<b>PAPR</b>	Pentagons Adjacency Penalty Rule
<b>SCE</b>	Short Channel Effect
<b>SEM</b>	Scanning Electron Microscope
<b>SOI</b>	Silicon On Insulator
<b>SSI</b>	Small-Scale Integration
<b>STM</b>	Scanning Tunneling Microscope
<b>STM-BJ</b>	Scanning Tunneling Microscope Break Junction
<b>TS</b>	Transmission Spectrum
<b>ULSI</b>	Ultra Large-Scale Integration
<b>VLSI</b>	Very Large-Scale Integration
<b>ZDO</b>	Zero Differential Overlap



# Chapter 1

## Introduction

The purpose of this work is the creation, from the theoretical standpoint, of a molecular electronic system. In particular, a molecular sensor will be characterized in all of its parts. Before proceeding I think it is therefore necessary to briefly talk about the motivations which may lead a scientist to the development of such a system, instead of using the already very good devices from standard semiconductor manufacturing, and what molecular electronics refer to. To this end, the present chapter will go through a summary of what have been the most important steps in the industry since the development of the first integrated circuit (IC) to the state of the art devices used nowadays. This is briefly done in section 1.1. Then, in section 1.2, the motivations for looking forward to new technologies are presented, to later introduce the idea behind molecular electronics with an overview of what are the desired characteristics that a molecule-based sensor should have to tackle standard systems, done in section 1.3. Finally, the personal motivations and the structure of the rest of the work are described in section 1.4.

### 1.1 History of standard electronic systems

One of the greatest achievements in humankind recent history has been the development of the integrated circuit. Already in 1959, the idea of employing just one material for the realization of all the useful circuital elements such that they are integrated into the body of the semiconductor material itself was proposed in a patent filed by Jack S. Kilby [1]. While the proposed structure was very different from modern IC, Kilby's invention is considered as the starting point for integrated circuit technologies, and the IC has gained so much importance that Kilby received a Nobel prize in 2000 for his part in the invention of the integrated circuit [2]. Since then, the world has been rapidly upset by the development of new technologies based on the IC.

Through the years, the target of the industry has been to follow Moore's law, a "law" based on observation devised by Gordon Moore in 1965, for which the number of components on an IC doubles every year [3]. While Moore's law has been modified in 1975, with the rate of increase changed to two years (18 months is also a typically referred to period of time) [4], it has been possible to go from the 50  $\mu\text{m}$  technological node, developed during the 1960s, to the most recent 5 nm node, entered in production in 2020 [5]. Notice, in that regard, that the term "technology node" is a way of describing the size of a transistor, usually related to the length of the gate, although recently used with a less precise meaning. In fact, as reported in the 2020 International Roadmap for Devices and Systems (IRDS), the 5 nm node corresponds to the 18 nm technology node definition according to International Technology Roadmap for Semiconductors (ITRS) and IRDS nomenclature [6].

It is important to highlight that, with the passing of years, Moore's law has been interpreted and followed in different ways. As reported in [4], three steps of Moore's law can be highlighted: in the first step (1970s and 1980s) the goal was just to increase the number of components on a chip; in the second step (mid-1990s), the goal was instead to increase the clock speed of devices (of course, higher clock means higher computational power and therefore better performing computing units); in the third step the goal is to increase the number of functional components on the device. Indeed, this third step is strictly connected to the concept of more than Moore, firstly introduced in the 2005 edition of the ITRS as the idea of integrating CMOS and non-CMOS based technologies in a single package with functional characteristics not necessarily scaling with Moore's law [6] [7], where the main purpose is to follow the market demand and develop devices more useful for the final users. Of course, while the second step of Moore's law inevitably ended years ago, due to ever increasing power consumption and heat production, the first step and the third one have been, and are still, followed for the research and development. As far as the first step (usually called more Moore) is concerned, different scales of integration have been reached. In the first years, small-scale of integration (SSI), with 1-10 transistors on a chip, was the standard. Then, medium-scale integration (MSI) with 10-500 transistors, followed by large-scale integration (LSI) with 500-20000 transistors, very large-scale integration (VLSI) with 20000-1000000 transistors and finally ultra large-scale integration (ULSI) where the number of transistors is bigger than 1000000. Currently, devices with billions of transistors are commonly find in CPUs and GPUs available to everyone. How has it been possible to follow such a rapid evolution in technology?

Certainly, all the achieved results would not have been possible without two crucial factors: the great properties of silicon and the technological advancements in the equipment required in the handling of employed materials. As it is very well known, the primary components of an IC are semiconductors, due to their ability of presenting the transistor effect, fundamental for the creation of the CMOS

technology. This means that it is possible to create a device in which the  $I(V)$  characteristic can be tuned by means of two voltages: a gate voltage, able to turn on and off the device, and a drain-source voltage, able to tune the current flowing through the device. This can be made possible by means of a doping mechanism, which modifies the electrical properties of the semiconductor in various portions of the device.

The materials allowed for use are therefore restricted to a very limited number. In particular, looking at the periodic table of elements, group IV (C, Si, Ge, Sn) and group VI (Se, Te) elemental semiconductors can be used, as well as compound semiconductors, made of binary (two elements) or ternary (three elements) combinations of elemental materials, with properties in between the various components. At the beginning of the semiconductor industry, germanium was the preferred choice, as also shown in Kilby's patent. With the passing of time, development and employment of that material stopped in favor of silicon, which, since then, has been the undisputed king for most of the applications.

The reasons for which that has been the case are manifold. First of all, silicon is the second most available material on earth after carbon, which, although being a potential semiconductor, is characterized by a too wide energetic gap between occupied and unoccupied electronic states, thus causing it to behave more as an insulator rather than a semiconductor. Then, silicon can be extracted and processed to create wafers in an efficient fashion, allowing for a reduction of costs associated to the creation of the whole chip. It also presents very good mechanical properties, allowing less risks in its handling. Last, but not least, silicon can be manipulated with ease, especially if compared to other materials. Oxidation and growth of structures on top of a silicon substrate are really what sustain it as the primary choice for most of the applications. In fact, even when the so called short channel effects (SCE), arised, threatening further reduction of scale of devices, the possibility of handling the material building silicon on insulator structures (SOI) and then FinFETs, allowed to overcome the issues, ensuring the predominance of silicon. Furthermore, being able to create a whole system, not just transistors, but also optical devices, interconnects, mechanical sensors and so on on it is really crucial as it both helps reducing the complexity of the creation of the whole structure and the costs associated to it. If every part of a Micro Electro-Mechanical System (MEMS) was to be made of a different material, the technology would be too complex, if compared to a completely silicon based device. Integrability is hence the real power of silicon.

Indeed, while silicon is the main actor, side actors are also responsible for the outstanding research and development leading to ULSI. In particular, the progresses in lithography, leading to the most recent extreme ultraviolet (EUV) tool by LLC [6]; in microscopy, with scanning electron microscopy (SEM) and scanning tunneling microscopy (STM); in deposition and growth techniques; but also manipulation of

structures through piezoelectric materials. The technological results in IC can not be thought without any of these and research also has to be done in these fields.

## 1.2 Beyond Moore

From what has been presented thus far, it may seem that the scaling of devices in standard manufacturing can progress indefinitely, and that silicon is set to be still the primary choice in the future. That's not the case at all. As the dimensions of the transistors are reduced, not only short channel effects related to classical mechanisms, like drain induced barrier lowering (DIBL) and threshold voltage roll-off, occur, but also, and especially, quantum effects. In particular, quantum tunneling represents the biggest constrain in future conventional technologies. In a MOSFET there are two tunneling effects which may happen: tunneling through the gate oxide and direct tunneling from the source to the gate. In both cases, a constant unwanted current contribution is present, which is not really important in the on state, since the contribution is negligible in that condition, but in the off state. As it happens with SCE, the biggest issue is to keep the current flux, and therefore the power consumption, small in that state.

As far as possible solutions to tunneling are concerned, in the case of gate parasitic current, the problem has been solved by changing the materials of the gate stack. As reported in [8], the scaling of CMOS has led to the replacement of silicon dioxide in favor of a physically thicker layer of high dielectric constant oxide such as hafnium oxide. While the details of the solution are not analyzed here, the basic idea is to substitute the  $\text{SiO}_2$  layer of dielectric, which has become too small during CMOS scaling, with new materials which allow for similar performances but with thicker extension, thus lowering the tunneling probability from the channel to the gate contact. Although it has not been a straightforward implementation, mainly for compatibility issues at the silicon interface, that solution is the one still in use today, and allows for great reduction in the parasitic current.

Different is the story of the source to drain tunneling. This phenomenon is caused by a too short channel length. Eventually, electrons are able to travel directly from source to drain without any voltage applied. If this happens, the control over the off state of the transistor is completely lost and the power consumption becomes too high. It is expected that this tunneling effect will be a limiting factor with devices 3nm long, causing the on/off ratio to be too low [9] [10].

As shown, the future of Moore's law does not look so bright, as the further scaling of devices is threatened by quantum effects. Nevertheless, while the nomenclature nowadays suggests that the industry is going to the 3nm node in 2022 (take a look at the 2020 IRDS), Moore's law will still be valid for the next decade if the real dimensions of devices are taken into account [6]. It is important to notice,

however, that the predominance of silicon is coming to an end. As SiGe, with different concentrations of germanium, is expected to be used as the material for the channel until 2025, silicon is expected to be completely replaced by Ge or other materials already in 2028 [6]. The reason for which this is the case is to achieve higher quasi-ballistic velocity and higher mobility with respect to strained silicon [11], although a big challenge is the fabrication of the channel on non-lattice matched silicon, causing the presence of defects. Another interesting idea reported in the IRDS is the one of lateral gate all around (LGAA) and stacked transistors to create 3D structures (LGAA-3D), expected to be the standard at least until 2034, which will allow for an higher number of components per unit volume, thus permitting to follow Moore's law for the foreseeable future.

Indeed, even with these modifications of the channel of MOSFETs, it would be a huge mistake to underestimate the problem of tunneling and, in fact, the IRDS presents a series of new technologies to replace standard CMOS when the limit of scaling is reached.

These take part of the well known idea of beyond Moore. The concept is to go beyond the conventional CMOS technologies in favor of new information processing devices and microarchitectures [11]. Beyond Moore has gained so much attention that an entire section of the IRDS is dedicated in defining and describing all the technologies on the research level taking part of that idea.

The most representative of these technologies is the quantum information processing [6], which not only is based on materials and device structures completely different to the one of a usual CMOS based system, but also on the concept of entanglement, by means of which different qubits (quantum bits) are correlated one to the other. While this technology is not expected to replace standard circuitry, it is nonetheless the primary example of beyond Moore, and what going after CMOS really means. Of course, this is just an example, as there are a lot of new systems, listed in [11], which are still on a research level, that will arrive in the next years, or decades.

## 1.3 Molecular electronics

Until now, molecular electronic systems have not been mentioned. So, what is a molecular electronic system? Where are these structures located within the framework depicted so far? Why are scientists even looking at molecular electronics?

### 1.3.1 Definition

First of all, it is necessary to clearly define what is here intended to be a molecular system. In fact, an important classification has to be made. As reported in [12], molecular electronics can be divided in two different groups: molecular materials for electronics and molecular-scale electronics. The first is related to those devices

in which only the macroscopic properties of the material are exploited. This is usually the case of optical devices, such as liquid crystal displays (LCD) and organic light-emitting diodes (OLED), which are already well established in the industry. The latter is instead focused on the creation of systems in which single molecules, or group of them, are placed in specific position within the device as to exploit microscopic properties of the material. In particular, much of the research activity is focused towards computational architectures which may rival standard electronics [12]. In the viewpoint of this thesis, a molecular electronic system can therefore be described as a system in which the main properties and functionality are dictated by a molecule that is then connected to the rest of the IC and able to communicate with it.

With this idea in mind, it is now possible to justify the reasoning for the research and development of this kind of devices. Indeed, if no advantages are found in substituting typical system with this new concept of molecular-scale electronics, there would be no reasons at all to even think about them.

### 1.3.2 History of moletronics

The first real idea of employing molecules as substitutes of usual solid state devices finds its foundation already in 1974, with the theorization of molecular rectifiers [13], in which an organic molecule is considered to work as a usual p-n junction able to let electrons pass only in one direction. Indeed, the structure is just presented from the theoretical standpoint, due to the technical limitations of the time, but represents a shift of attention in the development of new technologies, not relying anymore on conventional materials. During that period of time (1970s, 1980s) the United States Government's Defense Advanced Research Projects Agency (DARPA) organized a molecular research program focused on the molecular electronics field, also referred to as "moletronics" [14][15]. Thanks then to the development of the STM and of the atomic force microscope (AFM) during the 1980s, the way for measuring transport properties of single molecules was paved [16], thus shining a light of hope in the research. Other important tools, like Langmuir-Blodgett and self-assembly techniques allowed to form organized molecular monolayers on top of suitable substrates [17]. Then, in 1994, the first demonstration of electrical contact of a single  $C_{60}$  molecule occurred [18]. In the successive years, a lot of studies on a huge variety of molecular-based systems were made, like molecular electronic wires, molecular electronic diodes and two-terminal electrical switches [19].

### 1.3.3 Advantages and disadvantages

While the idea itself of creating molecular electronics is appealing, as anticipated earlier there should be some reasons for justifying their use with respect to standard

technology.

As pointed out in [12] [20], the main advantages of molecule-based systems are related to the intrinsic characteristics of molecules, such as the dimensions and the ability to self-assemble with a bottom-up approach. Of course, in the viewpoint of reducing the size of electrical components in IC, the dimensions of molecules really interest scientist as Moore's limits are approaching. Systems with channel length in the order of a nanometer, without losing control over the on or off state of the system and with transport properties that are more predictable if compared to similarly sized traditional MOSFETs, are possible [21]. This also allows for a huge increase in device density, with up to  $10^{13}$ - $10^{14}$  devices on  $1\text{ cm}^2$  with 1-3 nm sized molecules [12]. The self-assembly property, compatible with usual CMOS processes [22], then, is crucial in order to overcome one of the major issues related to standard technologies, that is the complexity of creating and developing technological processes able to tackle the reduction of the size of devices. For molecules, once the synthesis method is known, industrial scale production is not an issue, with up to  $10^{23}$  molecules per beaker [23] [24]. Another great attribute is the possibility of tuning with ease optical, electrical and structural properties by changing chemical composition and geometry [21], potentially observing novel phenomena not accessible from standard materials [24].

Unfortunately, despite all of these very interesting characteristics, employing molecules is not as simple as it may have appeared from the previous discussion, and in fact molecular electronics are far from being widely employed. As reported in [16], the creation of single-molecule electronics is a combined effort from different branches, all of which face different challenges. In particular, the main issue is the variability related to the creation of the region of space in which the chosen structure will ultimately be inserted, that is the nanogap. While, in fact, as previously pointed out, the synthesis of multiple molecules is not a problem, that is not the case for the rest of the device. The control at nanoscale is required, as well as extreme precision in the creation of the contacts. Although through the years several methods, like mechanically controllable break junction (MCBJ), electromigration (EM), STM breakjunction (STM-BJ) and focused ion beam (FIB) (an in depth analysis of most of the developed and studied techniques for the creation of nanogaps can be found in [24]) have been introduced and studied both from the theoretical and experimental point of view, the yielding ratio of structures with the desired geometrical features is still quite poor, thus not allowing a widespread distribution of molecule-based systems. Even small variation in single processes can lead to huge changes in the final system [24]. Aging of the molecule can also be an important factor for reproducibility. Therefore, it seems like some time is still needed to reach very high yield fabrication and widespread diffusion [24].

Another disadvantage of using molecules is the requirement of using complex tools

for simulations, meaning an higher computational cost and therefore slower research and development. In fact, the theory behind current transport through molecules comes from the famous Non Equilibrium Green's Function (NEGF) approach, which allows for great agreement between calculations and experiments [16], at the cost of simulation tools that are quite expensive from the computational standpoint. To summarize the advantages and disadvantages, in table 1.1 all of the discussed properties are summed up.

**Table 1.1:** Advantages and disadvantages of molecular electronics

<b>Advantage</b>	<b>Description</b>
Scalability	with respect to standard CMOS devices, way smaller structures are possible.
Cost	thanks to self-assembly technique, the cost for the synthesis of a huge number of molecules is low.
Tunability	an extreme variety of properties can be obtained by changing geometry and composition of molecules.
<b>Disadvantage</b>	<b>Description</b>
Handling	it is complex to create the whole system, requiring an high precision to control the final position of the molecule.
Variability	there is still not a process able to produce a great number of systems with the same properties.
Simulation	high computational cost required to model transport.

Before moving on, notice that it is beyond the purpose of this work to go into the details of the creation of the nanogap and therefore in the following chapters a structure with ideal desired characteristics will be employed. This does not mean, however, that the necessary attention will not be given to the way the chosen molecule will link itself to the contacts. Indeed, various orientation and distances between source, drain and channel will be considered to find out which ones are the most likely to occur from the energetic point of view.

### 1.3.4 Gas sensor

As previously anticipated, the goal of this work is the design and analysis of a molecule-based sensor. In this section the characteristics required for such device are described, starting from the general working principle and properties of a sensor,

to then move to the specific case of a molecular one.

The purpose of a sensor, here assumed to be a gas sensor, is to detect the presence of a specific molecular species in the environment. This species is usually referred to as being the analyte. Thanks to the Brownian motion of particles, it is possible that the target gets close to a part of the device, called sensing region, producing the so-called sensing effect. This means that the presence, or not, of the analyte is verified by means of the interaction with the sensor, that in turn causes a variation of the properties of the device itself. The process by means of which the interaction is transformed into a measurable signal is called transduction, and depending on the design it can be of different nature. Typically, the transduction occurs as a variation in the conductance of the conducting region of the sensor, and is therefore of electrical nature. Focusing on the interaction, instead, in the viewpoint of this work it is assumed to be due to Van Der Waals forces and is hence of physical (electrical to be more precise) nature, but in a general case scenario also a chemical bonding may occur. In both cases, however, what is expected is a modification in the channel conductance.

As far as the characteristics of the system are concerned, as for any experiment regarding the measurement of a quantity (in this case the concentration of species in a certain environment), the final device should be able to provide results that are repeatable, meaning that, using the same measuring procedure, user, conditions and instrument, the values provided have to be similar, and reproducible, meaning that, employing different procedures, users, conditions and instruments, compatible results are once again obtained. These two properties are included in the concept of measurement precision. Furthermore, it is crucial for the system to be accurate, in the sense that it is expected to give measurements that are close to the effective value of the quantity to be evaluated (it is not just important to know a specific species is present in the environment, but it is also crucial to know its concentration, especially for those cases in which there is a certain threshold dictated, for example, by specific laws).

While the just introduced characteristics are general for any system of measure, there are then others that specifically apply to the case of a sensor. Focusing on that case, since the requirement is to detect a specific molecule, selectivity is the main property the sensor must have, which means that the sensing mechanism should give an output which allow to distinguish between the analyte and possible other species present.

The second property to consider is the resolution of the system, which is, practically speaking, a measure of the smallest amount of variation in the concentration of the target that can be detected by the sensor. A small value of resolution indicate that the device is able to detect small variations of the analyte. Strictly connected to this quantity is the discrimination threshold, which is the maximum value of the measurand that does not produce a variation in the output. The smaller it is,

the better is the ability of detecting small concentrations and hence the quality of the device. Indeed, in most cases, the concentration of the analyte with respect to other species is small, therefore requiring the sensor to be able to detect very small concentrations.

Then, it is important to know the sensitivity of the device, which is a measure of the change in output of the sensor relative to a unit change in the input.

On the other end of the spectrum, when the concentration of the target is high, the sensing effect should not be saturated with a large number of molecules. In that sense it is said that the dynamic range should be high enough [25][26]. While this is true, it is also expected not to be something which can possibly occur, if the intended use of the sensor is to detect species that are not meant to be present in a huge amount. In that case, if the saturation of the system occurs, it means that the goal of the device has been fulfilled and that the analyte is present in the environment with a concentration exceeding the desired threshold. At that point is not really important the exact amount of that species.

All of these properties, in order for a molecule-based sensor to be considered valuable, must be verified and comparable, if not better, with respect to standard systems. It is important to notice, however, that some of them need experimental validation. In particular, repeatability and reproducibility are dependent on the possibility of realizing the sensor and produce multiple measurements in order to finally compare the data. Also the accuracy of the system, as well as the resolution and the discrimination threshold, depends on practical implementation. As such, these properties, in the viewpoint of this work, could not be verified and analyzed. The analysis of the following chapters is, in fact, just theoretical, meaning that the sensor could not be physically realized. Nevertheless, the main purpose of the sensor developed in the following is not to be able to produce state of the art results. What is of interest, in fact, is the possibility of creating a molecule-based sensor to see if the selectivity with respect to specific species is verified or not. Indeed, as previously indicated, the realization of molecular electronic systems is still at an early stage, and it would be presumptuous to expect a full characterization for a system that, practically speaking, is years in advance of what the technology could be possibly pulling off. In that regard it is also justified the choice of treating a sensor instead of, for example, a transistor. While the application and employment of transistors requires the ability of creating billions of them with the same characteristics and at the same time for the construction of a fully working system, for sensing applications way smaller number of devices are required, and there is no need to produce all of them at the same time.

As far as the sensing effect is concerned, the working principle of a molecule-based sensor is very similar to that of a standard sensor. The expected phenomenon is the variation of the conductance, and so of the current, of the device, due to the interaction of a part of the structure with external species. In both standard and

molecular applications, this process occurs in the channel between the two contacts. What is different, of course, is what this region is made of. The novelty, in the case under study, is really in this part, with the conducting channel being made of a molecule. In this introduction, the molecule of choice is not really important (it will be analyzed in depth in chapter 5). What matters is that it is expected that, whatever this choice is, a modification of the conductance occurs. While the specific characteristics of this variation are studied in depth in chapter 6, it is here possible to make some predictions.

As earlier mentioned, one of the advantages related to the use of molecules is the tunability. That characteristic comes very handy in the purpose of developing a sensor with high selectivity. Indeed, the nature of the interaction between molecules is strictly related to the species involved. Therefore, it is reasonable to think that the great power of molecule-based sensor is the possibility of choosing, accordingly to the needs, a specific analyte with respect to which a good selectivity occurs. Obviously, things are not that easy, in the sense that is not straightforward to find what the best choice for the channel is *a priori*, and therefore further analysis are required.

Also the accuracy and the precision should be quite good for molecular systems, especially if the interaction is of physical type and not chemical, meaning that the structure of the channel is not chemically modified by the event and so recovers the initial conductance once the species is removed from its surrounding region. As a consequence, multiple measurements are expected to give the same results and, if the systems is calibrated in the corrected way during its creation, such results should be similar to those made by other instruments.

Different is the case for the resolution, the discrimination threshold and the sensitivity. In fact, since the concentration of the target may be low if compared to the one of other particles, and since the channel is small, due to the intrinsic size of molecules, it may be hard to observe a sensing event, therefore causing a possibly poor discrimination threshold. Furthermore, even if that event occurs, it is unlikely to have multiple particles of the same type in the sensing region together, suggesting also a bad resolution and sensitivity. However, will this is true, a possible workaround consists in employing multiple wires together. In that case, if the properties of such wires are comparable, the problem can be partially, or completely solved.

A final consideration has also to be made in the variation of the output. Molecules are intrinsically small, and as such, if used in a wire configuration, may cause the current flowing through the structure to be quite low. It is therefore reasonable to expect the variation of it to be small and, possibly, smaller than the quantity effectively detectable by standard circuitry. As a consequence, a big problem may involve the sensitivity and the selectivity of the sensor, in the sense that the variation caused by the target may not be detectable with respect to the case in

which no particles are present in the region surrounding the channel. Again, this issue may be tackled by designing, with a more complex overall structure, the rest of the IC to which the sensor is connected to. Of course, if the difference is too small, or too similar, to the one produced by other species, it may be due to the sensor not being at all selective, and nothing can be done in that case.

## **1.4 Structure of the work**

Through this introduction, an overview of the history of standard electronic systems, from the first integrated circuits to more recent devices, has been presented. The concept of molecular electronic systems and the particular characteristics required by a sensor of this kind have also been introduced.

To conclude this chapter, the present section has the purpose of illustrating the structure of the rest of the thesis as well as the personal motivations for the choice made.

Approaching the end of the master's degree, semiconductors were dominating materials in almost all the state of the art systems presented. From photonic devices, like lasers, amplifiers, modulators and waveguides, to FinFET transistors, the first materials of choice were always semiconductors.

In this sea of structures, the idea of exploiting molecules never really crossed my mind, until I stumbled in molecular electronic systems presented in one of the last courses. The change of paradigm, from top-down methods to bottom-up ones, for the creation of devices, made me imagine about the huge variety of systems which could have been made possible with such building blocks.

It all seemed so reasonable, simple and intuitive. As molecules can be easily synthesized, the problems regarding the scaling of standard devices were not issues anymore and with the great tunability permitted creativity was the only limit in the design.

Indeed, I imagined things to be easier than they actually were and molecular systems are still far from being widely distributed. However, the idea of working with very different systems with respect to what I was used to stuck in my head. This led to the choice of focusing, in this thesis project, on a molecule-based sensor, starting from the theory by means of which they are described to then engineer the final system and study it in depth using different simulation tools.

As far as the structure of the rest of the work is concerned, in chapter 2 a simple model for the description of transport in molecular systems is presented. Of course, the theoretical modelling of how a certain device work is the primary step in order to correctly set up simulations and understand the results. This chapter truly represents an oversimplified view which is however capable of providing a little insight on the results obtained. All the topics here discussed are expected to be a

well known background for students coming from a degree in nanotechnologies for ICTs, so most of the elements are not justified nor presented.

In chapter 3, a more refined theory for understanding the electric structure of devices in absence of external stimuli is developed. All the steps for the description of the simulation tools used in the work are followed, from the formulation of the complete Hamiltonian of the system to the final set of equations practically solved. In this part most of the settings employed in the next chapters are also justified and described.

Then, the final, and more complete with respect to the one of chapter 2, model of transport in molecular systems is presented in chapter 4. Again, in the viewpoint of providing just the necessary theoretical results, this chapter is not intended to give a rigorous description.

Moving on to the practical part of the work, in chapter 5 the fullerene  $C_{28}$  is considered for an in depth analysis on possible structures for the molecular junction expected to work as a sensor. This is a crucial part for the design of the system as the behavior of it is strictly dependent on its geometry.

Once the structure has been found and fixed, in chapter 6 it is deeply analyzed in equilibrium and out of equilibrium conditions in the presence of species found in the atmosphere. This chapter proves the sensing ability of the employed molecule as well as the validity of less precise semi-empirical tools with respect to more precise ones.

Finally, in chapter 7 the study on possible targets for the sensor is performed. Moreover, the system is compared to a similarly developed and conceived gold- $C_{60}$  molecular junction based sensor to try finding a connection in behaviour of molecular sensors exploiting fullerenes.

## Chapter 2

# Simplified model for transport in molecular systems

One of the complexities of employing molecules instead of crystals is the difficulty of modeling how electron transport and in general electrical properties work in such structures. A good start in this viewpoint is to begin with a simple model which allows to understand at a basic level what the differences are with respect to studying a typical semiconductor-based system.

The present chapter arises exactly to fulfill this goal, with the description of a very approximated, and not rigorous at all, model. Indeed, it is neither complete, in the sense that a lot of elements herein used are assumed to be known, nor precise, in the sense that its purpose is not to analyze things from a rigorous standpoint. Nevertheless, it is able to catch a lot of what is discussed in the following chapters. The material of this part has been entirely extracted from personal notes taken in the "Physics II", "Quantum Physics" and "Nanoelectronic Systems" courses held in Politecnico di Torino respectively by professors Fabrizio Pirri, Vittorio Penna and Mariagrazia Graziano.

In section 2.1, a brief introduction to quantum mechanics is presented. Notice that, since the goal of this work is not to give an all-encompassing analysis of all the topics related to the study of transport in molecule-based devices, but just to give the basics required for the comprehension of the simulation tools employed and the inspection of the results given by them, only strictly necessary concepts are explained and analyzed thoroughly not only in this simplified model but also in the more complete one of the following chapters.

In section 2.2, the density of states for nanoscopic systems is analyzed, going from 3D to 2D, 1D and finally 0D systems, like the one of a molecule.

Finally, sections 2.3 and 2.4 focus on the complete simplified model for the analysis of transport.

## 2.1 Review of basics concepts of quantum mechanics

Classical mechanics is not suited for the analysis of nanoscale problems. In fact, at the beginning of the twentieth century there were some unsolved problems, like the very well known black body radiation, photoelectric effect, the radiation pressure and the electron diffraction which could not be solved with a classical approach. First of all, to find a solution for the radiation pressure and the electron diffraction, De Broglie proposed the concept of wave-particle duality for electrons, allowing to describe their diffraction by a crystal, and for photons, thus justifying the mechanical pressure caused by an electromagnetic wave impinging onto a structure. Together with Einstein, the wave and particle worlds were theorized to be linked together by means of:

$$\lambda = h/p$$

where  $h$  is a quantity, called Plank constant, used to solve the issues of black body radiation and photoelectric effect, where emitted energies and electromagnetic spectrum were quantized, thus introducing for the first time the concept of discretization of energetic levels and hence of physical quantities.

Starting from these two concepts, wave-particle duality and quantization, a shift from the conventional way of analyzing the world by means of classical mechanics started. The new way of approaching the world was called quantum mechanics. Since in this viewpoint the wave and particle natures are linked together, it is necessary to find a way of representing and describing a system. In particular, in quantum mechanics it is assumed that electrons can be described by wave functions which, in the particular case of free electrons, are simple plane waves of the form:

$$\psi(\vec{x}, t) = Ae^{i(k\vec{x}-\omega t)} \quad (2.1)$$

with the wave vector expressed as:

$$k = 2\pi/\lambda$$

While the meaning of  $\psi$  can not be easily described, it is well known that its magnitude squared gives the density of probability of finding an electron in a specific position and moment of time:

$$|\psi(\vec{r}, t)|^2 = \rho(\vec{r}, t) \quad (2.2)$$

Indeed, if a single electron is considered, the integral of  $\rho$  over the whole space is equal to 1, and so the meaning of the constant  $A$  in equation 2.1 is to provide a normalization constant ensuring that this is really the case.

Together with the concept of wave functions, another crucial point in quantum mechanics is the Schrödinger equation, which allows to study the time evolution of the system under analysis:

$$i\hbar \frac{\partial \psi(\vec{r}, t)}{\partial t} = V(\vec{r}, t)\psi(\vec{r}, t) - \frac{\hbar^2}{2m^*} \Delta \psi(\vec{r}, t) \quad (2.3)$$

where the potential and kinetic terms on the right hand side are typically put together to form the Hamiltonian  $H$  of the system, which represents the total energy of the structure under analysis:

$$i\hbar \frac{\partial \psi(\vec{r}, t)}{\partial t} = \hat{H}\psi(\vec{r}, t)$$

Notice that the quantization of physical properties of the system is directly embedded within Schrödinger equation in the case in which boundary conditions are applied. This will be clearer in the following.

In typical applications of Schrödinger equation, the presence of electromagnetic waves is neglected, thus causing the potential term in 2.3 to be time independent. Since also the kinetic term is time independent,  $\psi(\vec{r}, t)$  can be factorized in the product between space and time dependent terms:

$$\psi(\vec{r}, t) = R(\vec{r})T(\vec{t})$$

It can be proved that the general solution has the form:

$$R(\vec{r})T(\vec{t}) = Ae^{-i\frac{E}{\hbar}T}R(\vec{r})$$

where the time related term is fixed. Traditionally:

$$R(\vec{r}) = \psi(\vec{r})$$

Rewriting 2.3, one gets:

$$\hat{H}\psi(\vec{r}) = E\psi(\vec{r}) \quad (2.4)$$

$$-\frac{\hbar^2}{2m^*} \Delta \psi(\vec{r}) + V(\vec{r})\psi(\vec{r}) = E\psi(\vec{r}) \quad (2.5)$$

This is usually referred to as the steady state Schrödinger equation. It is an eigenvalue problem which allows to evaluate the eigenfunctions (the wave functions) and the eigenvalues, that is to say the set of possible energy values that can be assumed by the system. Ideally, if one is able to describe the system under analysis

with a complete Hamiltonian, meaning that all the kinetic and potential energy terms are known, solving 2.3 allows to get all the energy values as well as wave functions of the system, therefore obtaining a full description of everything related to the system itself. In practice, it is impossible to build the Hamiltonian and solve 2.5 even for small systems, and so various approximations are used. A typical approach for the analysis of a system is to suppose that the 3D potential term can be separated and considered as the sum of 1D independent contributions. Exploiting the linearity of the Hamiltonian, 2.5 becomes:

$$(\hat{H}_x + \hat{H}_y + \hat{H}_z)\psi_x(\vec{x})\psi_y(\vec{y})\psi_z(\vec{z}) = (E_x + E_y + E_z)\psi_x(\vec{x})\psi_y(\vec{y})\psi_z(\vec{z}) \quad (2.6)$$

The concept of separation of variables is crucial to tackle most practical problems, and will be widely used in the following.

### 2.1.1 Free particle in 1D system

The purpose of this part is to justify in a qualitative way why the wave function of a free particle has been previously introduced to be a plane wave. To this end, a very simple one dimensional system is considered. Since no potential term is imposed to the structure, the Hamiltonian will only be made of the kinetic term. Therefore, 2.5 takes the following form:

$$-\frac{\hbar^2}{2m^*} \frac{d^2}{dx^2} \psi(x) = E\psi(x) \quad (2.7)$$

which can be rewritten introducing the wave number:

$$k = \sqrt{\frac{2m^*}{\hbar^2} E} \quad (2.8)$$

so that:

$$\frac{d^2}{dx^2} \psi(x) + k^2 \psi = 0 \quad (2.9)$$

Notice that, in 2.7, the mass of the electron is reported as being  $m^*$ , called effective mass. While it is true that in the studied case (free particle), the effective mass of the electron is simply its mass, in a generic analysis the electron does not behave as its mass was its free space mass. Therefore from now on it is always assumed to be an effective mass. Equation 2.9 is easily solved by considering the characteristic polynomial, leading to:

$$\psi(x) = Ae^{ik_x x} + Be^{-ik_x x}$$

which means that, for a free particle in 1D, the wave function associated to it is a superposition of a forward and backward propagating waves. In this simple analysis,

the backward propagating term is neglected (if we consider it as an incoming wave there is nothing causing it to be reflected in the opposite direction), thus making the wave function a plane wave if time dependency was introduced. In fact, if the problem is extended in a 3D problem, assuming separation of variables and including time dependency:

$$\psi(x, y, z; t) = C e^{i(k\vec{r} - \omega t)} \quad (2.10)$$

Of course, even in this extremely simple example, the obtained result is not at all accurate. In fact, there is no way of normalizing it, that is to say that it is not possible to ensure that the integral of the wave function squared over the whole space goes to 1. The reason for which that is the case is quite obvious: it has been assumed that we have an infinitely extended space without any potential term when this is not representative of what happens in real applications. Nevertheless, this is not a too rough approximation, since for small nanoscaled system the laboratory is approximately infinite and so no problems are really present.

### 2.1.2 Confinement and bounding box approximation

Until now all the analysis have been carried out in the hypothesis of free particles. This is not what happens in a molecule, that is an example of 0D system. This means that a particle in a molecule is subjected to the presence of a potential energy barrier which limits the motion in all three directions.

It is important to notice that this first analysis will be performed with a very rough approximation, that is the presence of a potential well in all three dimensions. Indeed, in a real molecule the structure is much more complex and the potential can not be simply reduced to a potential well. In fact, particles interact together through potential forces, thus making the Hamiltonian extremely hard to manage. The bounding box approximation is nevertheless used to get in an analytical and straightforward way eigenfunctions and eigenvalues for a system.

The potential profile (assumed to be equal in the three directions) can be described as:

$$\begin{cases} U_x(x) = 0, & \text{if } 0 \leq x \leq L \\ U_x(x) = U_0, & \text{otherwise} \end{cases}$$

Lets focus on the cases in which the energy of the particle is smaller than the height of the well, that is to say  $0 < E < U_0$ . While it may be important to see what happens when the energy is higher, to understand the unique properties arising from a quantum mechanical analysis, for the purpose of this work it is not of interest. In the considered conditions, Schrödinger equation assumes two different forms depending on whether the potential is present or not. Conventionally, the

region to the left of the well is indicated as region I, the well as region II and the right side as region III. Therefore:

$$\begin{cases} \frac{d^2}{dx^2}\psi(x) - \frac{2m^*}{\hbar^2}(U_0 - E)\psi(x) = 0, & \text{region I, III} \\ \frac{d^2}{dx^2}\psi(x) + \frac{2m^*}{\hbar^2}E\psi(x) = 0, & \text{region II} \end{cases}$$

Introducing:

$$\lambda = \sqrt{\frac{2m^*}{\hbar^2}(U_0 - E)} = \pm\alpha$$

and considering that in region II the solution is the one of a free particle:

$$\begin{cases} \psi_I(x) = Ae^{+\alpha x} + Be^{-\alpha x}, & \text{region I} \\ \psi_{II} = Ce^{ikx} + De^{-ikx}, & \text{region II} \\ \psi_{III}(x) = Ee^{+\alpha x} + Fe^{-\alpha x}, & \text{region III} \end{cases}$$

The various unknown coefficients can be found by supposing  $B$  and  $E$  equal to 0, to avoid unlimited wave function, and by enforcing continuity at the boundaries of the well both for the wave function and for its derivative:

$$\begin{cases} \psi_I(0) = \psi_{II}(0) & \psi'_I(0) = \psi'_{II}(0) \\ \psi_{II}(L) = \psi_{III}(L) & \psi'_{II}(L) = \psi'_{III}(L) \end{cases}$$

While it is possible to find the solution by solving the resulting system, an easier way to proceed consists in considering that the wave function can either be even or odd but not a combination of the two. As a result, boundary conditions will only have to be enforced on one boundary, since the coefficients  $A$  and  $F$  will be equal in the even case or opposite in the odd case, thus requiring continuity for  $\psi$  on just one side of the well. Notice that typically the analysis is further simplified by considering infinitely high potential barriers. In this case,  $\alpha$  goes to  $\infty$  ( $U_0 = \infty$ ) and so  $\psi_I$  goes to 0 (negative exponent due to negative x values) as well as  $\psi_{III}$  (negative exponent due to negative sign). Imposing boundary conditions at  $x = 0$ , one gets  $C = -D$  and therefore:

$$\psi(x) = C(e^{ikx} - e^{-ikx}) = 2iC\sin(kx) = A\sin\left(\frac{n\pi}{L}x\right)$$

with:

$$A = \sqrt{\frac{2}{L}}$$

imposed through normalization. Considering also that  $2iC\sin(kx)$  must be 0 at  $x = L$  (for continuity between  $\psi_{II}$  and  $\psi_{III}$ ):

$$k = \frac{n\pi}{L}$$

$$E = \frac{\hbar^2 k^2}{2m^*} = \frac{n^2 \hbar^2 \pi^2}{2m^* L^2}$$

where  $n$  is an integer different from 0.

There are some very important results coming as consequence of the analysis carried out thus far. First of all, quantization of energetic levels is directly embedded within Schrödinger equation when suitable boundary conditions are applied. Then, in the case of confinement at nanoscale, electrons can not be described anymore as plane waves. Instead, they are described by means of sinusoidal even or odd functions. Notice that the analysis is easily extended to the 3D case by exploiting factorization obtaining the product of sinusoidal functions along the three directions:

$$\psi(x, y, z) = A \sin\left(\frac{n_x \pi}{L_x}\right) \sin\left(\frac{n_y \pi}{L_y}\right) \sin\left(\frac{n_z \pi}{L_z}\right)$$

to which the associated energetic levels, supposing  $L_x = L_y = L_z = L$ , are:

$$E = \frac{\pi^2 \hbar^2}{2m^* L^2} (n_x^2 + n_y^2 + n_z^2)$$

This way of analyzing a quantum system is usually referred to as the "bounding box" approximation. A molecule, in a very harsh viewpoint, can be seen as a system in which confinement occurs in all directions, with an approximated potential well profile. Indeed, this approximation is not good at all, especially for 0D systems like the one of a molecule. Nevertheless, it is usually a good way for understanding the concepts of confinement and quantization of energetic levels, which is of course also predicted by more complex methods and observed experimentally.

## 2.2 Density of states in quantum confined systems

Before addressing how transport works in quantum dots and hence in molecules, it is crucial to first understand how confinement affects the density of states (DOS) of electrons within the device. Indeed, the transport properties of a system are directly related to the density of states and it is therefore a required step to study it in molecule-based systems.

Of course, since the DOS represents the number of electron states per unit volume per unit energy and since the previous analysis proved that in nanoscaled devices the energy is quantized, a modification of the DOS is also expected. It is well known that the density of states for a 3D device is continuous:

$$\rho^{3D}(E) = \frac{1}{2\pi^2} \left(\frac{2m^*}{\hbar^2}\right)^{3/2} \sqrt{E - E_C} \quad (2.11)$$

As shown in the following, this is not anymore the case for lower dimensional structures, in which a different behavior is obtained as a function of the dimensionality of the system.

### 2.2.1 Density of states in 2D structures

Lets suppose confinement occurs along the  $z$  direction. In this case a 2D system, usually referred to as a quantum well, is obtained. It can be shown that the energy levels are distributed in a parabolic way:

$$E = \frac{\hbar^2(k_x^2 + k_y^2)}{2m^*} + c_j E_0$$

where the first term is related to the  $x$  and  $y$  directions (notice the parabolic dependence) while the second to the  $z$  direction, which causes the discretization between the various parabolas. It is possible to understand this point by considering a 3D plot in which horizontally there is the  $k_x, k_y$  plane whereas vertically there are the energies. Moving along the vertical direction the energies defined by the second term are found. Whenever one of them is encountered, a new parabola begins, defined by the first term. So, in the 3D representation just mentioned there are various parabolas, also called sub-bands, spaced apart due to the discretization imposed by the confinement in the  $z$  direction.

To retrieve the density of states in this condition, a  $k_x, k_y$  plane is considered, represented in figure 2.1. For now, only one sub-band is taken into account.

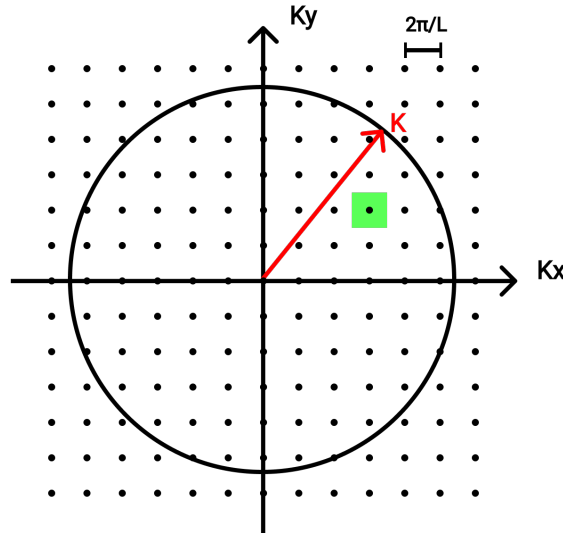


**Figure 2.1:** Graphical representation of the  $k_x, k_y$  plane. The green box is the area occupied by a single state.

For a generic value of  $k$  a circle of area:

$$A_{circle} = \pi k^2$$

is obtained. Supposing  $L_x = L_y = L$ , a single state will occupy a squared area equal to:

$$A_{state} = \left(\frac{2\pi}{L}\right)\left(\frac{2\pi}{L}\right) = \frac{4\pi^2}{L^2}$$

The number of available states as a function of  $k$  can therefore be written, considering a factor of two to include degeneracy, as:

$$N(k) = 2 \frac{A_{circle}}{A_{state}} = 2 \frac{\pi k^2 L^2}{4\pi^2} = \frac{k^2 L^2}{2\pi}$$

which can be expressed as a function of energy (using 2.8):

$$N(E) = \frac{m^* L^2}{\pi \hbar^2} E$$

Reminding that the density of states can be expressed as:

$$\rho^{2D} = \frac{1}{V} \frac{dN(E)}{dE} = \frac{1}{L^2} \frac{dN(E)}{dE}$$

one gets:

$$\rho^{2D} = \frac{1}{L^2} \frac{m^* L^2}{\pi \hbar^2} = \frac{m^*}{\pi \hbar^2} \quad (2.12)$$

Equation 2.12 tells that the density of states in the case in which confinement occurs in one direction is energy independent.

If more sub-bands are involved in the  $z$  direction, 2.12, considering a constant contribution by each of them, becomes:

$$\rho_{TOT}^{2D}(E) = \sum_{\mu_z=1}^{N_{bands}} \frac{m^*}{\pi \hbar^2} H(E - E_{\mu_z})$$

where  $H(x)$ , with  $x = (E - E_{\mu_z})$  is the Heaviside function of value 0 when  $x$  is smaller or equal than 0 and 1 otherwise.

## 2.2.2 Density of states in 1D structures

A similar analysis can be carried out also in the case of confinement in two directions. In this case confinement is supposed to happen in the  $x$  and  $y$  direction. The resulting structure is a 1D system, also called quantum wire.

Differently from before the total energy is expressed by the sum of a parabolic contribution given by the free  $z$  direction and a discrete contribution imposed by the  $x$  and  $y$  confinement. Therefore the representation of the energy levels can be seen in a 2D plane where the abscissa is related to  $k_z$  whereas the ordinate is linked to the energy. Moving vertically there are now the energies (discrete) defined by the  $x$  and  $y$  directions while horizontally there are parabolas caused by the free movement in  $z$ .

Fixing  $k_x, k_y$ , a  $k_z$  plane is obtained (see figure 2.2). Supposing a certain  $k$  vector, the density of states is easily derived with the same approach as before:

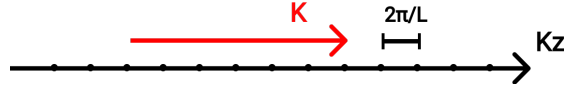


**Figure 2.2:** Graphical representation of the  $k_z$  plane.

$$N(k) = 2 \frac{k}{\frac{2\pi}{L}} = 2 \frac{kL}{2\pi} = \frac{kL}{\pi}$$

$$N(E) = \frac{L}{\pi} \sqrt{\frac{2m^*}{\hbar^2} E_z}$$

from which:

$$\rho^{1D} = \frac{1}{L} \frac{dN(E)}{dE} = \frac{\sqrt{m^*}}{\pi \hbar} \frac{1}{\sqrt{2(E - E_{\mu_x, \mu_y})}}$$

Notice that, differently from the previous case, the density of states is energy dependent. Therefore, in this case a parabolic shaped function is retrieved instead of a staircase structure. The analysis can be completed by considering all the possible levels involved, leading to:

$$\rho_{TOT}^{1D}(E) = \frac{1}{L} \frac{dN(E)}{dE} = \frac{\sqrt{m^*}}{\pi \hbar} \sum_{\mu_x=1, \mu_y=1}^{N_{bands}} \frac{H(E - E_{\mu_x, \mu_y})}{\sqrt{2(E - E_{\mu_x, \mu_y})}}$$

### 2.2.3 Density of states in 0D structures

It is finally time to tackle the density of states of 0D systems, usually referred to as quantum dots. In this case the density of states is immediately retrieved as a series of Dirac deltas centered in the energy eigenvalues:

$$\rho_{TOT}^{0D}(E) = \sum_{\mu_x=1, \mu_y=1, \mu_z=1}^{N_{bands}} 2\delta(E - E_{\mu_x, \mu_y, \mu_z}) \quad (2.13)$$

The densities of states for the various cases analyzed are reported in figure 2.3. Notice that the one reported is just a graphical qualitative representation and hence the energy values and heights of the DOS are not chosen in a quantitative/meaningful way, but to give an idea of the difference between the various structures. Indeed, the true values depend on the structure under analysis and hence the graph reported is inserted to generalize the analysis.

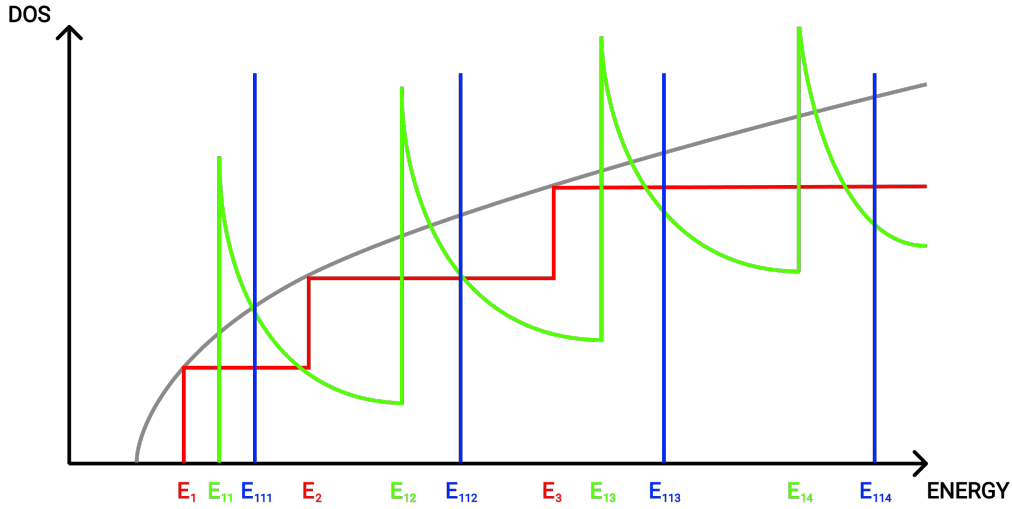


**Figure 2.3:** Comparison of the density of states in 3D (grey line), 2D (red line, notice the energy independent behavior), 1D (green line) and 0D (blue lines).

## 2.3 Transport model

In this section a very simplified model for the analysis of transport in 0D systems is introduced. The procedure is the one done in the "Nanoelectronic Systems" course held by professors Mariagrazia Graziano and Gianluca Piccinini in 2020.

Lets suppose to have a quantum dot with just one energetic level  $E_L$  connected to a source and a drain with Fermi level  $E_F$  shared between the two contacts. Of course, in this initial configuration, the number  $N$  of electrons occupying the quantum dot can only be equal to 0, if  $E_L > E_F$ , or 2 ,if  $E_L < E_F$ . The resulting system is reported in figure 2.4. In both of these cases the system will not provide a current. Theoretically, the only way to observe conduction through the dot is when  $E_L$  is placed between the Fermi level of the source and the one of the drain. This situation is only possible in the case in which a voltage is applied, thus shifting the position of the Fermi level in the source and the drain. In fact, the main effect of applying a voltage across the structure is to shift the position of the Fermi levels as to have a difference between them equal to  $-qV_{DS}$ .

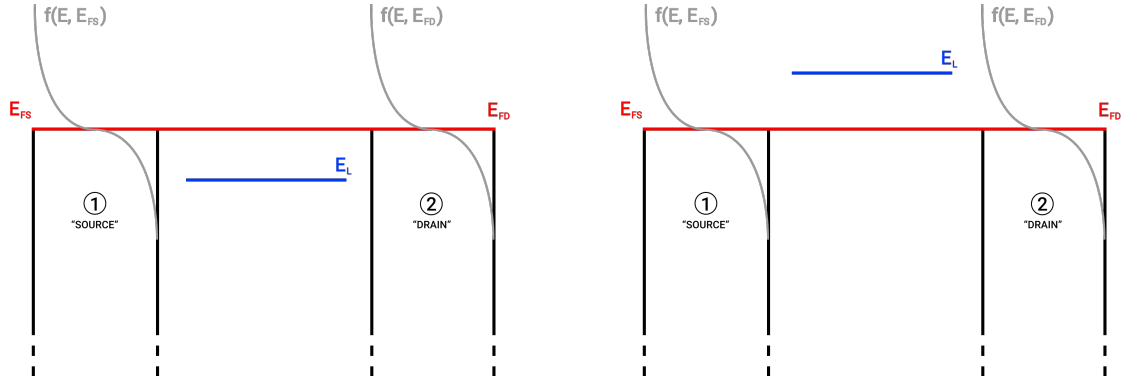


**Figure 2.4:** Considered system in the case in which the energy of the level is lower (left) or higher (right) with respect to the Fermi level of source and drain.

To study how the system behaves it is first necessary to introduce the concept of coupling. When the quantum dot is connected to the contacts, the creation of a bonding occurs. This bonding can be strong or weak, thus resulting in strong or weak coupling. The concept of coupling can also be associated to the one of delocalization of the electronic wave function. In the case of weak coupling the wave function is said to be localized either in the contact or in the dot and so it is not easy for the particle to go from one side of the structure to the other. If, instead, strong coupling occurs, the wave function is delocalized, therefore causing the electronic cloud to be somewhat shared between the dot and the contacts. As a result, it is easy for electrons to flow through the device and contribute to the formation of a current. The quality of coupling is related to the type of bonding created, which can be of chemical type, i.e. a covalent bond, or electrical, i.e. Coulomb interaction and hence physisorption (see chapter 5 for more about interactions).

Practically speaking, coupling is expressed in the following analysis by means of two coefficients,  $\gamma_1$  and  $\gamma_2$  (where the subscript "1" indicates the source whereas "2" the drain), which are a measure of how strong the coupling of the dot is with respect to the source and the drain. Although in theory the two coefficients differ one with respect to the other due to technological variability or to process design, they are usually assumed to have the same value. To these two coefficients two quantities, called intrinsic lifetimes, are associated. They are a measure of the average time required for an electron to go from one portion of the device to another. The smaller it is the better the coupling. In fact:

$$\gamma_1 = \frac{\hbar}{\tau_1} \quad \gamma_2 = \frac{\hbar}{\tau_2}$$

It is now possible to go deeper into the analysis. To do so, two fluxes of electrons are considered in the case in which a voltage is applied. The structure is reported in figure 2.5.

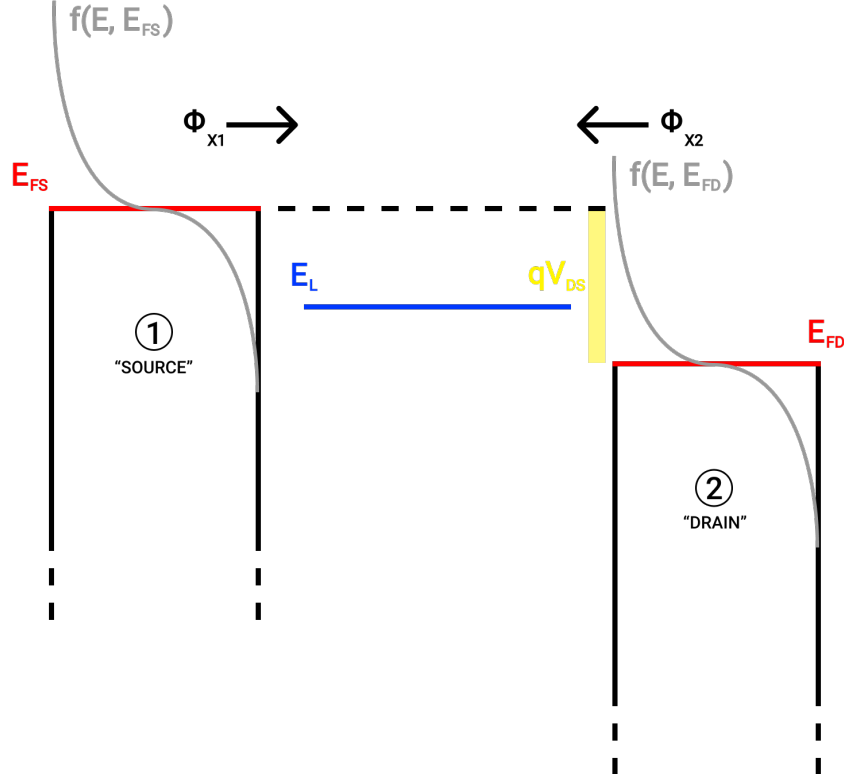


**Figure 2.5:** Structure under analysis with an applied voltage  $V_{DS}$ , creating a bias window (yellow strip).

Notice how, as anticipated earlier, the applied voltage causes a shift in the position of the Fermi level in the two contacts, creating what is usually referred to as the bias window.

The two fluxes can be expressed as:

$$\Phi_{x1} = \Phi_{x,1 \rightarrow dot} - \Phi_{x,dot \rightarrow 1} \quad (2.14)$$

$$\Phi_{x2} = \Phi_{x,2 \rightarrow dot} - \Phi_{x,dot \rightarrow 2} \quad (2.15)$$

Reminding that a flux of particles is given by the number of particles flowing through a considered area in the unit time, the single components in 2.14 and 2.15 can be expressed in a simple way. The unit time can be simply defined by employing the intrinsic lifetimes. As far as the fluxes from source to the dot and

from the drain to the dot are concerned, the numbers of particles flowing are given by the Fermi function evaluated at the energy level  $E_L$  with  $E_{FS}$  and  $E_{FD}$  as references respectively for the source and drain fluxes, multiplied by two in order to include spin degeneracy. The outward number of particles from the dot to the contacts are instead obtained using the number of electrons  $N$  already introduced earlier. Therefore:

$$\begin{aligned}\Phi_{x,1\rightarrow dot} &= \frac{2f(E_L, E_{FS})}{\tau_1} = \frac{2\gamma_1 f(E_L, E_{FS})}{\hbar} \\ \Phi_{x,dot\rightarrow 1} &= \frac{N}{\tau_1} = \frac{\gamma_1 N}{\hbar}\end{aligned}\tag{2.16}$$

and:

$$\begin{aligned}\Phi_{x,2\rightarrow dot} &= \frac{2f(E_L, E_{FD})}{\tau_2} = \frac{2\gamma_2 f(E_L, E_{FD})}{\hbar} \\ \Phi_{x,dot\rightarrow 2} &= \frac{N}{\tau_2} = \frac{\gamma_2 N}{\hbar}\end{aligned}$$

Considering that the two fluxes 2.14, 2.15, due to mass conservation, are equal and opposite, it is possible to retrieve the number of electrons within the dot as:

$$N = \frac{2}{\gamma_1 + \gamma_2} [\gamma_1 f(E_L, E_{FS}) + \gamma_2 f(E_L, E_{FD})]\tag{2.17}$$

As previously anticipated, if the energy level of the dot is lower than the Fermi level of the source and drain, the two Fermi functions in 2.17 are equal to 1 and so  $N = 2$ . If instead it is higher, the Fermi functions are equal to 0 and so  $N = 0$ . The case of interest is instead the one reported in figure 2.5. When the voltage is high enough, if the energy level of the dot falls between the Fermi level of the drain and the one of the source,  $N = 1$  (one Fermi function is equal to 0 whereas the other one is equal to 1).

Making use of 2.14 and 2.17, it is possible to evaluate the current flowing through the device:

$$I_{DS} = q\Phi_{x1} = q \left[ \frac{\gamma_1}{\hbar} 2f(E_L, E_{FS}) - \frac{\gamma_1}{\hbar} N \right]\tag{2.18}$$

leading to:

$$I_{DS} = \frac{2q}{\hbar} \frac{2\pi\gamma_1\gamma_2}{\gamma_1 + \gamma_2} [f(E_L, E_{FS}) - f(E_L, E_{FD})]\tag{2.19}$$

From equation 2.19 it is easy to see that the current is null if the two Fermi functions with  $E_L$  as the considered energy have the same value. Furthermore, within this very simple analysis, the current is characterized by a step behavior as the level of the dot enters in the bias window.

A more general expression of 2.19 can be obtained considering more levels in the quantum dot (with each of them called  $E_{L,i}$ ) and including the expression for the density of states. In this first approximated model, the DOS for the quantum dot is assumed to have the expression of 2.13. Therefore:

$$I_{DS,i} = \frac{2q}{h} \frac{2\pi\gamma_{i,1}\gamma_{i,2}}{\gamma_{i,1} + \gamma_{i,2}} \int_{-\infty}^{\infty} \delta(E - E_{L,i}) [f(E_L, E_{FS}) - f(E_L, E_{FD})] dE \quad (2.20)$$

Introducing the concept of transmission spectrum:

$$T_i(E) = \frac{2\pi\gamma_{i,1}\gamma_{i,2}}{\gamma_{i,1} + \gamma_{i,2}} \delta(E - E_{L,i}) \quad (2.21)$$

$$T(E) = \sum_{i=1}^{N_{levels}} \frac{2\pi\gamma_{i,1}\gamma_{i,2}}{\gamma_{i,1} + \gamma_{i,2}} \delta(E - E_{L,i}) \quad (2.22)$$

equation 2.20, considering all the levels, becomes:

$$I_{DS} = \frac{2q}{h} \int_{-\infty}^{\infty} T(E) [f(E_L, E_{FS}) - f(E_L, E_{FD})] dE \quad (2.23)$$

### 2.3.1 Broadening of levels

The obtained  $I_{DS}$  is still lacking of some crucial elements. First of all, in the presence of a bonding between the system and the contacts, the energetic levels are broadened, due to delocalization of the electronic cloud. As a consequence, it is not true at all that the density of states can be simply reduced to a series of Dirac deltas. Instead, the shape covers a more extended spectrum of energies, therefore modifying to a great extent the shape of the  $I_{DS}$  curve, not characterized anymore by a step-like behavior but with a more smooth transition from off to on state. A typical way of modifying 2.13 is by making use of a lorentzian distribution:

$$D_{EL_i}(E) = \frac{\gamma_i/(2\pi)}{(E - E_{L,i})^2 + (\gamma_i/2)^2} \quad (2.24)$$

with:

$$\gamma_i = \gamma_{i,1} + \gamma_{i,2}$$

### 2.3.2 Capacitative model of quantum dot

Another thing missing in the analysis is the effect of the applied voltage to the levels within the dot. It is possible to associate to the connection between the dot and the source a certain capacitance  $C_s$ . The same occurs for the drain, with  $C_d$ . Of course, in this analysis a linearized model is considered, and therefore  $C_s$  and

$C_d$  are assumed to be independent on the applied voltage. In this viewpoint, the applied  $V_{DS}$  will fall onto the dot with the intensity:

$$V_{dot} = V_{DS} \frac{C_d}{C_d + C_s} = V_{DS} \frac{C_d}{C_{es}}$$

To it, a certain energy variation can be associated:

$$U_{VDS} = -qV_{dot} = -qV_{DS} \frac{C_d}{C_{es}} \quad (2.25)$$

This induces a shift in the transmission spectrum:

$$T(E) \rightarrow T(E - U_{VDS})$$

In the symmetrical case, equation 2.25 becomes:

$$U_{VDS} = -q \frac{V_{DS}}{2}$$

So, without considering broadening yet:

$$T(E_i - U_{VDS}) = \frac{2\pi\gamma_{i,1}\gamma_{i,2}}{\gamma_{i,1} + \gamma_{i,2}} \delta\left(E - E_{L,i} + q \frac{V_{DS}}{2}\right)$$

### 2.3.3 Charging effect

One thing which is still missing is the charging effect, that is to say the variation of the energetic level of the dot subsequent to the variation of the charge in it. Supposing that, at equilibrium,  $N = N_0$ , the variation of the charge due to the variation of the number of electrons is:

$$\Delta Q = -q(N - N_0)$$

A voltage drop can be associated to this charge:

$$\Delta V_{charging} = \frac{\Delta Q}{C_{es}} = -\frac{q(N - N_0)}{C_{es}}$$

and therefore a potential energy:

$$U_{charging} = -q\Delta V_{charging} = \frac{q^2}{C_{es}}(N - N_0)$$

As a consequence, 2.21 becomes:

$$T(E_i - U_{charging}) = \frac{2\pi\gamma_{i,1}\gamma_{i,2}}{\gamma_{i,1} + \gamma_{i,2}} \delta\left(E - E_{L,i} - \frac{q^2}{C_{es}}(N - N_0)\right)$$

Practically speaking, the direct consequence of the charging effect is the shift of the Fermi level of the dot.

### 2.3.4 Self-consistent loop

The analysis of the previous parts comes with an important consequence. In fact, 2.17, in the general case, takes the form:

$$N(V_{DS}) = \sum_{i=1}^{N_{levels}} \int_{-\infty}^{\infty} \frac{2}{\gamma_{i,1} + \gamma_{i,2}} D_{EL_i}(E - U) [\gamma_{i,1} f(E, E_{FS}) + \gamma_{i,2} f(E, E_{FD})] dE \quad (2.26)$$

where:

$$U = U_{VDS} + U_{charging} = -q \frac{C_d}{C_{es}} V_{DS} + \frac{q^2}{C_{es}} (N - N_0) \quad (2.27)$$

Therefore, a self-consistent analysis is required. The applied voltage causes a shift of the energy levels of the dot but, as soon as a new level enters in conduction, a variation of the energy due to charging effect occurs, thus moving the energy level in the opposite direction. A complete analysis of a quantum dot, in a real case scenario, is thus a very complex task, already with the very simplified model introduced so far.

### 2.3.5 Gate effect

While the analysis seems to be complete, a final effect can to be taken into account. Of course, in a real application, the presence of a gate may be necessary (in the realization of a sensor it can be another option for the design of the system). The effect of an applied gate voltage onto the dot is nevertheless not too complex to be managed. As in the case of charging effect and in the case of the shift introduced by the applied voltage  $V_{DS}$ , the gate is included by another shift in the energy of the dot, with a value:

$$U_{VGS} = -qV_{GS} \frac{C_g}{C_d + C_g + C_s} = -qV_{GS} \frac{C_g}{C_{es}} \quad (2.28)$$

## 2.4 Complete simplified model

To complete the chapter, the simplified model including all the just mentioned effects is here reviewed. The structure of reference is reported in figure 2.6. As seen in the previous parts, this structure includes the effect of the  $V_{DS}$  and  $V_{GS}$  voltages on the system due to the capacitance.

From the capacitive model:

$$V_{dot} = V_{GS} \frac{C_g}{C_s + C_d + C_g} + V_{DS} \frac{C_d}{C_s + C_d + C_g} = V_{GS} \frac{C_g}{C_{es}} + V_{DS} \frac{C_d}{C_{es}} \quad (2.29)$$

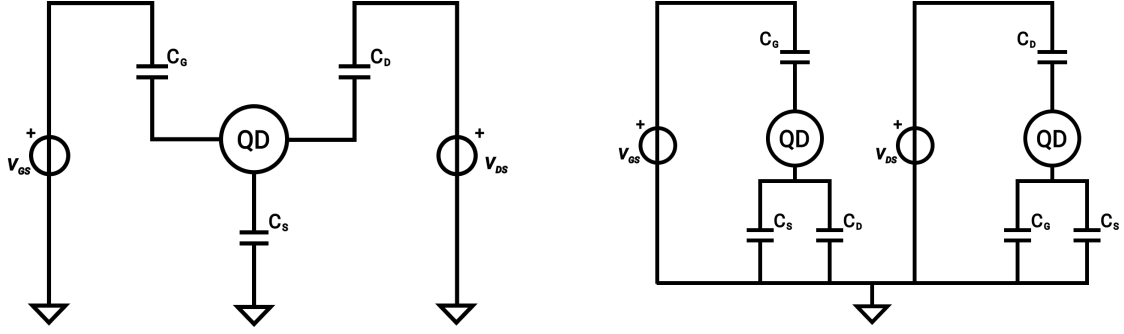


**Figure 2.6:** Complete structure for the simplified model in a figurative point of view (left) and in the corresponding circuitual representation (right).

and considering also the charging effect, the energy shift is equal to:

$$U_{SCF} = -qV_{DS}\frac{C_d}{C_{es}} - qV_{GS}\frac{C_g}{C_{es}} + \frac{q^2}{C_{es}}(N - N_0) \quad (2.30)$$

This equation has to be solved self-consistently with 2.26. Using the resulting values in:

$$I_{DS} = \frac{2q}{h} \int_{-\infty}^{\infty} T(E - U_{SCF}) [f(E_L, E_{FS}) - f(E_L, E_{FD})] dE \quad (2.31)$$

it is finally possible to evaluate the  $I_{DS}$  characteristic.

## Chapter 3

# Complete description of molecular systems

What has been analyzed thus far is usually referred to as the toy model. While it is able to give a rough idea of how conduction works in a molecular system, it is however far from being accurate. Furthermore, most of the elements introduced in it have not been justified at all from the theoretical standpoint.

The purpose of this chapter is therefore to analyze the system with a more complete model, but still in the mindset of not going too much into unnecessary details. The idea is, in fact, to give the fundamentals by means of which the settings for the simulations performed in the successive chapters may be understood. Furthermore, what is here presented will not be the full picture for the study of transport in molecular electronics. What is introduced is just the modeling of the Hamiltonian of the system and hence the study of energetic levels and wave functions. The model for the analysis of the  $I(V)$  characteristic demands a more in depth theoretical study, and will be performed in the next chapter. It has been chosen to separate that part from the one presented in this chapter in order to give a more meaningful and less complex idea of how the models at the core of successive simulations work.

The following approach is almost entirely extracted from the course "Solid State Physics" held by professor Giancarlo Cicero in Politecnico di Torino in 2019. More precisely, in section 3.1, the Hartree and Hartree-Fock (HF) models based on a wave function approach are analyzed. These are at the core of semi-empirical methods, briefly discussed in section 3.2, that will be widely exploited in the rest of the work and of which characteristics it is important to focus on. Then, in section 3.3, the discussion is shifted from wave functions based models to the density functional theory (DFT), in which wave functions are not the main focus anymore in exchange of the charge density.

Notice that the various simplifications introduced in the following are not the only ones implemented in simulations tools. Indeed, here the analysis is theoretical, which means that it is not reported yet the way in which the resulting equations are practically solved. In that it may seem that it is not concrete. Nevertheless, having in mind the general theoretical procedure allows one to understand what is the theory at the base of the calculators, to really capture the meaningful differences in the various models. Of course, in practical applications, due to the limited computational power available, other simplifications have to be employed, but keeping these separated from the ones of this chapter have been decided to be the correct choice, in order to avoid possible confusions.

### 3.1 Wave function based models

As evinced in chapter 2, the starting point for the analysis of systems with dimensions in the order of few nanometers or below is the use of Schrödinger equation. Already in this step, the previous analysis is extremely approximated. Indeed, the bounding box approximation is not accurate at all in depicting the potential term of the Hamiltonian, which is way more complex than a simple square-well, and also the kinetic term has been oversimplified.

In a general viewpoint, a nanoscopic system can be studied as a many-body problem of interacting particles, to which the associated Hamiltonian can be expressed as:

$$\hat{H} = \hat{T} + \hat{V}$$

with the kinetic component equal to:

$$\hat{T} = -\frac{\hbar^2}{2m_e} \sum_{i=1}^{N_{electrons}} \Delta_i - \hbar^2 \sum_{A=1}^{N_{atoms}} \frac{1}{2M_A} \Delta_A$$

where the first term is related to the kinetic energy of electrons whereas the second one to ions. Notice that, in order to take into account the possibility of having different masses of ions, the mass has been inserted in the summation. The  $\Delta$  represents the laplacian with respect to all the three directions and to simplify the notation only the subscripts  $i$  and  $A$  related to either electrons or ions have been placed.

The potential term can instead be expressed as:

$$\hat{V} = \frac{1}{2} \sum_i^{N_{el.}} \sum_{j \neq i}^{N_{el.}} \frac{e^2}{4\pi\epsilon_0 |\vec{r}_i - \vec{r}_j|} + \frac{1}{2} \sum_A^{N_{at.}} \sum_{B \neq A}^{N_{at.}} \frac{e^2 Z_A Z_B}{4\pi\epsilon_0 |\vec{R}_A - \vec{R}_B|} - \sum_i^{N_{el.}} \sum_A^{N_{at.}} \frac{e^2 Z_A}{4\pi\epsilon_0 |\vec{r}_i - \vec{R}_A|}$$

where the first term is connected to the interaction between electrons, the second between ions and the third to the interaction between electrons and ions, hence the

presence of the minus sign representing the attraction. The  $1/2$  term is inserted to avoid double counts and is thus not necessary in the third term.

### 3.1.1 Born-Oppenheimer approximation

It is rather obvious that the resulting Schrödinger equation can not be solved even for small systems of atoms, let alone a complex molecular electronic system of hundreds if not thousands of particles as the one analyzed in the following. In order to proceed further, all the models described in this chapter are based on the Born-Oppenheimer approximation, also called adiabatic approximation. The idea is that the kinetic energy term related to ions can be neglected as their mass is huge if compared to the one of electrons. As a consequence, ions are assumed to be still and as such the potential energy term associated to the interaction between ions becomes constant (the relative positions of ions do not change). Indeed, since in this approximation ions are not able to move, the information about electron-phonon interaction is lost, but this is not important as this interaction is not here of interest.

The Hamiltonian can be then rewritten as:

$$\hat{H}_{el.} = -\frac{\hbar^2}{2m_e} \sum_{i=1}^{N_{el.}} \Delta_i + \frac{1}{2} \sum_{i=1}^{N_{el.}} \sum_{j=1, j \neq i}^{N_{el.}} \frac{e^2}{4\pi\epsilon_0 |\vec{r}_i - \vec{r}_j|} - \sum_{i=1}^{N_{el.}} \sum_{A=1}^{N_{at.}} \frac{e^2 Z_A}{4\pi\epsilon_0 |\vec{r}_i - \vec{R}_A|} + const. \quad (3.1)$$

Typically, the interaction term between electrons is referred to as  $\hat{V}_{int.}$ , whereas the interaction between electrons and ions is  $\hat{V}_{ext.}$ . Of course, the presence of the constant term is not relevant since ions are fixed. Notice that, if one were to solve the corresponding Schrödinger equation, the resulting eigenstate would be a wave function associated to the whole many-body system which, in the case of a molecule, is simply a molecular orbital.

### 3.1.2 Mean Field Approach

Even though the adiabatic approximation helps in reducing the complexity of analysis, it is however insufficient to make Schrödinger equation solvable. In fact, the  $\hat{V}_{int.}$  term makes the analysis unmanageable. Therefore, in conjunction with the previous approximation, the mean field approach is usually employed. What will be obtained within this method is that the many-body problem gets reduced to a one-body problem, thus simplifying to a great extent the calculations. The main assumption is that the internal potential energy term can be substituted with an effective term resulting from all the electrons but one (of course an electron can not interact with itself). As a consequence, by choosing one electron at a time, the potential to which it is subjected is generated by all the other particles. With this

idea in mind, equation 3.1 becomes:

$$\hat{h}(\vec{r}_i) = -\frac{\hbar^2}{2m_e}\Delta_i - \sum_{A=1}^{N_{at.}} \frac{e^2 Z_A}{4\pi\epsilon_0 |\vec{r}_i - \vec{R}_A|} + V_{eff.}(\vec{r}_i)$$

where  $\hat{h}(\vec{r}_i)$  is a single electron Hamiltonian. Schrödinger equation then becomes:

$$\hat{h}(\vec{r}_i)\psi_k(\vec{r}_i) = E_k\psi_k(\vec{r}_i) \quad (3.2)$$

where it has been hypothesized that the wave function of the whole system can be expressed as the product of single particle wave functions:

$$\psi(\vec{r}_1, \vec{r}_2, \dots, \vec{r}_N) = \psi_k(\vec{r}_1)\psi_j(\vec{r}_2)\dots\psi_l(\vec{r}_N) \quad (3.3)$$

### 3.1.3 Hartree model

While the elements introduced thus far contain most of the components included in the famous Hartree model, there is however one missing element which is necessary, that is the presence of the spin associated to electrons. For the approximation to be close to the real behavior of the system, the total Hamiltonian will in fact have to take into account the spin. This can be done by including a spin dependency in the wave functions associated to the system.

Introducing:

$$\vec{x} = (\vec{r}, \sigma)$$

where  $\sigma$  is the spin, equation 3.3 becomes:

$$\psi_k(\vec{r}_1)\alpha(\sigma_1)\psi_j(\vec{r}_2)\alpha(\sigma_2)\dots\psi_l(\vec{r}_N)\alpha(\sigma_N) = \chi_k(\vec{x}_1)\chi_j(\vec{x}_2)\dots\chi_l(\vec{x}_N) \quad (3.4)$$

This production is known as the Hartree product and is at the core of one of the first model historically developed, known as the Hartree model. Within it, it is supposed that the wave function of the initial many-body system can be expressed as the product of single particle spin-orbitals.

### 3.1.4 Slater determinant

The Hartree product has been widely exploited through the years, but it is however still incomplete. In fact, it does not respect the anti-symmetry principle and it is only able to take into account anti-correlated electrons, so that the probability of finding an electron in a certain position is independent with respect to the probability of finding another electron in the same position (if one were to write the wave function squared in order to evaluate the density of probability, the various term would not depend one on the other since no cross product is present). Indeed,

this is a quite rude approximation, since the motion of an electron depends on the position of the others. In order to partially solve these issues, a usual procedure involves employing a linear combination of Hartree products. The resulting system is known as the Slater determinant:

$$\psi(\vec{x}_1, \dots, \vec{x}_N) = \frac{1}{\sqrt{N!}} \begin{bmatrix} \chi_i(\vec{x}_1) & \chi_j(\vec{x}_1) & \dots & \chi_l(\vec{x}_1) \\ \chi_i(\vec{x}_2) & \chi_j(\vec{x}_2) & \dots & \chi_l(\vec{x}_2) \\ \dots & \dots & \dots & \dots \\ \chi_i(\vec{x}_N) & \chi_j(\vec{x}_N) & \dots & \chi_l(\vec{x}_N) \end{bmatrix} \quad (3.5)$$

The anti-symmetry requirement is respected as exchanging two rows causes a change of sign. On the other hand, if two electrons share the same place, two columns are equal and so the determinant goes to 0, respecting Pauli. The resulting model, usually referred to as being the Hartree-Fock method, is able to solve the problem of anti-symmetry and Pauli, but it still does not account for correlation.

### 3.1.5 Variational approach

Without caring, for now, about the correlation term still missing from the analysis, it is now possible to finally develop the methodology for the analysis of a system. Moving back to the full picture, the Hartree product or the Slater determinant can be used to build the wave function of the system. This can be done by means of a variational approach. What does this mean? First, an approximation for the wave function of the system is made:  $\psi'$ . This approximation, that depends on a parameter which can be varied, may be used for the evaluation of the expectation value for the energy. In particular:

$$E' = (\langle \psi' | \hat{H} | \psi' \rangle) > (\langle \psi_0 | \hat{H} | \psi_0 \rangle) = E_0$$

where the second term is related to the effective wave function of the system. Of course, since the initial guess for the system is not the exact one, it is expected that the evaluated energy by means of it is higher with respect to the true one of the system. The parameter ( $x$  in this case) of the initial guess is then modified in order to ensure:

$$\frac{\partial E'(x)}{\partial x} = 0$$

Considering for example an hydrogen atom, a good approximation is represented by a gaussian profile:

$$\psi'(\vec{r}) = N e^{-r^2 \alpha}$$

in which  $N$  is obtained from normalization and  $\alpha$  is unknown (it is the  $x$  parameter). By calculating the expected value for the Hamiltonian, an energy eigenvalue

$E'$  is obtained. The best unknown parameter for the system, with the chosen approximation, will be evaluated by means of:

$$\frac{\partial E'(\alpha)}{\partial \alpha} = 0$$

Therefore, the best approximation which can be possibly obtained using a gaussian profile depends on  $\vec{r}$  and  $\alpha$ :  $\psi'(\vec{r}, \alpha)$ . Of course, in a general case, neither the wave function nor the eigenvalue are known *a priori* (in the hydrogen example just done the "real" profile for the wave function is known and so it is easy to do a first guess). What is done to solve this issue is to choose a basis set that is able to produce the whole space, meaning it should be a complete basis set. With it it is possible to build the initial guess using linear expansion coefficients.

So, to summarize, in a general case scenario a basis set is chosen:

$$\{\phi_n(\vec{r})\}$$

which has to be a complete basis set, such that:

$$\psi'(\vec{r}) = \sum_n c_n \phi_n(\vec{r})$$

where  $c_n$  are the coefficients found by exploiting:

$$\frac{\partial E'}{\partial c_i} = 0$$

With this idea in mind, getting back to the initial problem, the variational approach can be used with the Hartree product (or Slater determinant), where the unknowns are the spin-orbitals. Therefore:

$$E' = \langle \psi^{HP} | \hat{H} | \psi^{HP} \rangle \quad (3.6)$$

$$\frac{\partial E'}{\partial \chi_i} = 0$$

To complete the analysis there is an additional requirement, which is to satisfy normalization, such that:

$$\langle \chi_i(\vec{x}_i) | \chi_i(\vec{x}_i) \rangle = 1$$

This is usually referred to as being a constraint, and is needed in order to proceed. Explicitly writing equation 3.6, one gets:

$$\begin{aligned} E' = \langle \psi^{HP} | \hat{H} | \psi^{HP} \rangle = & -\frac{1}{2} \sum_{i=1}^{N_{el.g}} \int d\vec{x}_i \chi_i^*(\vec{x}_i) \Delta_i \chi_i(\vec{x}_i) \\ & + \frac{1}{2} \sum_{i=1}^{N_{el.}} \sum_{j=1, \neq i}^{N_{el.}} \int \int d\vec{x}_i d\vec{x}_j \frac{|\chi_i(\vec{x}_i)|^2 |\chi_j(\vec{x}_j)|^2}{|\vec{r}_i - \vec{r}_j|} \\ & - \sum_{i=1}^{N_{el.}} \sum_{A=1}^{N_{at.}} \int d\vec{x}_i \frac{Z_A}{|\vec{r}_i - \vec{R}_A|} |\chi_i(\vec{x}_i)|^2 \end{aligned}$$

where atomic units have been employed to simplify the analysis. In conjunction with this equation, constraints have to be enforced. In particular, there are  $N$  constraints (one per particle), expressed as:

$$\sum_{i=1}^{N_{el.}} [\langle \chi_i(\vec{x}_i) | \chi_i(\vec{x}_i) \rangle - 1] = 0$$

Without going into the details of the calculations, at the end what is obtained are eigenvalue problems, also called Hartree equations:

$$\left(-\frac{1}{2}\Delta_i + \sum_{j \neq i} \int d(\vec{x}_j) \frac{|\chi_j(\vec{x}_j)|^2}{|\vec{r}_i - \vec{r}_j|} - \sum_A \frac{Z_A}{|\vec{r}_i - R_A|}\right) \chi_i(\vec{x}_i) = E_i \chi_i(\vec{x}_i)$$

So, in order to find  $\chi_i$  (which are the spin-orbitals), it is necessary to solve an eigenproblem based on single particle eigenfunction. Notice that the integral in the final equation is the total repulsion term for the  $i$ -th electron, but that does not mean that this approach takes into account correlation. In fact, this element is only taken into account with other methods.

What has been discussed in this last section is the complete Hartree method. As noted previously, it does not take into account anti-symmetry and Pauli, which can be instead introduced by using, instead of simple Hartree product, the Slater determinant. In that case the resulting method is called Hartree-Fock model.

Before proceeding it is important to review the full methodology within the depicted framework. First of all, since the complete Hamiltonian of a system is unmanageable even for small aggregates of atoms, the Born-Oppenheimer approximation is employed, removing the additional complexity of studying the energy terms related to ions. Then, the mean field approach comes in play, simplifying to a further extent the treatment assuming that the many-body problem can be decoupled into single-body problems, leading to the Hartree model, in the case in which simple products between the independent particles wave functions are considered, or to the Hartree-Fock method, if instead the Slater determinant is used to build the total wave function.

At this point it is fundamental to do some considerations. The analysis of the system in the Hartree-Fock model starts with a first guess, which is typically built starting from isolated atoms (if one has two hydrogen atoms, the initial wave function of the system is obtained as the product of gaussian functions centered on the two atoms which are independent one with respect to the other). This guess is associated to the wave function of independent particles and includes a parameter which can be varied. In particular, knowing that the goal is to minimize the energy of the system as to find the solution which mimics in the best way possible the true ground state of the system, the variational approach is exploited to find the most suitable parameter for the guess. This allows to evaluate the

set of spin-orbitals that minimize the energy associated to the Slater determinant. What is important to highlight is that the solution of the final set of equations, enforced by the necessary constraints, depends on the orbital themselves, meaning that the Hartree-Fock method is an iterative model, also called self-consistent field procedure. In particular, this is due to the effective potential term related to the interaction of the electron in a certain spin-orbital with the average field generated by all the other electrons.

Another thing to notice is that in the Hartree-Fock treatment an exchange term is present, which causes the energy values finally obtained to be smaller than the ones obtained from simple Hartree method and therefore closer to the desired solution. Again, it is important not to think that correlation is embedded through Hartree-Fock. This is not true and correlation will be something only other methods include, with the presence of an exchange-correlation term.

## 3.2 Semi Empirical methods

The previous analysis has shown that it is possible to study a system by means of Schrödinger equation exploiting the Born-Oppenheimer and the mean-field approximations, obtaining the Hartree and the Hartree-Fock methods. Furthermore, and this will be clearer in the following when density functional theory will be described, these models are wave functions based, which means that the self-consistency is achieved by working on wave functions and using a variational approach. In this section, starting from Hartree and Hartree-Fock, other models are briefly introduced in order to be finally able to describe the tools present in the *quantum ATK* environment (the software used for performing all the simulations), and that will be widely employed in the rest of the work. Notice that, since they are not used in successive sections, the so-called "post Hartree" methods are not addressed. These make the HF analysis more complete by considering in some ways the lacking correlation term.

Although it has been possible to greatly simplify the initial problem, it is still computationally intensive to proceed in the calculations with the just presented models. In order to go further, a class of models which start from Hartree-Fock, known as semi-empirical methods, have been developed through the years. Of this category belong two important models used in the following, namely the Extended-Hückel and the Slater-Koster theories. The main idea is to reduce the complexity of the analysis by exploiting corrections coming from experimental data (or ab-initio methods). Indeed, it is necessary to employ data that is quite accurate, otherwise the already simplified model will give very inaccurate results. Furthermore, since most of the parameters taken have been found for specific cases, it is a good practice to verify the goodness of a semi-empirical method by means of

ab-initio models, in which the final results are obtained only using theory.

The starting point of semi-empirical methods is to consider only valence electrons, that is to say those that are meaningful in the creation of chemical bonds. Core electrons are either considered by modifying the nuclear charge (and in particular by decreasing it) or by adding specific functions. This is not a too harsh approximation, since core electrons are not expected to interact with other particles and hence should not behave too much differently when other elements are close. Then, for the description of valence electrons, only a minimum basis set is employed, which is usually of Slater type, and thus of exponential kind. Furthermore, another approximation present in almost all semi-empirical methods is the Zero Differential Overlap (ZDO). This allows to greatly reduce the computational effort by not considering two-electrons integrals. In exchange to this approximation, some parameters are added in the remaining integrals. As far as such integrals are concerned, some are computed exactly, whereas others are computed thanks to parameters extracted from known data. From the choice made in the computation of them, a series of different methodologies have been developed through the years. From the ZDO, in fact, three main methods can be derived, known as the Complete Neglect of Differential Overlap (CNDO), Intermediate Neglect of Differential Overlap (INDO) and Neglect of Differential Diatomic Overlap (NDDO). Adding additional approximations a huge variety of other models can be obtained. Nevertheless, it is not of interest in this work to analyze deeply each of them.

### 3.2.1 Extended Hückel Theory

One of the most famous semi-empirical model is the Extended Hückel Theory (EHT). In it, the structure of the system is expanded in a basis set of local atomic orbitals (LCAO) [27], which are approximated by Slater-type orbitals, described by parameters which must be defined for the valence orbitals of each element. EHT represents an evolution of the Hückel theory, in the sense that, while the latter only takes into account p orbitals, and is hence restricted to planar molecules, EHT involves all valence s and p orbitals, allowing to study also non-planar systems. Furthermore, while in the Hückel theory the overlap integrals are directly set to 1 or 0, in EHT they are calculated, meaning that the ZDO approximation previously mentioned is not applied. The analysis of this section follows directly the one of [28].

Following the Hartree method, the total electronic wave function can be expressed as the product of single electron wave functions (see 3.3):

$$\psi = \psi_1(1)\psi_2(2)\dots\psi_j(n)$$

where  $n$  is the number of electrons and  $j$  represents the molecular orbital, which is the wave function for one electron moving in the field generated by the nuclei and

other electrons.

Until now, nothing has been said about the shape of such wave functions. In EHT, each of them is written as LCAO, which, as just pointed out, is built upon a minimum basis set ( $\phi_j$ , usually of Slater type) able to describe all valence orbitals (s and p orbitals of carbon for example), such that:

$$\psi_j = \sum_{r=1}^N c_{jr} \phi_r \quad (3.7)$$

where the  $c_{jr}$  are the weighting coefficients for the atomic orbitals in the molecular one.

It is then possible to express the energy of the  $j$ -th molecular orbital using the one electron Hamiltonian (see 3.2):

$$h\psi_j = \epsilon_j \psi_j$$

From it, the total energy of the system is achieved by summing up all the energies  $\epsilon_j$  obtained from Schrödinger equation. Notice that the expected value of  $\epsilon_j$  may be expressed as:

$$\epsilon_j = \frac{\langle \psi_j | h | \psi_j \rangle}{\langle \psi_j | \psi_j \rangle} = \frac{\langle \sum_{r=1}^N c_{jr} \phi_r | h | \sum_{s=1}^N c_{js} \phi_s \rangle}{\langle \sum_{r=1}^N c_{jr} \phi_r | \sum_{s=1}^N c_{js} \phi_s \rangle}$$

where it has been made use of equation 3.7.

Finally, this leads to:

$$\epsilon = \frac{\sum_{r,s=1}^N c_r^* c_s \langle \phi_r | h | \phi_s \rangle}{\sum_{r,s=1}^N c_r^* c_s \langle \phi_r | \phi_s \rangle} \quad (3.8)$$

Notice that the bracket at the denominator is the overlap integral. If the indexes are equal ( $s = r$ ), the overlap integral is assumed to be equal to 1 as normalized atomic orbitals are assumed to be used. If instead they are different, the value is comprised between 1 and 0 (notice again that in the simple Hückel theory it is either 1 or 0, i.e. overlap integrals are neglected). The bracket at the numerator, instead, is called Coulomb integral when  $s = r$ , and in this case it represents the energy of an electron experiencing the potential energy of other electrons and nuclei, or resonance integral when  $r \neq s$ , and in this case it gives the energy of an electron in a region of space in which two  $\phi$  overlap. In the Hückel theory it is assumed to be null in the latter case.

Indeed, it is possible, but will not be done here, to find the unknown coefficients by using the variational approach introduced earlier. What will be obtained at the end is a set of linear equations which are solved by means of a matrix notation (see 4.1 for the derivation of the matrices).

What is important to highlight is that, since it is a semi-empirical method, some of the resulting integrals are evaluated by means of known data, thus reducing the computational costs. To be more precise, in EHT, in the matrix notation the diagonal elements arising from the Coulomb integrals are set as the valence state ionization potentials, obtained from experiments or other simulations. Also the off-diagonal elements, related to the resonance integrals, are evaluated starting from known data, but their calculation is more complex. Of course, it is rather obvious that the EHT model is quite rough in analyzing systems of particles. However, if the data is chosen carefully, it is able to give fairly good results at a fraction of the cost of more computationally involving methods. As such, it can be one of the only alternatives for huge complexes of particles, where other tools would simply be inapplicable.

### **EHT in quantum ATK**

Within *quantum ATK*, in setting up a semi-empirical calculation it is possible to choose the EHT model, with a series of modifiable options. First of all, it is possible to choose between Müller and Hoffmann parameters, which are both advised for organic analysis on the ATK manual [29]. The choice will impact the orbitals that are used in the LCAO. Then, it is also possible to choose the weighting scheme for the orbital energies of the off-site Hamiltonian between Wolfsberg and Hoffmann. Finally, self-consistence iteration can be performed or not.

For the settings used in the analysis done with EHT in the following parts refer to table 6.1. Since no particular information are given by the manual, in general the default settings have been used.

### **3.2.2 Slater-Koster model**

The main difference of the Slater-Koster method with respect to EHT is in the evaluation of the offsite Hamiltonian. The overlap matrix, as reported in [29], is given by pairwise integrals between basis functions. Such integral are, in Slater-Koster, pre-calculated to take into account distances, orbitals combinations, element types and angular momentum. This known data is stored in tables which need to be specified. Notice that, typically, tables are generated by evaluating Hamiltonian matrix elements for a set of dimer distances or by fitting matrix elements for different lattice constants. Another thing to highlight is that, as said in the manual, EHT is a Slater-Koster model with a special fitting procedure for the matrix elements. However, Slater-Koster is not a purely wave function based model. In fact, as reported in [30], it follows the Kohn-Sham formalism of section 3.3. In that, the results given within this method are expected to be better with respect to those of EHT, and proofs of its validity are reported in [30].

For the settings used in the following by means of Slater-Koster refer to table 5.1.

### 3.3 Density functional theory

In section 3.1 wave function based models have been introduced, in order to describe semi-empirical methods. From that analysis it is now possible to move to the density functional theory (DFT), where the wave functions are substituted by the electron density  $n(\vec{r})$ . This allows to go from  $4N$  (three spatial and one spin) coordinates to  $3$ , independently on the number of electrons. This is possible thanks to the Hohenberg-Kohn theorem, which tells that all the information can be extracted from the electron density. Introducing the electron density operator:

$$\hat{n}(\vec{r}) = \sum_{i=1}^{N_{el.}} \delta(\vec{r} - \vec{r}_i)$$

which allows to get the electron density as:

$$n(\vec{r}) = \langle \psi(\vec{r}_1, \vec{r}_2, \dots, \vec{r}_N) | \hat{n}(\vec{r}) | \psi(\vec{r}_1, \vec{r}_2, \dots, \vec{r}_N) \rangle$$

it is thus possible to get every important information about the system. In particular, from a classical electrostatic analysis, the interaction term between electrons can be written (always in atomic units) as:

$$E_{hartree} = \int \int d\vec{r} d\vec{r}' \frac{1}{2} \frac{n(\vec{r})n(\vec{r}')}{|\vec{r} - \vec{r}'|}$$

The Hohenberg-Kohn theorem goes beyond that by telling that also the interaction term between electrons and ions can be expressed as a function of the charge density. Furthermore, and this can be proven by absurd, that potential is uniquely determined, except for a constant, by the ground state charge density. This means that the complete Hamiltonian of the system can be written as:

$$E[n(\vec{r})] = \hat{T}[n(\vec{r})] + \hat{V}_{int.}[n(\vec{r})] + \hat{V}_{ext.}[n(\vec{r})]$$

and that Hamiltonian is fully determined, except for a constant shift, allowing to get all the other properties of the system. Notice that changing the expression of  $V_{ext.}[n(\vec{r})]$  means having a different material. Square brackets are used to distinguish between normal functions and functionals.

In order to proceed, there are then two other important theorems. The first tells that the exact ground state is the global minimum for a given  $V_{ext.}[n(\vec{r})]$  and the  $n(\vec{r})$  which minimize the functional is the exact one. The second instead tells that the functional  $E[n(\vec{r})]$  alone is sufficient to determine the exact ground state energy and density. Indeed, in order to evaluate the charge density for the ground state it is necessary to use the variational process previously introduced.

### 3.3.1 Kohn-Sham scheme

The typical way to go in the density functional theory is by exploiting the Kohn-Sham treatment of the problem. The idea is to study the system of interacting particles by means of a system (non-existent!) of independent particles. This can be done in the case in which the resulting charge density is equal to the starting one. In the new energy functional all the required terms for the analysis are present. Namely a kinetic term  $T_S[n(\vec{r})]$ , a coulomb-like term for electrons interaction, a term with the external potential and a term for the exchange-correlation. The resulting energy for the system can be written as:

$$E_{ks}[n(\vec{r})] = T_S[n(\vec{r})] + \int d\vec{r} n(\vec{r}) V_{ext.}(\vec{r}) + \frac{1}{2} \int \int \frac{n(\vec{r})n(\vec{r}')}{|\vec{r} - \vec{r}'|} d\vec{r} d\vec{r}' + E_{xc.}[n(\vec{r})]$$

where the exchange-correlation term  $E_{xc.}$  is inserted to mimic the dependency of the various electrons. If the process is performed in the correct way, at the end the difference of energy between the fictitious system and the starting one should be equal to 0. In particular:

$$E[n_0(\vec{r})] - E_{ks}[n_0(\vec{r})] = 0$$

which can be explicitly written (without writing the dependency of the various terms on the charge density), leading to:

$$E_{xc.} = T + V_{int.} - E_{hartree}$$

The expression of the exchange-correlation term, as previously mentioned, is not known. This means that it has to be enforced by means of chosen functionals. In the Kohn-Sham treatment, at this point the kinetic term is rewritten in terms of single particle wave functions, practically going back to 3 N coordinates. This is done to make the analysis easier, since it is hard to write a "correct" expression of the functional for the kinetic energy. What is derived at the end, by applying constraints, will be the Kohn-Sham equations:

$$\left[ -\frac{1}{2} \Delta_i + V_{ext.}(\vec{r}) + \int d\vec{r}' \frac{n(\vec{r}')}{|\vec{r} - \vec{r}'|} + \frac{\delta E_{xc.}[n(\vec{r})]}{\delta n(\vec{r})} \right] \psi_i(\vec{r}) = E_i \psi_i(\vec{r}) \quad (3.9)$$

Solving this eigenvalue problem will allow, in theory, to get the same solutions which would have been obtained studying the initial problem. Practically, the results are obtained in an iterative way, starting from an initial guess for the charge density, from which the Kohn-Sham Hamiltonian is built and used to evaluate the eigenvalues and eigenfunctions, that in turn allow to find the ground state charge density that has to be close to the initial one, in order to achieve self-consistency. Usually, a faster way to complete the loop consists in replacing, at the beginning

of each iteration, a linear combination of the final charge density obtained and the previous one. Notice also that it is required to choose a basis set for the description of the kinetic term.

The advantage of the DFT approach using Kohn-Sham equation is that the results obtained are typically very accurate, with a less computational effort with respect to full Hartree-Fock treatment. Indeed, semi-empirical methods are still faster, but the quality of results of DFT is way higher, since theoretically no experimental data is used.

## DFT in ATK

The first setting which can be changed in *Quantum ATK* is the choice of the functional for the exchange-correlation term. As said earlier, in fact, the form of that functional is not known and must be enforced *a priori*. Within the tool, the available options are: local density approximation (LDA), generalized gradient approximation (GGA), meta generalized gradient approximation (MGGA) and hybrid generalized gradient approximation (HGGA). The LDA assumes variation of the density to be slow and treats the local density as a uniform electron gas [31]. This model can be improved by modifying the exchange-correlation functional to better describe the non uniform electron distribution of molecules. This can be done by including derivatives of the density, leading to the GGA method. Indeed, various formulations exist, causing GGA to be divided into different models, depending on the shape used. If, instead of the only first derivative, the second order one is taken into account, MGGA methods arise. Finally, in HGGA part of the exchange is evaluated by HF method. Again, depending on the specific model used, different HGGA methods are obtained.

The second setting gives the possibility of choosing the specific model between the various in which the precedent methods are divided. In particular, for LDA the available functionals are: HL, PW, PZ, RPA, Wigner and XA; for GGA: BLYP, BP86, BPW91, PBE, PBES, PW91, RPBE and XLYP; for MGGA: SCAN, TB09LDA; for HGGA: HSE06.

Then, it is possible to decide the pseudopotential and the basis set used for the LCAO calculation. As far as the pseudopotential is concerned, the available options are FHI, HGH, OMX, PseudoDojo and SG15. Depending on the choice made, different basis set are present. In the *ATK* manual, for GGA it is recommended to use PseudoDojo, for LDA the FHI pseudopotential is suggested [32].

While it is beyond the purpose of this part to describe in details all the specific models, it is however important to do the right decision as to get accurate and not too computationally intensive results.

First of all, between the various functionals for the exchange-correlation term, the LDA one is known to give not so accurate results. On the other hand, GGA is

able to give fairly good results, as demonstrated in [33]. MGGA only allows for small amelioration with respect to GGA whereas HGGA is the most accurate one, combining the good qualities of the previous methods with the accuracy given by the direct evaluation of a portion of the exchange-correlation term. In the following, to combine results and efficiency it has been chosen to use the GGA model.

As far as the pseudopotential is concerned, the chosen one is FHI, which, although being listed on the manual as being less accurate with respect to other models, for some materials it is expected to give good results. Furthermore, pseudodojo and SG15, that are considered to give the best results, are optimized specifically for bulk, dimer and trimer systems [32] and are therefore not expected to provide a much better analysis with respect to FHI, considering a molecule-based structure. Notice that an attempt in comparing the two potentials' results has been tried but due to the much bigger computational effort required, the simulations with pseudodojo could not be completed, thus forcing the use of FHI.

The associated basis set employed is the *doublezetapolarized*, which is recommended for FHI implementations.

A complete list of all the used settings is reported in table 6.2.

Notice that it has also been used a Van Der Waals correction to better estimate the interaction between external species and the molecule in the channel. Indeed, it is known that DFT underestimate such interactions, and better results may be obtained by introducing corrective terms. The most common resulting methods are the DFT-D2 Grimme and DFT-D3 Grimme, which are both present in *ATK*. In the first case the correction scales as a typical Van Der Waals interaction, that is to say with a power six inverse proportionality with respect to the distance, multiplied by a coefficient and an exponential term preventing the divergence of the energy [34]. In the second case, a power eight dependency is added and the parameters are made dependent on the coordination number of each atom [35]. Since no noticeable difference has been observed in the case under study, as reported in appendix B, the D2 correction has been used in the project for all the simulations.

## 3.4 Final considerations

In this chapter, a more refined procedure for the description of molecular electronic systems has been presented. Going from the most general form of the Hamiltonian representing the system and using the well established Born-Oppenheimer and mean-field approaches for the simplification of such quantum operator, the Hartree and Hartree-Fock models have been obtained. These are the starting point for both semi-empirical and ab-initio methods.

Before moving on, it is fundamental to understand really are the differences

between these two groups of tools. As stated in [36], DFT, semi-empirical self-consistent field and molecular mechanics (called force field method in ATK and not described in this work due to their poor performances) methods are the main tools used in computational chemistry. Nevertheless, the choice of the model to use must take into account the differences in performances and quality between them. There is, in fact, a trade-off to consider concerning the accuracy and the computational effort [36].

Of course, most accurate results are obtained by correlated ab-initio calculations with complex basis set. This comes, unfortunately, at the cost of an high computational power required to carry out the results, due to the calculations being performed just from first principles. In fact, as stated in [37], such tools solve the electronic Schrödinger equation with only the masses of ions and electrons as empirical inputs. As such, they rarely provide results incompatible with experiments. In the discussion made thus far, ab-initio techniques have not been presented, since simulations of that kind have not been performed in the following. Nevertheless, the DFT methodology is very close to that idea. Ideally, in fact, if the exact form of the exchange-correlation functional were known, DFT would be without doubt an ab-initio method. Unfortunately, this is not the case and some parameters, chosen from empirical data, are included in the description, causing DFT not to be purely ab-initio [37]. However, the number of such parameters is much lower than what required in semi-empirical models, and hence the quality of DFT is expected to be higher.

As far as semi-empirical methods are concerned, they are a fast but less reliable alternative to ab-initio and DFT tools [36], since they employ more approximations to reduce the number of integrals to be practically calculated and a good number of empirical data [37]. However, since their characteristics are mainly related to the quality of the that data, it is possible to achieve good results. A good practice in the use of semi-empirical methods is thus to compare, for those analysis for which it can be done, DFT results to EHT ones, for example. This will be, in fact, the procedure followed in the rest of the work.

Finally, force field based methods are the ones providing less accurate results but with a very low computational power requirements. Their use is thus not considered of interest in the following, but a more in depth description of them can be found in [37].

In the upcoming chapters, DFT, Slater-Koster and EHT will all be used for the analysis related to the sensor. In particular, as will be clearer in the following, for equilibrium studies their results will be compared in order to validate the less accurate EHT and Slater-Koster, to finally decide the tool to employ for further out-of-equilibrium studies.

## Chapter 4

# Non-Equilibrium Green's Function

In chapter 2 the toy model for the description of transport in molecular systems has been introduced. It has been stressed ever since that it is a very approximated analysis in which most of the elements have been enforced without almost any explanation.

On the approximations point of view, the most noticeable ones have been the square-well profile for the potential inside the system, the expression of the density of states, reduced to a series of Dirac delta, but also the capacitive model for the effect of an applied voltage onto the system.

Some of them have been addressed in chapter 3, where a more complete way of analyzing the energetic levels and the wave functions through the device has been presented, thus going over the main simplifications made on the Hamiltonian.

Furthermore, the models used for the simulations of the next chapters were introduced, going from the precise DFT methods to less accurate semi-empirical ones.

Different is the story for most of the concepts introduced in a forced way, like the coupling between the contacts and the channel or the broadening of the levels when such connection is established. For these characteristics of a molecule-based system it has not been yet presented a more refined model.

The purpose of this chapter is to finally give a complete description of transport in nanoscaled devices when such structures are forced in an out of equilibrium condition thanks to an applied bias between the electrodes. The main results of the toy model will be thoroughly studied and justified with a more precise model which is indeed the one on which the simulation tools for the evaluation of the  $I(V)$  characteristic are based on. In particular, as said in chapter 1, the theory which allows for such analysis is known as Non Equilibrium Green's Function approach.

Again, notice that the main goal is to give the most important concepts in the comprehension of such theory, always in the viewpoint of understanding how the simulations are performed and how to describe the derived results. Demonstration of the various formulas and theorems is thus not provided and the interested reader may find way a more complete treatment in [38], which has been used as the main source for the following analysis.

As far as the content of this chapter is concerned, in section 4.1 the matrix notation for the Schrödinger equation is presented. It will be widely employed in the following sections as a tool to simplify the analysis and also allows to conclude the discussion started in 3.2.1.

Then, in section 4.2, a generic system is considered in an equilibrium condition, in order to provide the main concepts of the theory without the complexity of having an applied voltage.

Moving on to section 4.3, here the system is brought out of equilibrium, allowing to finally get an expression for the current flowing through the system.

Finally, in section 4.4, the settings available in *ATK* for NEGF calculations are briefly discussed.

Before proceeding, it is fundamental to do some considerations. In this chapter, and in the whole work, it is assumed that the transport mechanism occurring in a system like the one under analysis is of coherent type. This means that all the dissipative/phase-breaking processes are not expected to occur within the channel and are hence limited to the contacts, where their main effect is to keep the electrons in local equilibrium.

This assumption would be greatly justified if the device studied was made of conventional semiconducting materials, where even with channel lengths in the order of few to tens of nanometers the transport is practically speaking completely ballistic. However, the channel, in this work, is constituted by a molecule, and assuming coherent transport may be risky.

A simple way to justify this choice is to take into account the toy model previously analyzed and consider the meaning of the coupling coefficients, which have been associated to two quantities called intrinsic lifetimes. It is reasonable to expect, given the size of the molecule employed in the rest of the work, that the main effect preventing the coherent transport of particles between the two ends of the device is the extension of the coupling. The weaker the molecule is connected to the contacts the higher will be the time required for electrons to flow and hence the probability of undergoing interactions with phonons and photons. In the following, since a strong coupling will be present, the electronic cloud will be greatly delocalized in the system and so phase-breaking processes are not expected to be dominant.

Indeed, this is not a complete justification and a more in depth analysis of vibrational frequencies of the molecule as well as the effect of photons would be required. Nevertheless, it is beyond the purpose of this work and most of the literature studies

regarding transport in molecule-based systems assume the Landauer-Büttiker formula retrieved at the end of this chapter to be valid in the description of transport in such devices.

## 4.1 Matrix representation of Schrödinger equation

Before beginning with the actual treatment of the NEGF methodology, it is crucial to introduce the matrix notation of Schrödinger equation. In fact, it will be the notation used for the next parts as it greatly helps in understanding all the steps of the theory.

To keep things simple lets suppose to have a 1D Schrödinger equation of the type:

$$\left[ -\frac{\hbar^2}{2m} \frac{d^2}{dx^2} + U(x) \right] \xi(x) = E\xi(x)$$

The idea is to solve it by dividing the domain into  $N$  nodes with a distance between them being expressed as  $a$ . In this way the wave function  $\xi(x)$  can be represented as a column vector  $\{\xi\}$  containing its values at each point of the discretized domain. As far as the Hamiltonian operator is concerned, the procedure implies the use of the finite difference technique. The second order derivative can be written as:

$$\left( \frac{\partial^2 \xi}{\partial x^2} \right)_{x=x_n} \longrightarrow \frac{1}{a^2} [\xi(x_{n+1}) - 2\xi(x_n) + \xi(x_{n-1})]$$

whereas the potential related term simply becomes:

$$U(x)\xi(x) \longrightarrow U(x_n)\xi(x_n) = U_n\xi_n$$

Introducing then:

$$t_0 = \frac{\hbar^2}{2ma^2}$$

one gets:

$$H = \begin{bmatrix} 2t_0 + U_1 & -t_0 & 0 & \dots & \dots & \dots & 0 \\ -t_0 & 2t_0 + U_2 & -t_0 & 0 & \dots & \dots & 0 \\ 0 & -t_0 & 2t_0 + U_3 & -t_0 & 0 & \dots & 0 \\ \dots & \dots & \dots & \dots & \dots & \dots & \dots \\ 0 & \dots & \dots & \dots & 0 & -t_0 & 2t_0 + U_N \end{bmatrix}$$

which leads to:

$$[H]\{\xi\} = E\{\xi\} \tag{4.1}$$

where  $[H]$  is the Hamiltonian matrix.

Of course, the results obtained through this method will be just an approximation of the right solution, and the accuracy is a function of the size of the steps in which the domain has been divided. The smaller the step  $a$  the bigger in size will be the matrices and the more precise the retrieved results will be. Notice also that, while the obtained notation has been derived in a 1D domain for sake of clarity, it can be generalized to a 3D case.

It may be interesting, at this point, to apply this methodology to the analysis of section 3.2.1, where it has been said the set of linear equations derived through EHT is solved using a matrix notation. The followed procedure is again the one of [28].

The starting point is equation 3.8. Using the symbols  $S_{rs}$  to represent the overlap integrals and  $H_{rs}$  to represent the Coulomb or resonance integrals, it is possible to rewrite that equation as:

$$\epsilon = \frac{\sum_{r,s=1}^N c_r^* c_s H_{rs}}{\sum_{r,s=1}^N c_r^* c_s S_{rs}}$$

As previously said the goal is to find the various coefficients, which can be found through a variational approach. The first step is to derive the energy with respect to the coefficients (in theory that derivative should also be performed for the complex conjugate of the coefficients but it would lead to the same solution):

$$\frac{\partial \epsilon}{\partial c_t} = 0$$

for  $t = 1, 2, 3, \dots, N$ . This can be achieved by rewriting the problem as:

$$\epsilon \sum_{r,s=1}^N c_r^* c_s S_{rs} = \sum_{r,s=1}^N c_r^* c_s H_{rs}$$

The differentiation leads to:

$$\epsilon \sum_r c_r^* S_{rt} = \sum_r c_r^* H_{rt}$$

which, by taking the complex conjugate of both sides and rearranging the terms, provides:

$$\sum_r c_r (H_{tr} - S_{tr} \epsilon) = 0 \tag{4.2}$$

The matrix notation allows to solve this set of homogeneous linear equations. At this point 4.2 is written explicitly, so that the first equation is related to  $t = 1$ , the

second to  $t = 2$  and so on:

$$\begin{aligned}
 c_1 H_{11} + c_2 H_{12} + \dots c_N H_{1N} &= c_1 S_{11} \epsilon + c_2 S_{12} \epsilon + \dots c_N S_{1N} \epsilon \\
 c_1 H_{21} + c_2 H_{22} + \dots c_N H_{2N} &= c_1 S_{21} \epsilon + c_2 S_{22} \epsilon + \dots c_N S_{2N} \epsilon \\
 &\vdots \\
 c_1 H_{N1} + c_2 H_{N2} + \dots c_N H_{NN} &= c_1 S_{N1} \epsilon + c_2 S_{N2} \epsilon + \dots c_N S_{NN} \epsilon
 \end{aligned}$$

This set of equations can be represented in a matrix notation as:

$$[H - S\epsilon]\{C'\} = 0$$

and is valid for the orbital with energy  $\epsilon$ . Considering all the molecular orbitals:

$$HC = SCE \tag{4.3}$$

where  $H$  is a square matrix containing the  $H_{rs}$  integrals,  $C$  is the matrix of coefficients for the atomic orbitals,  $S$  represents the overlap integrals and  $E$  is the diagonal matrix of orbital energies. Each column of  $C$  is the  $C'$  that defines one molecular orbital. The size of these matrices equals the number of atomic orbitals used for the LCAO of the molecule analyzed.

Indeed, the specific expression and evaluation of 4.3 depends on the method used. In EHT for example the overlap matrix is evaluated whereas in HT it is either 1 or 0.

One could argue, at this point, that the matrix notation of 4.3 is not really equivalent to the one of 4.1. In fact, while the latter consists of the values that the wave function  $\xi$  has in every point of the discretized domain, in the former one  $C$  is related to the coefficients of the expansion used to represent the wave functions. In truth, the expression of 4.3 can be seen as a generalization of 4.1, where the choice of the basis function for the representation of the wave functions of the system is arbitrary. If chosen in the right way, just a few terms will be necessary to correctly reproduce the shape of the wave functions of the system, thus reducing significantly the size of the matrices of the problem with respect to the ones that would be obtained discretizing the domain as done in the beginning of this section.

## 4.2 Equilibrium analysis

This section focuses on an equilibrium condition for the system and allows for a preparatory and simple introduction to the main concepts on which the full theory is based on, without having to deal with the additional complexity of working with an applied voltage. In order to provide an even simpler approach a device with just one contact is first considered, to then move to a two terminals one. Moreover, some important quantities, namely the electron density and the density of states, are presented always in an equilibrium condition.

### 4.2.1 One contact case

To begin with the NEGF theory, a good starting point is to consider a system formed by a channel and a single contact, and more precisely without having a connection between the two. As usual, in the contact electrons will have specific wave functions  $\{\Phi_R\}$  that satisfy Schrödinger equation:

$$[EI_R - H_R]\{\Phi_R\} = \{0\} \quad (4.4)$$

which has been written in a matrix form and where  $I_R$  is the identity matrix (if the overlap integrals are neglected the right hand side of 4.3 becomes an identity matrix) of the same size ( $R \times R$ ) of the Hamiltonian.

The first step consists in rewriting the problem by introducing a matrix  $\eta$  with small infinitesimal positive entries on the left side to represent the extraction of electrons from the contact and that is expected to be counterbalanced by a term on the right hand side to describe the reintroduction of them from external sources. These term are considered to justify the characteristic of the contact of being a reservoir, thus able to provide ideally an infinite number of electrons without modifying its electrochemical potential and while their introduction seems to be forced, they will nevertheless not be present in the final results.

At this point equation 4.4 becomes:

$$[EI_R - H_R + i\eta]\{\Phi_R\} = \{S_R\} \quad (4.5)$$

It is important to highlight that the problem under analysis in this step is quite the opposite of what described in the previous chapter. In fact, it is now of interest to know how the system respond to an external stimulus, not how the system behaves in the absence of it.

Typically, the use of Schrödinger equation is dictated by the requirement of finding the electronic properties of a closed system, i.e. a system not able to communicate with the external world, such as the eigenvalues and the eigenfunctions. In the case under analysis, instead, the system is open and as such able to communicate with the contacts. Therefore, the energy  $E$  present in the various formulas is not an eigenenergy, but an independent variable that is forced and known *a priori*, representing the energy of excitation from external sources. The  $\{\Phi_R\}$  are the eigenfunctions of  $H_R$  that are different from zero when the forced energy matches one of the eigenenergies of  $[H_R]$ .

When the contact is coupled to the channel, its wave functions will overlap onto the channel causing the excitation of scattered waves  $\chi$ . The channel is described by the Hamiltonian  $H$  of size  $(dx \times dx)$  and by the wave function  $\psi$  of size  $(dx \times 1)$ . The complete wave function will satisfy the composite Schrödinger equation for the system, which may be written as:

$$\begin{bmatrix} EI_R - H_R + i\eta & -\tau^+ \\ -\tau & EI - H \end{bmatrix} \begin{Bmatrix} \Phi_R + \chi \\ \psi \end{Bmatrix} = \begin{Bmatrix} S_R \\ 0 \end{Bmatrix} \quad (4.6)$$

where  $\tau$  is called coupling Hamiltonian and is of size  $(dxR)$ . The diagonal elements in 4.6 represent the contact and the channel alone, whereas the off-diagonal terms are related to the interaction between the two.

Using equation 4.5, it is possible to eliminate  $S_R$  from the analysis, obtaining:

$$[EI_R - H_R + i\eta]\{\chi\} - [\tau^+]\{\psi\} = \{0\}$$

$$[EI - H]\{\psi\} - [\tau]\{\chi\} = [\tau]\{\Phi_R\}$$

Expressing  $\chi$  from the first equation:

$$\{\chi\} = [EI_R - H_R + i\eta]^{-1}\tau^+\{\psi\} = G_R\tau^+\{\psi\}$$

it is possible to rewrite the second one, getting:

$$[EI - H - \tau G_R\tau^+]\{\psi\} = [EI - H - \Sigma]\{\psi\} = \{\tau\Phi_R\} = \{S\}$$

So, to summarize, the channel connected to a contact can be studied with a Schrödinger equation of the form:

$$[EI - H - \Sigma]\{\psi\} = \{S\} \tag{4.7}$$

with:

$$\Sigma = \tau G_R\tau^+ \quad S = \tau\Phi_R \tag{4.8}$$

Notice that  $G_R$  represents a property of the isolated contact (it only depends on quantities related to the reservoir) and is referred to as the Green's function for the contact. Its meaning will be discussed in section 4.2.2.

From the just obtained equations, it may seem that the evaluation of  $\Sigma$  and  $S$  is not that easy, as the size of  $G_R$  is related to the size of the reservoir. A way to proceed is to note that the matrix  $\tau$  is of size  $(dxR)$  but in real space it only couples the  $r$  surface elements next to the channel. Therefore  $G_R$  can be reduced to  $g_r$ , which is of size  $(rxr)$ , involving just the  $r$  points at the surface. In this viewpoint also the contact wave function  $\Phi_R$  is reduced to a subset  $\phi_R$  of it of size  $(rx1)$ .

The result achieved is already quite interesting: a channel with an Hamiltonian  $H$  of size  $(dxd)$  is coupled to a contact with an  $(RxR)$  Hamiltonian, with  $R \gg d$ . Nevertheless, it has been shown that the effect of the reservoir can be described through a self-energy matrix  $\Sigma$  of size  $(dxd)$  and a source term  $S$  of size  $(dx1)$ , evaluated by:

$$\Sigma = \tau g_r\tau^+ \quad S = \tau\phi_R$$

## 4.2.2 Additional quantities

Having introduced some of the components on which the NEGF methodology is based on, it is now of interest to describe thoroughly how the concepts of electron density and density of states are expressed in the new framework. This will allow to introduce a very important quantity known as the density matrix, which evaluation is the central problem in non-equilibrium analysis, as all the quantities related to a system can be obtained exploiting it. Furthermore, a more concrete definition of the Green's functions and of the self-energies is provided to understand where the concept of broadening enforced in the toy model belongs to.

### Electron density and density matrix

In the previous chapter it has been stressed the role played by the electron density in DFT for the evaluation of all the important quantities related to a system. Its importance is inherited also in the NEGF analysis.

It is known that, at equilibrium, the electron density can be evaluated as the sum of the probability density of each occupied eigenstate  $\alpha$ . In general, since the working temperature is different from zero, it is necessary to make use of the Fermi function, obtaining;

$$n(\vec{r}) = \sum_{\alpha} |\Phi_{\alpha}(\vec{r})|^2 f_{FD}(\epsilon_{\alpha} - \mu) \quad (4.9)$$

It is here of interest to know if it is possible to write the wave function  $\Psi(\vec{r})$  for the system as the expansion of the basis functions being made of system eigenfunctions in such a way that its squared magnitude is the electron density. Ideally this would lead to:

$$\Psi(\vec{r}) = \sum_{\alpha} C_{\alpha} \Phi_{\alpha}(\vec{r})$$

with:

$$|C_{\alpha}|^2 = f_{FD}(\epsilon_{\alpha} - \mu)$$

However this is not correct. In fact, it gives:

$$n(\vec{r}) = |\Psi(\vec{r})|^2 = \sum_{\alpha} \sum_{\beta} C_{\alpha} C_{\beta}^* \Phi_{\alpha}(\vec{r}) \Phi_{\beta}(\vec{r})$$

which is correct only if:

$$|C_{\alpha}|^2 = f_{FD}(\epsilon_{\alpha} - \mu) = f_{\alpha} \quad C_{\alpha} C_{\beta}^* = 0$$

This is not possible if  $C_{\alpha}, C_{\beta}$  are ordinary number. The right thing to do is to write a complete matrix  $\rho(\alpha, \beta)$  known as the density matrix which expresses the correlation  $C_{\alpha} C_{\beta}^*$  between each pair of coefficients, in such a way that it is null

whenever  $\alpha = \beta$ . It is therefore obvious that the diagonal elements of the density matrix are equal to:

$$\rho(\alpha, \alpha) = f_{FD}(\epsilon_\alpha - \mu)$$

whereas the off-diagonal terms are null. It is then possible to write:

$$n(\vec{r}) = \sum_{\alpha} \sum_{\beta} \rho(\alpha, \beta) \Phi_{\alpha}(\vec{r}) \Phi_{\beta}^*(\vec{r})$$

which, by exploiting a transformation from the eigenstates representation to a real space representation of the density matrix, given by:

$$\tilde{\rho}(\vec{r}, \vec{r}') = \sum_{\alpha} \sum_{\beta} \rho(\alpha, \beta) \Phi_{\alpha}(\vec{r}) \Phi_{\beta}^*(\vec{r}')$$

allow to write the electron density as its diagonal elements:

$$n(\vec{r}) = [\rho(\vec{r}, \vec{r}')]_{\vec{r}'=\vec{r}}$$

where  $\rho$  is now expressed in real space and not in the eigenstate base.

What has been obtained comes with the fundamental result that the density matrix at equilibrium can be written as the Fermi function of the Hamiltonian matrix:

$$\rho = f_{FD}(H - \mu I)$$

which is verified in any representation. Indeed, the density matrix looks very different depending on what basis functions are used. It can be diagonal or not, but that does not change the fact that the diagonal elements represent the electron density and, as such, their summation, also called trace, provides the total number of electrons. It is important not to think, however, that the off-diagonal elements are not important. In fact, their presence allows to correctly go to one basis to another.

It is also necessary to remind that in quantum mechanics to every observable is associated an operator for which it can be found a matrix representation. It is possible to write, with the just obtained results:

$$\langle A \rangle = \text{Trace}[\rho A] \tag{4.10}$$

Meaning that, even if the system is out of equilibrium, assuming that the density matrix is known, it is possible to evaluate the expected value for any observable.

### Local density of states

In chapter 2 it has been demonstrated that a 0D system has a density of states made of Dirac's deltas centered around the energetic positions of the eigenvalues of

the system. That was not the full picture. It is, in fact, necessary to weight each state by the fraction of its squared wave function that resides in the channel, in order to take into account the spatial distribution of states.

Since the reservoir states have wave functions that are partially or completely extending in the channel, the resulting DOS will not be anymore as simple as a series of deltas.

In general it is possible to define a local density of states (LDOS) that weights each level by the square of its wavefunction at the location  $\vec{r}$ :

$$D(\vec{r}; E) = \sum_{\alpha} |\Phi_{\alpha}(\vec{r})|^2 \delta(E - \epsilon_{\alpha})$$

which can be viewed as the diagonal element of a quantity known as the spectral function:

$$A(\vec{r}, \vec{r}'; E) = 2\pi \sum_{\alpha} \phi_{\alpha}(\vec{r}) \delta(E - \epsilon_{\alpha}) \phi_{\alpha}^*(\vec{r}') \quad (4.11)$$

just as the electron density can be viewed as the diagonal element of the density matrix. It can be shown, in a similar fashion to what done with the density matrix, that the spectral function may be written as:

$$[A(E)] = 2\pi \delta(E[I] - [H]) \quad (4.12)$$

and its evaluation can be performed by exploiting the known expression for the Dirac delta function:

$$2\pi \delta(x) = \lim_{\epsilon \rightarrow \eta} \frac{2\epsilon}{x^2 + \epsilon^2} = \frac{i}{x + i\eta} - \frac{i}{x - i\eta}$$

$$2\pi \delta(E - \epsilon_{\alpha}) = \lim_{\eta \rightarrow 0^+} \left[ \frac{2\eta}{(E - \epsilon_{\alpha})^2 + \eta^2} \right] = \frac{i}{E - \epsilon_{\alpha} + i0^+} - \frac{i}{E - \epsilon_{\alpha} - i0^+}$$

to write:

$$\delta(EI - H) = \frac{i}{2\pi} \{ [(E + i\eta)I - H]^{-1} - [(E - i\eta)I - H]^{-1} \} \quad (4.13)$$

where  $\eta$  denotes a positive infinitesimal. Using equations 4.12 and 4.13 it is then possible to rewrite the spectral function as:

$$A(E) = i[G(E) - G^+(E)] \quad (4.14)$$

where:

$$G(E) = [(E + i\eta)I - H]^{-1} = G^R(E)$$

$$G^+(E) = [(E - i\eta)I - H]^{-1} = G^A(E)$$

are known as the retarded (already defined in the previous section) and advanced Green's functions, between which there exists the relation:

$$G^A = (G^R)^\dagger$$

Within this framework it is possible to rewrite the density matrix as:

$$[\rho] = \int_{-\infty}^{+\infty} dE f_{FD}(E - \eta) \delta([EI - H]) = \int_{-\infty}^{+\infty} \frac{dE}{2\pi} f_{FD}(E - \eta) [A(E)] \quad (4.15)$$

This allow to simplify the analysis, even if at a first glance it may seems that there's an extra integration over the energies which has to be done in addition to an inversion of a matrix. The power of this new expression for the density matrix is that it reduces the complexity by exploiting a minor dimensionality of the various matrices.

### Green's function and Self-Energy

Until now nothing has been said about the Green's functions and the self-energies. The first just seems to be introduced for the mere purpose of expressing the spectral function in a different way whereas the second resulted to be necessary in Schrödinger equation to take into account for the presence of the contacts. However, both of them have a specific physical meaning on which this part will focus on.

It will be shown that the Green's function (and in particular the retarded one) can be seen as the impulse response of Schrödinger equation. On the other hand the self-energy is responsible for the broadening effect on the density of states introduced in a forced way, and not really justified, in the toy model.

To show these properties it is required to work with the Fourier transform of  $G(E)$ , which provides (in the eigenstates basis):

$$[\tilde{G}^R(t)] = \int_{-\infty}^{+\infty} \frac{dE}{2\pi\hbar} e^{+iEt/\hbar} [G(E)]$$

Notice that the superscript "R" denotes that it is a retarded Green's function, which is null for  $t < 0$ . It can be verified that the diagonal elements of this function satisfy:

$$(i\hbar \frac{\partial}{\partial t} - [H])[\tilde{G}^R(t)] = [I]\delta(t)$$

which tells that the Green's function represents the response of Schrödinger equation to the impulse represented by  $[I]\delta(t)$ . Indeed, mathematically there also exists an advanced version that does not even a physical meaning but just a mathematical one.

Similarly, supposing that the self-energy is independent on the energy to simplify the analysis (and therefore both  $[H]$  and  $[\Sigma]$  are numbers and not matrices), it is possible to write:

$$(i\hbar \frac{\partial}{\partial t} - \epsilon - \Sigma)[\tilde{G}^R(t)] = \delta(t)$$

with solution:

$$\tilde{G}^R(t) = -\frac{i}{\hbar} e^{-i\epsilon' t/\hbar} e^{-\gamma t/2\hbar} \delta(t) \quad (4.16)$$

with:

$$\epsilon' = \epsilon + \text{Re}\Sigma \quad \gamma = -2\text{Im}\Sigma$$

Showing that the real part of the self-energy causes a shift in the device energy level from  $\epsilon$  to  $\epsilon'$  while the imaginary part has the effect of giving the eigenstates a finite lifetime. This is evident when the squared magnitude is taken into. Notice that this effect is reflected also on the density of states. Using equation 4.16 and Fourier transforming it one gets:

$$G(E) = \frac{1}{E - \epsilon' + i\gamma/2}$$

so that:

$$\frac{A(E)}{2\pi} = D(E) = \frac{\gamma}{(E - \epsilon')^2 + (\gamma/2)^2}$$

which really represents the Lorentzian profile forced in the toy model, where the width is twice the imaginary part of the self-energy. It is important, however, not to be fooled into thinking that this is a general result. That particular profile has been obtained thanks to the choice of supposing the self-energy independence on the energy.

In general, the self-energy is a matrix and one can define a broadening matrix equal to its antihermitian component:

$$\Gamma(E) = i[\Sigma(E) - \Sigma^+(E)] \quad (4.17)$$

which is responsible for broadening, whereas the hermitian component:

$$\Sigma_H(E) = \frac{1}{2}[\Sigma(E) + \Sigma^+(E)]$$

can be viewed as the Hamiltonian  $H$  correction. Overall, it is possible to write:

$$H + \Sigma(E) = [H + \Sigma_H(E)] - \frac{i\Gamma(E)}{2}$$

### 4.2.3 Two contacts case

The analysis performed in 4.2.1 can be quite easily extended to the case of interest, which is the one where the channel is connected to a source and a drain. As done before, it is assumed that the source and the drain can be described independently with wave functions  $\{\Phi_1\}$  and  $\{\Phi_2\}$  which satisfy Schrödinger equation for the isolated contacts configuration. Once connected to the channel, the whole system will be represented by:

$$\begin{bmatrix} EI - H_1 + i\eta & -\tau_1^+ & 0 \\ -\tau_1 & EI - H & -\tau_2 \\ 0 & -\tau_2^+ & EI - H_2 + i\eta \end{bmatrix} \begin{Bmatrix} \Phi_1 + \chi_1 \\ \psi \\ \Phi_2 + \chi_2 \end{Bmatrix} = \begin{Bmatrix} S_1 \\ 0 \\ S_2 \end{Bmatrix}$$

Proceeding in the same way as in the one-contact case, what is obtained is:

$$[EI - H - \Sigma_1 - \Sigma_2]\{\psi\} = \{S\}$$

with:

$$\begin{aligned} \Sigma_1 &= \tau_1 G_1 \tau_1^+ & \Sigma_2 &= \tau_2 G_2 \tau_2^+ \\ G_1 &= [EI - H_1 + i\eta]^{-1} & G_2 &= [EI - H_2 + i\eta]^{-1} \end{aligned}$$

The source term is:

$$\{S\} = \tau_1 \{\Phi_1\} + \tau_2 \{\Phi_2\} \quad (4.18)$$

The broadening matrices can instead be evaluated using equation 4.17 and 4.8, giving:

$$\Gamma_1 = \tau_1 A_1 \tau_1^+ \quad \Gamma_2 = \tau_2 A_2 \tau_2^+ \quad (4.19)$$

where the two spectral functions are evaluated using equation 4.14.

Notice that the Green's function can be exploited to write:

$$\{\psi\} = G\{S\} \quad (4.20)$$

This relation will be useful in the following.

## 4.3 Out of equilibrium analysis

The previous section allowed to introduce the main concepts of the NEGF theory in an equilibrium condition. Of course, the true power of this approach comes in out of equilibrium studies. This section focuses on that condition but supposing a coherent transport, as discussed at the beginning of this chapter.

### 4.3.1 Density matrix out of equilibrium

Previously it has been presented the procedure for the evaluation of the density matrix at equilibrium. Now the problem is shifted to its evaluation in an out of equilibrium condition, as, knowing the density matrix, everything about the system can also be evaluated. The device is now connected to two terminals and a voltage is applied, causing a shift in the position of the Fermi levels. The solution may be quite hard but it is greatly simplified in the assumption of coherent transport made.

Using the results obtained at equilibrium in the two contacts case, it is possible to evaluate the density matrix out of equilibrium using the Green's function to express the channel wave function in terms of the source terms (see equation 4.20), and multiply it by  $\psi^+$ :

$$\{\psi\}\{\psi\}^+ = G\{S\}\{S\}^+G^+ \quad (4.21)$$

where:

$$SS^+ = \tau_1\Phi_1\Phi_1^+\tau_1^+ + \tau_2\Phi_2\Phi_2^+\tau_2^+ + \tau_1\Phi_1\Phi_2^+\tau_2^+ + \tau_2\Phi_2\Phi_1^+\tau_1^+$$

in which the cross terms are null since the two wave functions (remember that  $\Phi_1$  and  $\Phi_2$  are the wave functions before connecting the contacts to the channel) are physically disconnected. The other terms are evaluated (using 4.11) as:

$$\{\Phi_1\}\{\Phi_1^+\} = \int \frac{dE}{2\pi} f_{FD,1}(E)[A_1(E)] \quad (4.22)$$

Reminding that the density matrix can be written as:

$$[\rho] = \sum_{\alpha} f_{FD}(\epsilon_{\alpha} - \mu)\{\psi\}\{\psi\}^+$$

it is possible to write:

$$\rho = \int \frac{dE}{2\pi} \{[G\tau_1A_1\tau_1^+G^+]f_{FD,1} + [G\tau_2A_2\tau_2^+G^+]f_{FD,2}\} \quad (4.23)$$

This expression can be simplified using the expression of the broadening matrices (equation 4.19) to write:

$$G^< = G\Sigma^<G^+ \quad (4.24)$$

with:

$$[\Sigma^<] = [\Gamma_1]f_{FD,1} + [\Gamma_2]f_{FD,2} \quad (4.25)$$

leading to:

$$[\rho] = \int \frac{dE}{2\pi} [G^<]$$

Substituting equation 4.25 into 4.24, one gets:

$$[G^<] = [A_1]f_{FD,1} + [A_2]f_{FD,2}$$

where:

$$A_1 = G\Gamma_1G^+ \quad A_2 = G\Gamma_2G^+$$

This means that, in the coherent transport assumption, the density matrix out of equilibrium is simply obtained by dividing the spectral function into a component related to the source and one to the drain. This result represents a sort of superposition of effects and may seem like a violation of Pauli's exclusion principle, as in theory one wave function coming from a contact should block the one coming from the other contact. It is possible to show (refer to [38] for a detailed justification) that the hypothesis of coherent transport ensures that this is not the case.

### 4.3.2 Inflow/outflow

It is finally time to derive the expression for the current flowing at the terminals, starting again from a one-contact system. The idea is to evaluate it by reminding that it can be expressed as the electron flux, which can be evaluated as:

$$I = \frac{d}{dt}\psi^+\psi$$

The right hand side can be derived from the time-dependent Schrödinger equation:

$$i\hbar \frac{d}{dt} \begin{Bmatrix} \psi \\ \Phi_R + \chi \end{Bmatrix} = \begin{bmatrix} H & \tau \\ \tau^+ & H_R - i\eta \end{bmatrix} \begin{Bmatrix} \psi \\ \Phi_R + \chi \end{Bmatrix}$$

and considering that:

$$Trace[\psi\psi^+] = Trace[\psi^+\psi] = \psi^+\psi$$

where the last one is just a number and so it is not important to take the trace of it. It is possible to show that what is obtained through the time derivative is:

$$I = \frac{d}{dt}\psi^+\psi = \frac{Trace[\psi^+\tau\Phi_R - \Phi_R^+\tau^+\psi]}{i\hbar} - \frac{Trace[\chi^+\tau^+\psi - \psi^+\tau\chi]}{i\hbar}$$

Where the first term represents an inflow due to the incident wave  $\{\Phi_R\}$  whereas the second an outflow due to the scattered wave  $\{\chi\}$ . Using the expressions of the source term (equation 4.18) it is possible to rewrite the inflow as:

$$inflow = Trace[S^+G^+S - S^+GS]/i\hbar = Trace[SS^+A]/\hbar$$

where  $SS^+$ , using equation 4.22, can be written as:

$$\int \frac{dE}{2\pi} f_{FD}(E - \mu) \tau A_R \tau^+ = \int \frac{dE}{2\pi} f_{FD}(E - \mu) [\Gamma] \quad (4.26)$$

so that:

$$Inflow = \frac{1}{\hbar} \int \frac{dE}{2\pi} f_{FD}(E - \mu) Trace[\Gamma A]$$

Similarly, for the output:

$$Outflow = \frac{1}{\hbar} \int \frac{dE}{2\pi} Trace[\Gamma G^<]$$

At equilibrium, as expected, the two fluxes are equal, to ensure a null total current.

Moving now to the two contacts configuration, the current at the terminal  $i$  may be expressed as:

$$I_i = \frac{Trace[\psi^+ \tau_i \Phi_i - \Phi_i^+ \tau_i^+ \psi]}{i\hbar} - \frac{Trace[\chi_i^+ \tau_i^+ \psi - \psi^+ \tau_i \chi_i]}{i\hbar}$$

Making use of the relations  $\psi = GS$  and  $S_i = \tau_i \{\Phi_i\}$  it is possible to write:

$$Inflow = Trace[S^+ G^+ S_i - S_i^+ GS] / i\hbar = Trace[S_i S_i^+ A] / \hbar$$

Since (for two terminals)  $S = S_1 + S_2$  and  $S_1^+ S_2 = S_2^+ S_1 = 0$ .

Therefore, for the  $i$ -th terminal:

$$Inflow = \frac{1}{\hbar} \int \frac{dE}{2\pi} f_{FD,i}(E) Trace[\Gamma_i A]$$

$$Outflow = \frac{1}{\hbar} \int \frac{dE}{2\pi} Trace[\Gamma_i G^<]$$

Finally, considering that the current is given by the difference between inflow and outflow:

$$I_i = \left(-\frac{q}{\hbar}\right) \int_{-\infty}^{\infty} \frac{dE}{2\pi} \tilde{I}_i(E) \quad (4.27)$$

with:

$$\tilde{I}_i(E) = Trace[\Gamma_i A] f_{FD,i}(E) - Trace[\Gamma_i G^<] \quad (4.28)$$

### 4.3.3 Landauer-Büttiker

It has been shown that the current at the terminal  $i$  can be written as the difference between an inflow and an outflow, giving equation 4.27. It is possible to rewrite everything in order to get:

$$\bar{I}_1 = Trace[\Gamma_1 A_2][f_1(E) - f_2(E)] = \bar{T}_{12}(E)[f_1(E) - f_2(E)]$$

$$\bar{I}_2 = \text{Trace}[\Gamma_2 A_1][f_2(E) - f_1(E)] = \bar{T}_{21}(E)[f_2(E) - f_1(E)]$$

Since the currents at the terminals are expected to be equal, it is necessary that  $\text{Trace}[\gamma_1 A_2] = \text{Trace}[\gamma_2 A_1]$ . This leads, taking into account the spin degeneracy through a factor of two, to the Landauer-Büttiker formula:

$$I = \frac{2q}{h} \int_{-\infty}^{\infty} dE T(E)[f_1(E) - f_2(E)] \quad (4.29)$$

where:

$$T(E) = \text{Trace}[\Gamma_1 G \Gamma_2 G^+] = \text{Trace}[\Gamma_2 G \Gamma_1 G^+] \quad (4.30)$$

is called the transmission function. The idea is that the system can be seen as a semi-permeable membrane that separates two reservoirs, and the transmission function is a measure of its permeability for electrons with energy  $E$ .

The reason for which the transmission function has been introduced is that it links the NEGF approach with the transmission formalism, that is typically employed to keep a simple analysis of devices in the assumption of coherent transport. Furthermore, employing the concept of transmission function allows for a better understanding of the properties of the sensor in the following chapters.

### 4.3.4 Effect of voltage on the device

The analysis done up to now may seem complete but it is still lacking of a crucial element, that is the effect of the applied bias on the channel. Obviously, at the electrodes, its effect is to shift the position of the Fermi levels as to create a difference between them equal to the applied voltage, but nothing has been said on how this voltage modifies the channel.

The presence of the applied voltage can be considered by modifying the Hamiltonian, which can now be expressed as the sum of the Hamiltonian  $H_0$  and a self-consistent potential  $U([\Delta\rho])$  which represents the average potential that an electron feels due to the variation of the density matrix.

Initially, the electron density is evaluated from the diagonal elements of the density matrix. Then, it is used in Poisson equation to calculate the potential that is inserted in the Hamiltonian in order to recalculate the electron density. A full self-consistent calculation of NEGF transport equations and Poisson equation may be quite involving computationally speaking, so usually a "reasonable" potential profile is assumed.

## 4.4 NEGF in ATK

To conclude the chapter, the goal of this section is to present the settings used for the simulations in *ATK*. Notice that the settings used for the evaluation of the

Hamiltonian are not reported here. Indeed, the evaluation of the elements of the Hamiltonian matrix depends on the method used and an extensive analysis of them has already been done in the previous chapter.

First of all, since it has been said that the NEGF transport equations need to be solved self-consistently with Poisson equation, it is possible to modify the way *ATK* solves it. Among the available choices, FFT and FFT2D are based on the fast Fourier transform. As such they should not be used for calculations of non-periodic systems like molecule-based ones. The other three methods, [Parallel] Direct, [Parallel] Conjugate gradient and Multi-grid, are instead based on a real space finite difference method and are thus suited for the system under analysis in this thesis. In the *ATK* manual [39] it is stated that the conjugate gradient method has similar accuracy with respect to the multi-grid one but, for parallel calculations, can be much faster than the latter. The direct solver, instead, is more precise at the cost of slower computations. Considering these characteristics, it has been chosen to proceed with the conjugate gradient method.

Associated to the Poisson solver one should also set the boundary conditions for the solution of that equation. In the manual it is specified that boundary conditions within NEGF calculations are unique and different with respect to what the user may think. In fact, the electrodes are considered by solving a bulk problem for the fully periodic electrode cell, and hence periodic boundary conditions are imposed for them. Instead, for the channel itself it is possible to choose either Neumann or Dirichlet boundary conditions, with specific characteristics reported in the manual. For the case of a molecule the correct choice is Dirichlet boundary condition.

Then, in the device algorithm and contour integral sections it is possible to choose the way in which the initial guess for the density matrix, the self-energies and the density matrix under applied bias are computed. Considering that these options only modify the way equations are solved and are hence not dependent on a great extent on the structure used, default settings have been employed. Also the rest of the settings associated to numerical accuracy have been kept unchanged.

# Chapter 5

## System design

Having described the theory behind transport in molecular systems and justified most of the settings later employed, it is finally time to move to the practical part of the work.

The starting point for the realization of a sensor based on a molecule is the design of the structure, commencing from the choice of the molecule, to then study what is the best configuration for such molecule in terms of orientation and distance from the electrodes. The purpose of this chapter is exactly to fulfill these requirements. In particular, in section 5.1, the employed molecule is presented, whereas in section 5.2 preliminary information about the simulations' settings for this chapter and the description of the various interaction phenomena which may occur between the molecule and the contacts are introduced. Then, different geometries are analyzed in sections 5.3 and 5.4, in order to finally decide what the most promising structure is, with the final considerations drawn in section 5.5.

### 5.1 Fullerene C<sub>28</sub>

The choice of the molecule to be used in the channel is of course the primary step. In this case, the system chosen is a fullerene. Fullerenes are one of the allotropes, together with diamond, graphite and graphene, of carbon. In particular, in a fullerene carbon atoms are  $sp^2$  hybridized (actually, due to the fact that the neighboring region of each carbon atom is not flat, the actual hybridization is assumed to fall between  $sp^2$  and  $sp^3$  by some [40]) and hence bonded through double or single bonds to create either a closed cage ("buckyballs") or a cylindrical tube ("carbon nanotubes") [41]. Usually, the name fullerene is used to directly identify the cage-like structures, as the name is derived from Buckminster Fuller, famous for his domes, and buckminsterfullerene was the name used to identify the C<sub>60</sub> molecule [41].

Two classes of fullerenes may be identified: classical fullerenes, in which carbon atoms are organized to form only hexagons and pentagons, and non-classical fullerenes, in which other shapes are present. Even though these two categories exist, classical fullerenes are typically the preferred choice in applications. In fact, the hexagons and pentagons configuration results to be the one minimizing the potential energy for the system, thus making the obtained structures more stable. Two rules are then used to predict the stability of a fullerene in nature: the isolated pentagons rule (IPR) and the pentagons adjacency penalty rule (PAPR). IPR is satisfied only starting from fullerene  $C_{60}$ , whereas PAPR holds for all the fullerenes starting from the  $C_{24}$ . IPR, as reported in [42], tells that a fullerene made of pentagons and hexagons prefers the configuration in which all the pentagons are separated by hexagons. While, in fact, hexagons tends to minimize the energy of the system, pentagons are the cause of the curvature and so of the strain of the system. Of course, for smaller fullerenes that rule can not be satisfied and so the preferred configurations tend to have the smaller number of adjacent pentagons as possible. In fact, as reported in [43], each pair of adjacent pentagons causes an increase in the energy of the system. While this holds true for most cases, sometimes other isomers, maybe in the form of non-classical fullerenes, may be preferred in terms of thermal stability.

In this work the chosen fullerene is  $C_{28}$ , which is typically regarded to be the smallest stable fullerene [44]. While, in fact, smaller fullerenes, like  $C_{20}$ ,  $C_{24}$  and  $C_{26}$ , exist, they are usually not considered stable.

In particular, the studies on the smallest fullerene to be possibly obtained (assuming that a fullerene can only be called as such if it is made just of pentagons and hexagons), that is the  $C_{20}$  one, while being in disagreement on which of its form may be the most stable one, agree in not considering the cage-like structure to be more stable than the bowl one, thus making that configuration harder to be grown technologically. Once obtained, though, as reported in [45], it is not expected to collapse to other forms. Nevertheless, due to the technological complexity of directly obtaining the cage structure, described in [46], it is not considered for the creation of a possibly cheap sensor.

Similar is the reasoning behind  $C_{24}$ , where the two isomers, fullerene and dodecahydrocoronene, are seen as being isoenergetic, but with a predominance of the latter, as reported in [44].

As far the  $C_{26}$  structure is concerned, various isomers have been analyzed and studied in [47], concluding that a non-classical fullerene isomer is thermodynamically more favorable with respect to the classical fullerene shape.

Moving to the  $C_{28}$ , as it happens for the previously cited molecules, as well as for bigger ones, multiple isomers exist, both in the form of fullerene cage, ring and bowl. In this case, the cage is considered to be the most stable one [44], [48]. In particular, the two most common configurations are the ones with  $T_d$  and  $D_2$

symmetry, shown in figures 5.1 and 5.2.

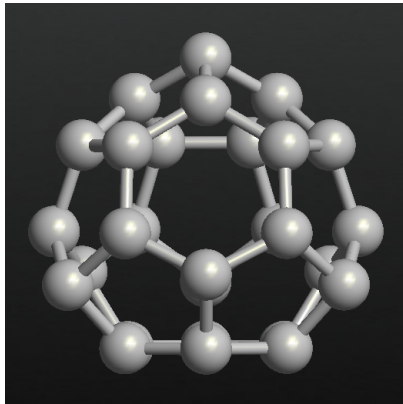


**Figure 5.1:**  $T_d$  symmetry

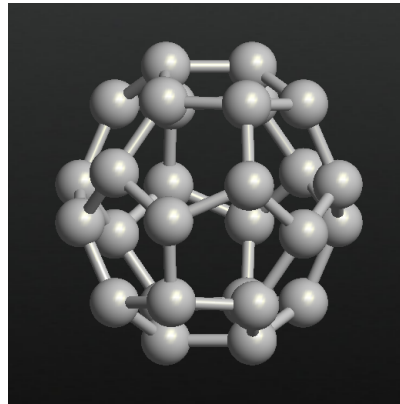


**Figure 5.2:**  $D_2$  symmetry

The differences in the properties of the two are related to the way pentagons and hexagons are connected in the structure. More in details,  $C_{28}$  with  $D_2$  symmetry presents two hexagons connected together, differently from the  $T_d$  configuration, in which all the hexagons are separated by pentagons. As a consequence of the PAPR, and as theoretically demonstrated in [44] and [48], the  $T_d$  symmetry is the isomer with smaller total energy of the  $C_{28}$  fullerene. Nevertheless, since both the configurations have been obtained experimentally with high stability [49] and with the theoretical mechanisms described in [50], [51] and [52], they are both assumed to be possible candidates for the creation of the sensor in the following steps.

The reasons for which this particular fullerene is taken into account are manifold. First of all, studies in literature are lacking, as most of fullerene based structures focus on the  $C_{60}$ . Furthermore, it is characterized by being highly reactive, due to the high curvature and to the presence of four unpaired electrons at the most strained pentagonal triplet vertices [49] [53]. This means that it can be a great candidate for the realization of a sensor, allowing for high sensitivity in interacting with other species. Finally, considering it is an unsaturated molecule it may be possible to obtain strong bonding configurations with metal contacts, thus permitting to have a sensor able not to lose its good properties due to usage.

## 5.2 Introduction on configuration analysis

Having chosen the molecule for the channel, it is now time to find what is the best geometry for the whole system. Before doing so, in this section some important preliminary information are given to understand how the successive steps have been performed.

As mentioned in section 1.3.3, a huge problem for the realization of molecular electronics is the variability. In fact, even small variations in the way the molecule is connected to the contacts, both in terms of rotation but also of distance, can cause great variations in the behavior of the device. This is still the main reason for which this kind of structures have not been implemented yet in a widespread way. Nevertheless, the material for the contacts is a parameter which is not affected by process variations and can thus be fixed without approximations. In this step, in particular, a (1,1,1) face-centered cubic (FCC) gold structure is considered to constitute the contacts. The reasons for this particular choice will be analyzed in the following.

Once the material for the contacts is fixed, it is important to study which are the most likely to occur configurations for the structure. In particular, the distance between the molecule and the contacts is a crucial parameter as it also gives an indication of how wide the nanogap should be. Again, this is one of the most complex step in the practical realization of the system as it is hard to consistently get the desired distance. In this step it is also fundamental to find what the preferred orientation of the molecule is with respect to the contacts.

All of the mentioned parameters greatly impact the final characteristics of the sensor, since the transmission spectrum and hence the current are directly related to the coupling coefficients, which are ultimately linked to the choice of the materials and the way the various connections occur.

It is important to notice that here no process variations are considered. This means that various possible configurations are analyzed, both from the extension of the gap and of the orientation point of view, but it is always assumed that the resulting structure can be obtained technologically.

As far as fullerene  $C_{28}$  is concerned, studies in literature are quite lacking, with only few focusing on pristine  $C_{28}$ . Attempts towards the realization of a device using this fullerene are present in [54], where  $D_2$  symmetry is considered in three structures, with contacts made of gold, copper and silver but without references in terms of precise distances, and in [55], where again three structures, this time with  $T_d$  symmetry, are studied. Other studies, like [56], [57], [58], focus on more complex structures, known as endohedral fullerenes, where additional species are inserted inside the cage to improve the mechanical stability or to modify the transport properties of the system. For this reason, the geometries therein reported are not considered to be representative of the way pristine  $C_{28}$  fullerene creates bonding with other materials. In the following, the structures reported in [54] and [55] will be studied to verify their validity, as well as others not found in literature.

Before proceeding, it is necessary to describe how the correct configurations can be found. Unfortunately, in *ATK* there is not a tool devoted for the dynamic analysis of how the fullerene can connect to the contacts, starting from the environment to then enter in the nanogap.

Therefore, what is done in this chapter is to directly place the molecule in the channel, with a precise orientation and distance, and then relax the structure as to see how the system prefers to place the fullerene. If, at the end of the process, the amount of deformation from the initial configuration of either the contacts or molecule is too extended, the starting position is not considered to be a possible way in which C<sub>28</sub> links to gold. If, otherwise, a certain degree of deformation is present, but not too much as to suggest an initial wrong alignment, the configuration is considered to be a possible one.

Concerning the device calculator block, the employed settings are reported in table 5.1. The geometry optimization settings are instead reported in table 5.2.

**Table 5.1:** Device calculator settings. If not specified, default settings have been used.

	<b>SemiEmpiricalCalculator</b>
<b>Hamiltonian</b>	Parametrization: Slater-Koster Parameter Group: DFTB Parameter Set: DFTB (dftb.org, auorg-1-1) No SCF iteration: unticked
<b>Numerical Accuracy</b>	Density mesh cut-off: 10 Hartree Interaction max range: 10 Å Occupation method: Fermi-Dirac Broadening: 300 K k-points: [4, 4, 4] Å

**Table 5.2:** Geometry optimization settings. If not specified, default settings have been used.

	<b>Geometry Optimization</b>
<b>Parameters</b>	Max forces: 0.05 eV/Å Max stress: 0.1 GPa Max steps: 300 Max step length: 0.2 Å

As far as the constraints for the systems in the geometry optimization block are concerned, the first few layers of gold have been allowed to relax freely in all three directions, whereas the others were fixed (a meaningful picture about constraints can be found in appendix A).

Notice that in this chapter only some of the analyzed configurations are reported. For a more complete list of structures and distances refer to appendix A.

## Physisorption and Chemisorption

Before proceeding with the analysis of the various configurations, it is necessary to review the possible ways a molecule and a metal structure can interact. In fact, when an atom or a molecule interacts with a solid surface, a process of adsorption occurs. This phenomenon can be divided in two categories, known as physisorption and chemisorption. As the names suggest, the difference between these two is that physisorption is a physical bonding mechanism involving attractive dispersion forces and short range repulsive forces, as well as specific molecular interactions like polarization, field-dipole and field gradient quadrupole, occurring as a result of particular geometric and electronic properties of the adsorbent (the material on which the gas is adsorbed) and adsorptive (the material which is being adsorbed) [59]. In the case of chemisorption, instead, a chemical bonding is physically present. Therefore, while physisorption is mainly associated to the electrostatic interaction between the two species involved, and it is thus quite weak, chemisorption has a chemical nature, hence resulting in a much stronger interaction. As a consequence, while in the first case the two structures remain unchanged, in the second case a great modification of the electronic structure occurs. Physisorption can be associated to the well known Van Der Waals force, which is exerted between any two molecules, making physical adsorption possible on any solid surface [60] [61]. Chemisorption, instead, presents a covalent bond and, as such, involves the transfer, exchange, or sharing of electrons between the two species, and is therefore slower and energy activated [60]. Nevertheless, it is important to highlight that the two phenomena are not really unrelated. A typical situation, in fact, sees a first moment of physisorption followed then by the creation of the bonding itself (an interesting case is the one of dissociative chemisorption). Another important consideration to be done is that there is a configuration which minimizes the potential energy of the system, in both the bonding situations. Indeed, if one analyzes the energy-distance curve for a specific process, a minimum of energy is observed at a specific distance, which obviously depends on the interacting species, especially in the chemisorption case. This distance is the one searched in this chapter, as it is possible to associate to it the structure minimizing the energy of the system, and therefore the most likely to happen. Consequently, studying these two types of interactions will be very important in the following. Furthermore, not only they are involved in the bonding of the fullerene with the contacts, which is the content of this chapter, but they are also crucial in the sensing mechanism, required for the final sensor to work.

Notice, in that regard, that the choice of gold is directly related to the necessity

of having a good bonding. Gold is the typical material of choice in dealing with molecule-based electronics. In fact, it has been demonstrated in [62] and [58] to create strong covalent bond with carbon and has been widely used to create structures like the ones reported in [63]. Therefore it is a good choice for the fullerene under analysis.

As far as the configurations of this chapter are concerned, in *ATK* it is not straightforward to verify the presence of a bonding and in particular the type of bonding present. These information can be derived by means of specific studies, like the molecular projected self-consistent Hamiltonian (MPSH), Mulliken population analysis or with specific adsorption studies. Therefore, only in certain cases such analysis are carried on, keeping in mind that studies of adsorption of fullerenes on gold exist and have proved the presence of strong interactions.

Of course, it is also intuitive to verify the presence of an interaction by directly performing DOS, transmission spectrum (TS) and current analysis, since, as demonstrated within the NEGF framework of the previous chapter, the amount of coupling has a great impact in broadening of energetic levels and hence on these figures of merit. However, the previously cited analysis may provide a better insight on the type and amount of interaction.

### 5.3 D<sub>2</sub> symmetry configurations

Starting from the D<sub>2</sub> symmetry of the fullerene, in this section two possibilities are analyzed.

First, in part 5.3.1, some configurations where the fullerene is not expected to create a strong bonding with the contacts due to the chosen distance are considered. In these cases the interaction may be of weak chemisorption type or strong physisorption. Since the distances are quite bigger with respect to those employed in literature, in order to prove the effective presence of a link between the contacts and the fullerene, a study is performed about the molecular projected self-consistent Hamiltonian (MPSH), which allows to study the delocalization of the system orbitals over the whole system.

Then, in section 5.3.2, other configurations where instead the distance is shorter and hence the bonding stronger are considered.

Notice that the configurations reported here are as close as possible to being symmetric. Indeed, this is not a nitpicking choice. Other configurations, with an asymmetric shape, were considered. However, what usually happens in these cases is that the interaction with the left contact is different with respect to the interaction with the right contact, causing the relaxed geometry to have the fullerene really close to one contact and far away from the other one, thus excluding those geometries from being equilibrium ones.

### 5.3.1 Weak coupling configurations

Since no specific configurations have been found in literature regarding distances in the order of 3 Å or higher, for the first structure the fullerene has been placed unrotated (i.e. with the orientation naturally provided by *ATK*) at a distance of 3.36 Å from the nearest gold atom. The resulting structure is reported in figure 5.3. Using both force field and Slater-Koster, the fullerene does not seem to be greatly modified. On the other hand a little deformation on the contacts occurred, suggesting a different distance between gold and molecule (see figure 5.4).

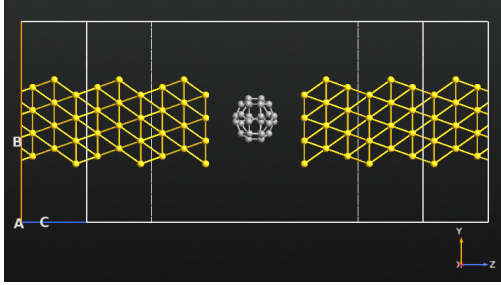


**Figure 5.3:** Initial configuration for the fullerene placed at 3.36 Å from the nearest gold atom.

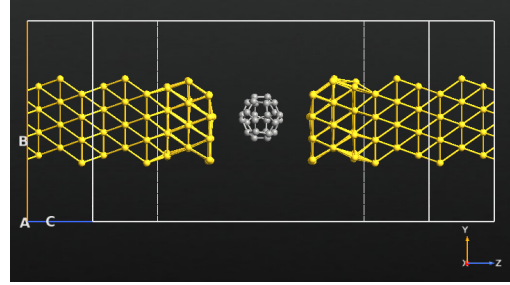


**Figure 5.4:** Configuration of the device after relaxation has occurred. Notice the displacement of gold atoms especially in the right contact.

While other distances have been analyzed keeping the orientation of the fullerene constant, none of them proved to be more favorable than the one initially considered. A couple of these alternative configurations are reported in appendix A (in one the distance is 0.1 Å higher, to see if the deformations of the contacts were less extended; in the other it is 0.1 Å smaller, to see if the deformation pushes the fullerene to create strong covalent bonding with the contacts). Other attempts have also been made with the distance kept constant but with different orientations. In these cases, stronger deformation occurred.

### Molecular projected self-consistent Hamiltonian

As previously anticipated, the presence of an effective bonding may be verified by means of an MPSH analysis. Indeed, from figure 5.3, it is unclear whether the fullerene and the contacts are effectively interacting.

The idea is to project in the real space the eigenstates associated to the Hamiltonian of the system. As shown in the previous chapters, the Hamiltonian of the system is the operator associated to the total energy of the system itself. Using it in association with Schrödinger equation allows one to get the eigenvalues of the system,

i.e. the energy values that can be achieved by the system itself. In conjunction to the eigenvalues, eigenfunctions are obtained, which are the eigenstates associated to the system, i.e. the molecular orbitals. Projecting these onto the system in the real space means to see the 3D surfaces of iso-energy. So why is this analysis so useful? It is a common methodology, as shown in [64] [65] [66], to employ MPSH to verify how the system behaves.

When the molecule interacts with the metal, its orbitals get modified. If a contact is effectively present, some orbitals are involved in transmission. As a consequence, the MPSH analysis will show a delocalization of such system orbitals on the whole scattering region. In this case, the motion of particles from one side of the device toward the other is possible and therefore an interaction is occurring (particles have no problem in traveling in regions of space in which their energy is constant). If, otherwise, the orbitals are localized either on the contacts or on the molecule, the motion is not favored and therefore a weak or no bonding is present and a small current may flow thanks to tunneling effects.

Within the *ATK* environment, MPSH energies are easily computed by exploiting the *MolecularEnergySpectrum* block, allowing to find the HOSO (highest occupied system orbital) and LUSO (lowest unoccupied system orbital) levels, whereas the *EigenState* block evaluates the eigenstates. Using these tools, an analysis on the considered configuration has been performed. The results are reported in figure 5.7. In figure 5.5, the molecular orbital related to first level in the HOSO side is analyzed. As shown in the figure, a great degree of delocalization occurs all over the system. The same behavior is observed in the LUSO level, reported in figure 5.6.

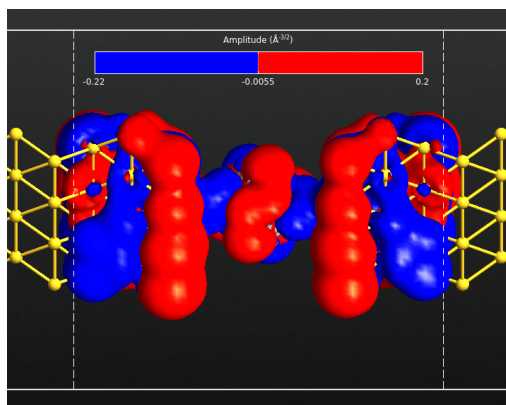


**Figure 5.5:** MPSH relative to the highest occupied system orbital.

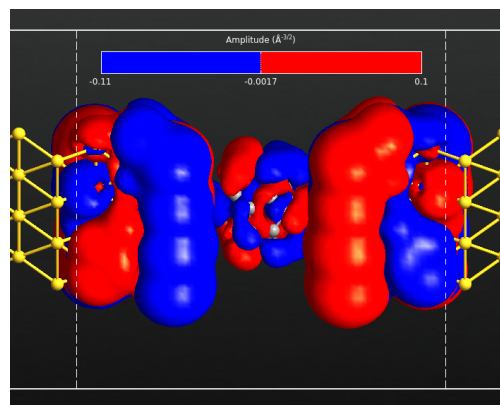


**Figure 5.6:** MPSH relative to the lowest unoccupied system orbital.

**Figure 5.7:** MPSH analysis of the structure (zoom on the middle region)

Given these results, it is clear that a good interaction between the molecule and the contacts is occurring, although the evaluation on the quality of the bonding would require a more in depth adsorption study. In light of what has been discussed thus far, this is considered to be a stable possible configuration for  $C_{28}$  with  $D_2$  symmetry.

### 5.3.2 Strong coupling configurations

Since no other configurations of weak coupling proved to be better than the one reported, structures with shorter distances between the contacts and the fullerene have been taken into account. One may ask why to look for other structures when a good one has already been found. The reason is quite simple. While in the weak coupling case (possibly related to a physisorption bonding) a contact is present and a current flows through, nevertheless it is more subject to lose its properties over time or by means of interaction with other species. In fact, as previously said, physisorption is not a strong bonding and can be broken quite easily, possibly causing the removal of the fullerene from the channel. Therefore, if a configuration with a covalent bonding exists and is proven to be stable, it would be more probable to occur (remind that chemisorption typically follow physisorption), and it would be a better configuration for the creation of a sensor as a great increase of the current, and thus of the sensitivity, as well as integration with standard technologies, would occur.

With this idea in mind, following the design of [54], the  $C_{28}$  fullerene has been placed between the electrodes at a distance of 2.31 Å, compatible to the configuration of [57] and [58], as well as the experimentally verified Au-C bond measured in [62]. The resulting structure is reported in appendix A.

Using then the geometry optimization tool, the structure has been allowed to relax toward a more stable configuration, firstly with a simple force field based approach and then with the more complete semi-empirical Slater-Koster analysis. Unfortunately, both of them provided results inconsistent with the result of [54]. In fact, while the size, shape and orientation of the fullerene did not change to a great extent, the contacts resulted extremely distorted. It is therefore not supposed to be a stable configuration. Notice that, with respect to the structures of [54], the fullerene has been initially placed with a certain degree of rotation. The reason for which that is the case is that the optimization tool suggested, through previous analysis with unrotated  $C_{28}$ , that the preferred orientation is indeed the one used in figure A.9.

Supposing that the strong deformation occurred due to a not correct orientation of the fullerene, another configuration was considered, with an Au-C distance of 2.20 Å. The resulting structure is reported in figure 5.8.

Also in this case, after the geometry relaxation, a strong deformation of the contacts,

and especially of the Au-C distance, occurred. In particular, the final distance is of 2.50 Å. Notice that in both cases (A.9 and 5.8) the optimization calculation was stopped after some days as the biggest deformations, if present, usually occurs in the first steps. After that, small deformations still occur but it would have been useless to wait for the tool to produce the final configuration.

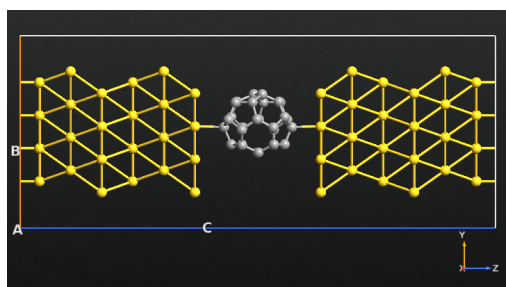


**Figure 5.8:** Initial configuration with rotated fullerene at 2.20 Å.

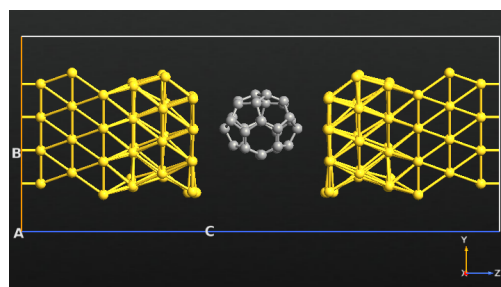


**Figure 5.9:** Final configuration after geometry relaxation.

While other structures, with various orientations, were considered, all of them were characterized by the same behavior: the initial structure gets deformed with an Au-C distance that increases until the force acting on the atoms is smaller than the tolerance.

As suggested by [55], the strong reactivity of  $C_{28}$  may be the cause of this effect. The idea is therefore to place an adatom (i.e. an additional atom on the gold contacts surface) to help reducing the strong interaction between the molecule and the gold surface, hopefully obtaining a stable system.

With the same orientation of the fullerene of the previous configuration, but with the presence of a gold adatom on the surface of gold, the structure of figure 5.10 has been realized.

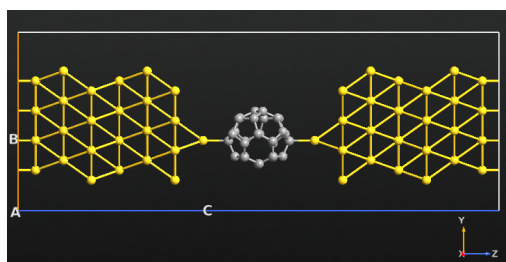


**Figure 5.10:** Initial configuration for the structure with the adatom present.

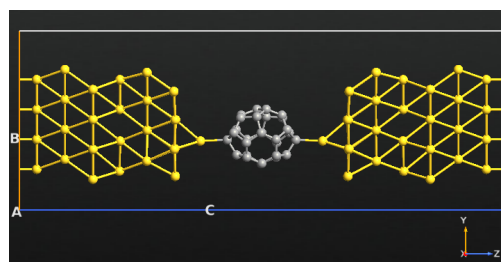


**Figure 5.11:** Relaxed structure. Notice the elongation of the fullerene.

The distance between the adatom and the carbon atom is 2.15 Å, whereas the adatom is placed as a direct continuation of the gold structure, at a distance of 2.88 Å. After geometry relaxation, the new structure has an adatom-carbon distance of 2.29 Å and the adatom is now at 2.7 Å from the nearest gold atom. While a little deformation is present, as shown in figure 5.11, both in the contacts, and in the fullerene, where the biggest amount of deformation is along the z-axis (from 5.14 Å to 5.74 Å of extension), this can be a valid configuration. Indeed, it would be unreasonable that no deformation occurred. From this configuration it seems true that the presence of an adatom is necessary to avoid issues.

## 5.4 $T_d$ symmetry configurations

Moving to the  $T_d$  symmetry, only strong coupling cases are here reported. In fact, no configuration with high distance between the fullerene and the contacts proved to be stable enough for it to be considered a possible structure. However, as done with the  $D_2$  symmetry, the first configuration analyzed does not involve the presence of an adatom.

The initial configuration, reported in figure 5.12, is characterized by a distance of 2.30 Å between the gold atom in the contact surface and the carbon atom. Using again the geometry and calculator settings of tables 5.1 and 5.2, the structure has been allowed to relax. As it happened in previous calculations in the absence of an adatom, the resulting geometry after relaxation suggests this not to be a stable configuration.

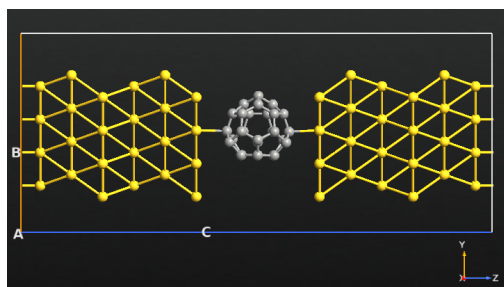


**Figure 5.12:** Initial configuration with the fullerene at 2.30 Å from gold.

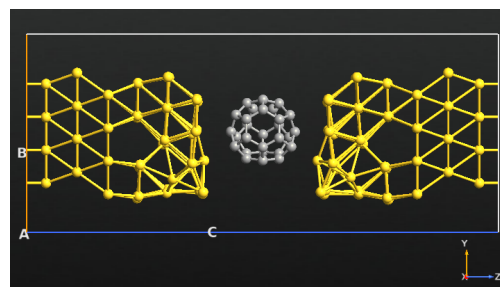


**Figure 5.13:** Final configuration after relaxation. Strong deformation of the contacts occurred.

Having confirmed that the presence of an adatom is required to keep the deformation low, new structures with its presence have been analyzed. In particular, following the designs of [55], three configurations have been realized. Unfortunately, since no meaningful graphical representation is reported in the paper, for each of

the three proposed structures, a couple of attempts with different geometries have been analyzed (notice that the position of the adatom is not always of 2.88 Å, refer to appendix A for more information). As far as the *MJ1* structure of [55] is concerned, one of the two inspired configurations is reported in figure 5.14, whereas the other in appendix A.

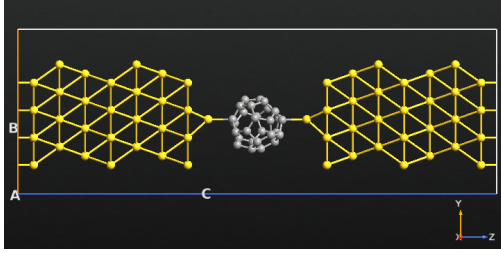


**Figure 5.14:** *MJ1* junction initial configuration. The Au-C distance is 2.25 Å.

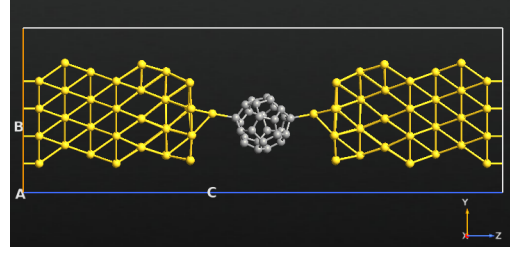


**Figure 5.15:** Structure resulting from optimization.

In this case, since the structure is not symmetric, a good amount of deformation is observed on the fullerene, which results to be more spherically shaped after relaxation (the deformation along the z-axis is in the order of 10%). Nevertheless, since both of the configurations have the same characteristic after relaxation, this may suggest that the fullerene is prone to deform along that direction, and that therefore does not directly go with that orientation within the channel.

Analyzing now the *MJ2* structure, also in this case two structures have been realized. The first one is reported in appendix A. The second structure is instead reported in figure 5.16.

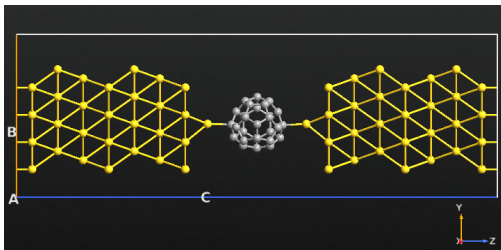


**Figure 5.16:** *MJ2* junction initial configuration.

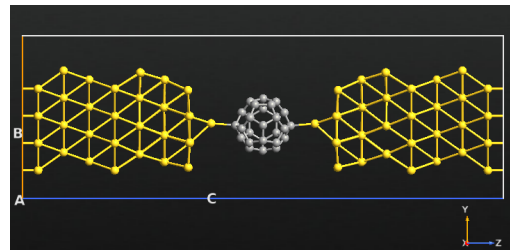


**Figure 5.17:** Final configuration after relaxation.

The initial distance is set at 2.21 Å. After relaxation, the structure is just slightly

modified. Since the amount of deformation is small, this can be a valuable configuration for the  $T_d$  symmetry.

Different is the case for the *MJ3* configuration, of which a similar structure with respect to the one of the paper is reported in figure appendix A. After geometry relaxation the structure gets considerably modified, both in the contacts and in the position of the fullerene. It is hence not assumed to be a stable configuration.

## 5.5 Chosen structure

In this chapter a lot of configurations have been taken into account. While some of them proved not to be stable, others instead seem to be good candidate for the creation of a sensor. In particular, for the  $D_2$  symmetry, the structures of figure 5.3 and 5.10 proved to be valid. For the  $T_d$  structure, instead, the most stable one is the system of figure 5.16.

To proceed in the following steps a configuration must be chosen. Even though, in section 5.1, it has been said that the two symmetries can be both obtained experimentally, since it is necessary to do a choice between the various structure, the geometry of figure 5.16, with the more stable  $T_d$  symmetry, is fixed and used in the next analysis (a study of the MPSH on that structure has been performed and the results reported in appendix A). Indeed, it is reasonable to think that, due to the smaller stability of the  $D_2$  symmetry, systems realized with it would be more prone to lose their properties in time, and that the structure of the fullerene may break due to the interaction with other elements.

Furthermore, since the amount of deformation of the system in the decided structure is very small, in order to reduce the computational effort in the calculations of the successive steps, due to the presence of additional slightly deformed layers in the contacts, it has been decided to proceed the analysis on the initial geometry and not on the relaxed one. Of course, rigorously, the configuration to be used should be the closest possible to the effective real one, and therefore the optimized structure should be the one employed. Nevertheless, it is also assumed that, if the molecule works well as a sensor sensitive to specific species in the undeformed configuration, a similar effect is expected to happen also in the deformed case.

There is also a more subtle reason, that will be clearer in the next chapter. It will be shown, in fact, that the Slater-Koster method does not allow for the analysis of all the possible species which may interact with the system. As a consequence, since it is recommended that the analysis should be performed with the same tool exploited for the geometry optimization, it has been chosen to avoid using a structure configuration evaluated by Slater-Koster and then studied with another tool. Again, this is reasonable also, and especially, for the aforementioned reason, that is the small degree of deformation resulting from relaxation.

# Chapter 6

## Free air performance

Fixed the geometry for the system, it is now time to analyze the behavior of the final structure. However, since no information about a possible sensor exploiting the chosen molecule have been found in literature, the purpose of this chapter is manifold.

First of all, in section 6.1 the device is studied with different tools in an equilibrium condition and in the absence of other particles, in order to have a starting comparison in performance between less computationally involving methods, like EHT and Slater-Koster, and more complete and expensive ones, like DFT.

Then, a similar comparison is performed in section 6.2 in the presence of additional species naturally found in the atmosphere. These analysis have the purpose of checking whether the system is able to modify its properties when interacting with various species as well as to verify the quality of the methods employed, to see if they are all able to identify such variations. Of course it is reasonable not to have very close outputs, due to the higher degree of approximations introduced, but because of the huge number of atoms present in the structure, DFT analysis could not be performed out of equilibrium and so, if the methods are somewhat comparable, successive studies will be performed with less demanding tools.

Finally, in section 6.3, out of equilibrium analysis using EHT with atmospheric compounds are presented, to confirm the modification in properties of the system in interacting with other species also in the case of a voltage being applied between the electrodes.

As far as the settings for the simulations are concerned, for Slater-Koster the settings are equal to the ones of table 5.1, with the only difference being the *k-points density*, increased to [4, 4, 150]. The reason for which that is the case can be found on the *Quantum ATK* forum, where, for device calculations like the ones of transmission, density of states and current analysis, it is suggested to use a big number of k-points in the transport direction to match the electronic structure of the electrodes [67].

**Table 6.1:** EHT settings. If not specified, default settings have been used.

	<b>SemiEmpiricalCalculator</b>
<b>Hamiltonian</b>	Parametrization: Extended-Hückel Theory Parameters: Hoffmann Weighting: Wolfsberg Spin: unpolarized No SCF iteration: unticked
<b>Numerical Accuracy</b>	Density mesh cut-off: 10 Hartree Interaction max range: 10 Å Occupation method: Fermi-Dirac Broadening: 300 K k-points: [4, 4, 150] Å
<b>Poisson Solver</b>	Solver Type: [Parallel] Conjugate Gradient Boundary Conditions: A: Periodic; B: Dirichlet; C: Dirichlet;

**Table 6.2:** DFT settings. If not specified, default settings have been used.

	<b>LCAO calculator</b>
<b>Basis set</b>	Exchange correlation: GGA Functional: PBE van der Waals correction: Grimme DFT-D2 Pseudopotential: FHI Basis set: DZP
<b>Numerical Accuracy</b>	Density mesh cut-off: 75 Hartree Occupation method: Fermi-Dirac Broadening: 1000 K k-points: [4, 4, 150] Å
<b>Poisson Solver</b>	Solver Type: [Parallel] Conjugate Gradient Boundary Conditions: A: Periodic; B: Dirichlet; C: Dirichlet;

For the EHT and DFT settings, the employed ones are reported in tables 6.1 and 6.2. For the transmission spectrum and the density of states blocks at equilibrium, instead, the range of energies analyzed is comprised between  $-3$  eV and  $3$  eV with 301 points. The rest of settings have been kept unchanged.

## 6.1 Clean sensor

Starting with the analysis of the system in the absence of additional species, in figures 6.1 and 6.2 the density of states per unit energy and the transmission spectrum are plotted. Of course, these two elements are crucial in the examination of a device. The DOS allows, in fact, to study the number and the energetic position of states which are allowed for electrons to be occupied and the TS plays a primary role in the evaluation of the current, giving a fast idea of the amount of charge able to flow through when a voltage is applied and a bias window is created. Therefore, a first analysis of these elements at equilibrium is already capable of giving a first insight of how the structure will behave in the presence of a voltage drop between the electrodes. In fact, if a variation of them occurs with no bias applied, it is reasonable to expect the same effect out of equilibrium.

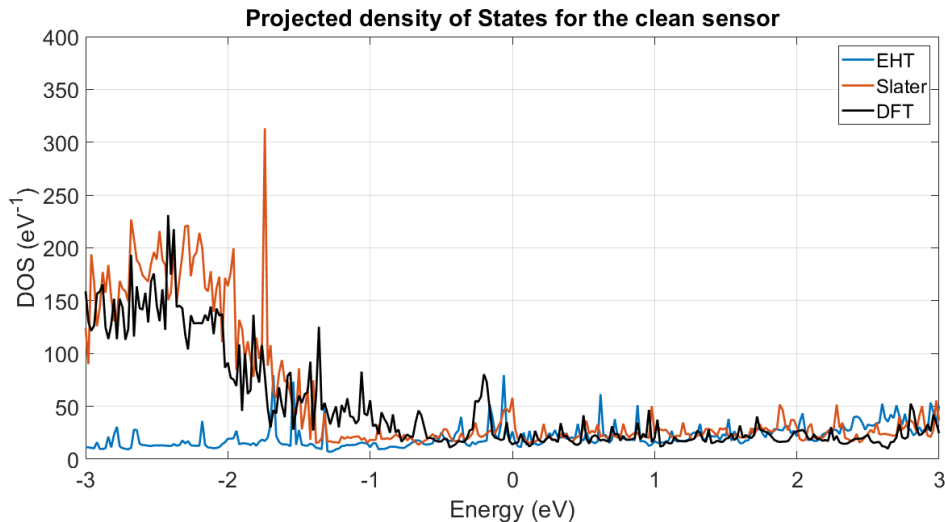


**Figure 6.1:** Comparison between the DOS at equilibrium evaluated by DFT, EHT and Slater-Koster. Notice that the  $0$  eV energy level corresponds to the Fermi level.

Of course, this is not the full picture, and it would be a mistake thinking that there is a one-to-one correspondence between the TS in and out of equilibrium,

since it has been previously verified that the bias changes the shape of the spectrum both in a direct way, by means of which the peaks are rigidly shifted in position, and in an indirect way, with effects like the charging effect. Nevertheless, it would also be wrong to think the opposite, and this preliminary analysis can still be useful, for example, for the comparison between the possible employable tools (DFT, Slater-Koster and EHT in this case).

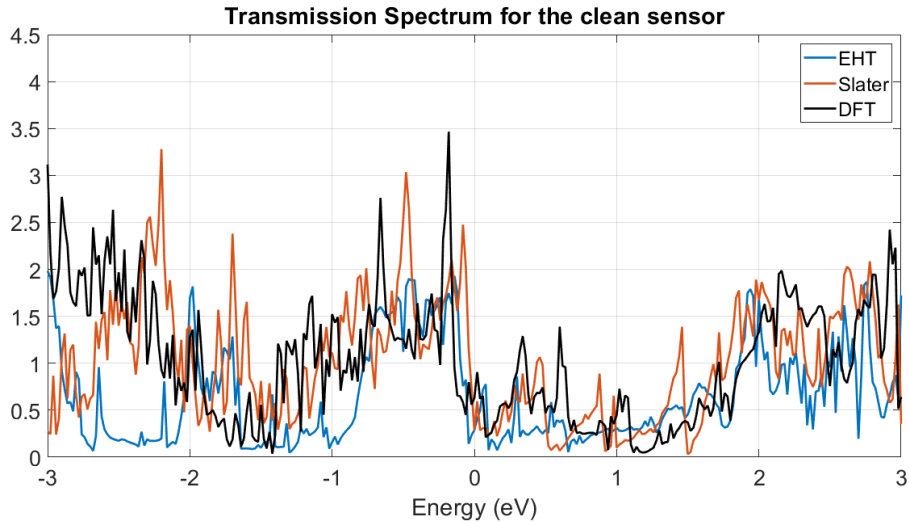


**Figure 6.2:** Comparison between the TS at equilibrium evaluated by DFT, EHT and Slater-Koster.

Focusing on the density of states, it is possible to observe a great agreement between the DFT and the Slater-Koster methods, with most of DFT behavior being replicated by the semi-empirical tool. On the other hand, EHT mostly fails in reproducing this result, with the increasing number of available states below the Fermi level, in particular for energies smaller than  $-1$  eV, not individuated by this model.

Slightly different is the case of the transmission spectrum. While it is true that Slater-Koster is still better, especially in the HOSO side of the spectrum, also EHT seems to be able to catch the properties of the system, and in particular the dip at the beginning of the LUSO side is well reproduced, as well as the overall behavior of the DFT curve. The main difference, as it happened in the DOS analysis, regards an underestimation of transmission, again prevalently in the region between  $-3$  eV and  $-2$  eV. Notice that, due to the presence of transmission peaks near the Fermi level, the system is expected to enter in conduction already at very low biases, potentially allowing to work with reduced power (although this is not expected to be an element of concern considering the application of the sensor and taking

into account the small bias voltages involved) and high sensitivity, especially if the variation of DOS and TS in the presence of additional species involves such energetic spectrum.

## 6.2 Performance at equilibrium

With the idea of analyzing the properties of the system in the presence of other particles, a good starting point is to verify whether the sensor modifies its equilibrium characteristics with typical free air particles common in the atmosphere.

Indeed, since the final sensor is required to feel the presence of different elements in a room, for example, it is expected to do so with also the presence of elements naturally found in any uncontrolled space, and therefore this first analysis may be crucial to verify the reactivity of the employed molecule. If that results to be the case, it will be then possible to proceed further to see if the variations due to the presence of various pollutants can be distinguished with respect to those particles and hence if a sensor can be realized or not.

It is well known that the most present gases in the atmosphere (in dry air case) are, in order of concentration, nitrogen, oxygen, argon and carbon dioxide, followed by other particles like Ne, He, Kr, Xe, H<sub>2</sub>, CH<sub>4</sub> and N<sub>2</sub>O (a list of them with precise concentrations is reported in [68]). In this section the substances taken into account and considered to be possible source of interaction, and that are therefore necessary to be studied in interacting with the sensor, are the ones of the first group. In addition to them, also water vapor is taken into account, to foresee the possibility of having a high degree of humidity (in this case, considering water is a molecule held together by an hydrogen bonding leading to a polar behavior, with the position of the electronic cloud centered around the oxygen atom, different orientations of the molecule were taken into account). The elements of the second group, on the other hand, since being characterized by a low concentration, in the order of few parts per million (ppm), are not considered of interest in the following analysis, as the interaction of the system with them is very unlikely to occur.

Until now the sensor has always been considered clean. This means that the fullerene in the channel was not interacting with other species. Therefore, before proceeding, it is important to describe how the sensing mechanism takes place. In section 5.2, the two main adsorption processes have been introduced to study how the molecule can create bonding with the contacts. Indeed, the same type of interactions are responsible for the sensing phenomenon. In theory, what should be done is an optimization analysis similar to those of chapter 5, to find out what is the best configuration for interaction. Unfortunately, due to the limited computational power of the machine employed, studies of this type could not be performed, and therefore the position of adsorbed species has been enforced in an arbitrary way.

In this section, in particular, it is assumed that the interaction is due to a physisorption mechanism. To be more precise, the distance at which the various molecules were placed has been fixed at about 2.10 Å, in order to obtain a good intersection between the Van Der Waals spheres of the carbon atoms in the fullerene and the ones of the atoms belonging to the considered molecule. A complete list of pictures and distances depicting the employed configurations is reported in appendix B. Notice that, since the Van Der Waals radii of the involved molecules are close, in magnitude, one with respect to the other, the positions at which the atmospheric species have been placed were similar.

The following analysis are still performed at equilibrium, so DFT, EHT and Slater-Koster are all taken into account to finally decide what will be the final tool for the studies out of equilibrium.

### Mulliken population analysis

Even though it has been said that the precise interaction positions could not be found, it is possible to do a simple analysis to find out what are the atoms in the fullerene which are expected to be more reactive to external species. A study of this kind can be performed exploiting a Mulliken population analysis, which provides a fast way to know the distribution of the electronic charge within the system. Although not being listed as a precise tool for knowing the exact amount of atomic charges, due to the high dependency on the basis set chosen to study the system [69] [70], it can however be used to have a rough idea of the distribution of charges and hence to find the sites of the molecule expected to have a higher negative or positive charge distribution. This can be helpful in order to find positions of external molecules where the interaction may be strengthened by a big electric charge distribution unbalance, thus leading to a stronger electrostatic attraction.

Notice also that a validity check of this method has been performed employing different basis set using DFT and Slater-Koster with the fullerene in the absence of the contacts (see appendix B for further details), obtaining results comparable with the ones of [49]. A Mulliken population analysis performed on the full sensor with Slater-Koster provided the result shown in figure 6.3.

Without focusing on the exact variation in the charge distribution between the carbon atoms, it seems that the behavior of the C<sub>28</sub> without electrodes is basically unchanged in interacting with the gold layers, therefore showing the same negatively charged four carbon atoms. This is a further confirmation of the covalent nature of the interaction between gold atoms and carbon atoms, with the electronic cloud being evenly distributed between the two species.

Another thing to notice is that, both in the absence and in the presence of the contacts, the uneven charge distribution is not too extended, with only a portion of the full electron charge being concentrated near those atoms.

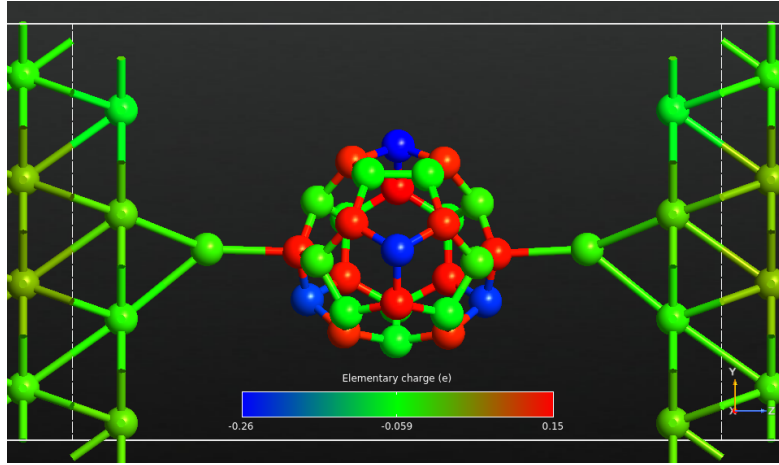


**Figure 6.3:** Mulliken population of the sensor (zoom in the middle region) as evaluated by Slater-Koster. Notice the four carbon atoms slightly negatively charged.

Nevertheless, with the purpose of maximizing the interaction strength due to the physisorption interaction, which depends on a temporarily fluctuating dipole moment arising from a brief shift of orbital electrons to one side of an atom or molecule, which creates a similar shift in adjacent atoms or molecules [71], in the following all the external species will be placed in a region of space ensuring the interaction with a negatively charged carbon atom. To be more precise, the enforced position is near the pentagon on the top of the structure, in such a way that the temporary induced dipole of the external species has the positive tail near the negatively charged carbon atom.

### 6.2.1 DFT results

Starting with the DFT results, in figures 6.4 and 6.5, the DOS and the TS are considered.

As shown, in both cases the presence of external species nearby the channel causes a good variation in the properties of the system. In particular, focusing on the DOS, the main variations occur near the Fermi level, and more precisely in the HOSO side. This effect is accentuated at about  $-0.2$  eV,  $-1.1$  eV and  $-1.6$  eV, with a significant increase in the available states. While a certain degree of variation is also present in the LUSO side, such modifications are far less extended with respect to those just mentioned.

More interesting is, instead, the analysis of the TS. Here, the HOSO side is still the one more involved by the presence of other species, with a modification which

seems to be different for each molecule introduced.

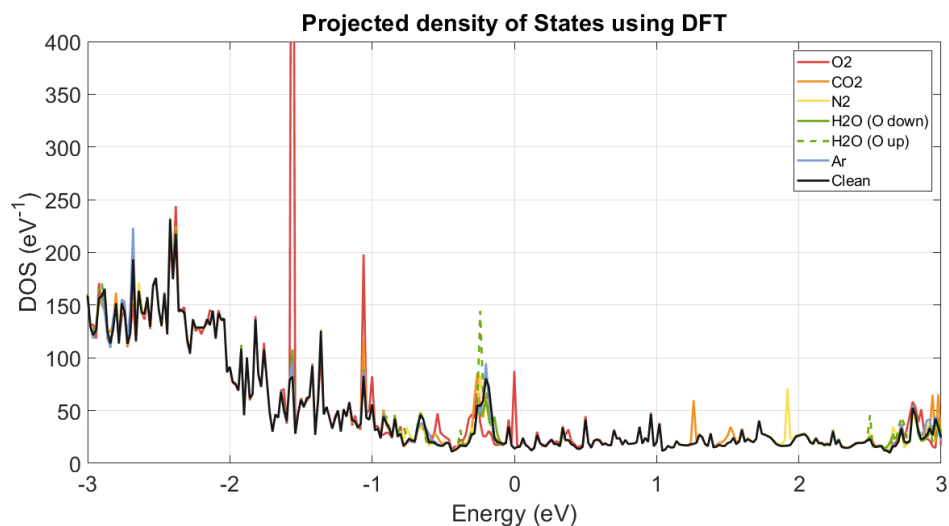


**Figure 6.4:** Density of states as evaluated by DFT in the presence of free air species. Notice that the peak at  $-1.6$  eV is cut to keep the image comparable to the following ones and to allow a better visualization of the DOS. A complete image can be found in appendix B.

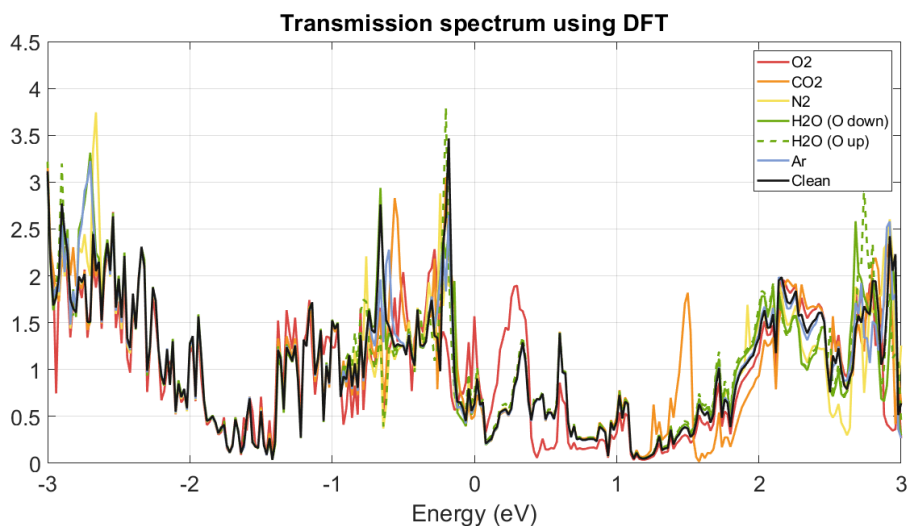


**Figure 6.5:** Transmission spectrum as evaluated by DFT in the presence of free air species.

Nevertheless, this time also the LUSO side is affected, and in particular, for small energies,  $O_2$  and  $CO_2$  cause a good variation in the position and extension of the peaks in transmission.

## 6.2.2 Slater-Koster results

Moving to the results obtained by the Slater-Koster semi-empirical method, as happened before in the clean sensor case, both the DOS and the TS are quite close to the ones of DFT.

In figure 6.6 the DOS is reported. While the overall shape is similar to the previous one, a smaller variation is observed. The peaks at  $-1.1$  eV and  $-1.6$  eV are not well reproduced whereas a bigger modification occurs at the Fermi level.

Different is the case of the transmission spectrum, shown in figure 6.7. The variation due to the presence of  $O_2$  is present and the main variations are occurring at the Fermi level, as in the DFT case.

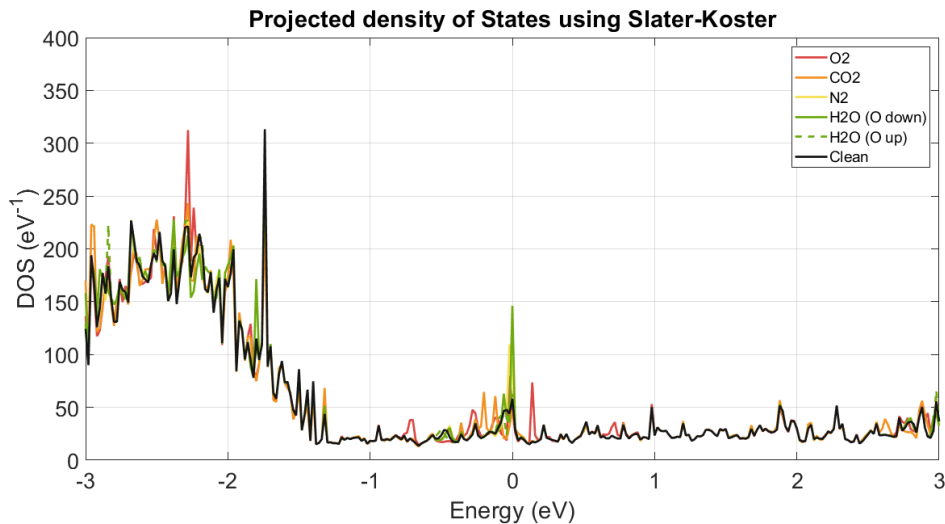


**Figure 6.6:** Density of states as evaluated by Slater-Koster in the presence of free air species.

Unfortunately, these analysis also highlight the issue of employing Slater-Koster for this and the next analysis. It is clear from the DOS and TS graphs that the study of the variation induced by argon is missing. The reason for which this is the case has to be addressed to the lack of a basis set for such species, not only in the *ATK* suite, but also in literature. This means that it is not possible to carry out any study on it and that therefore the tool can not be taken into account for successive analysis. Indeed, this is not just a problem for free air interaction of

the system, but it can arise again for other species belonging to pollutants, thus causing the final results to be incomplete. Therefore, while it has been proven that the results pulled out by Slater-Koster are very close to the DFT ones, it will not be considered anymore to be a valid option.

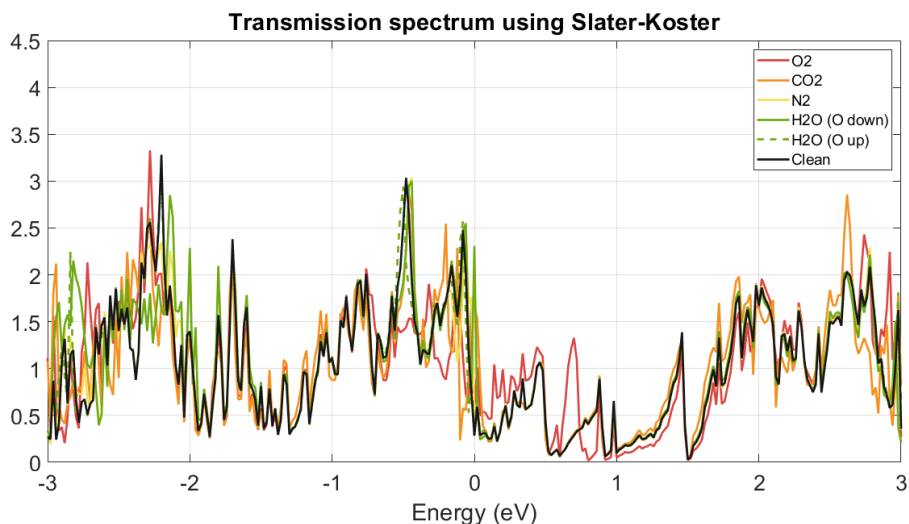


**Figure 6.7:** Transmission spectrum as evaluated by Slater-Koster in the presence of free air species.

Notice that this reasoning is at the base of the choice of using the non-relaxed geometry in the previous chapter. In fact, as mentioned, the successive analysis would have had to be performed with the same optimization tool, which, as just said, could not be employed for the characterization of the sensor.

### 6.2.3 EHT results

The same analysis just performed on the TS and the DOS have been also carried out for the EHT model. The results are reported in figures 6.8 and 6.9.

As in the clean sensor case, EHT is not able to reproduce in a significant way the DOS evaluated by DFT, especially in the HOSO side. Nevertheless, as both DFT and Slater-Koster did, it is able to predict a variation in the number of available states per unit energy caused by interaction with free air particles and a similar variation with respect to the other two methods in the neighborhood of the Fermi level is observed.

Same observations hold true for the TS, even though the interaction with argon seems to be more effective. Notice, in that regard, that a basis set for representing argon is present and has been therefore possible to have a complete analysis.

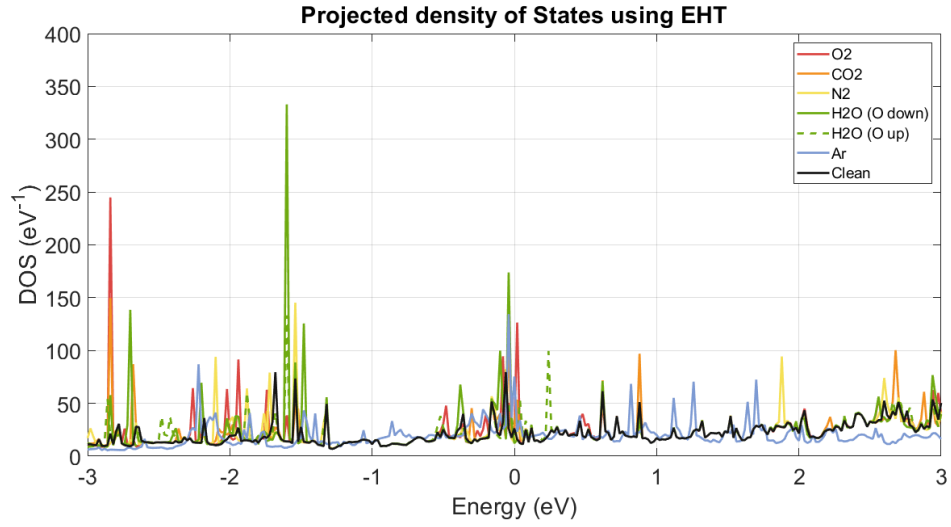


**Figure 6.8:** Density of states as evaluated by EHT in the presence of free air species.

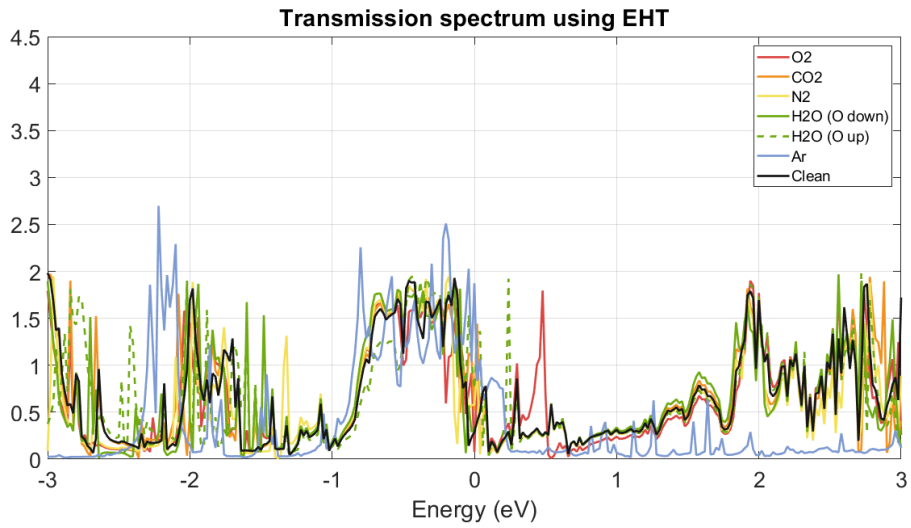


**Figure 6.9:** Transmission spectrum as evaluated by EHT in the presence of free air species.

In order to have a further validation of the semi-empirical methods, a final study has been performed. Considering that, in the NEGF theory, under the hypothesis of coherent transport, the current is evaluated by means of 4.29, a preliminary

evaluation of the integral of the transmission spectrum may confirm the quality of EHT. Of course, this analysis is not rigorous at all, since the transmission spectrum is strictly dependent on the applied voltage, but, if such integrals provide very different results, it is reasonable to assume the same to happen in the successive studies.

Taking into account the possibility of having applied voltages from 0.04 V to 6 V with a 0.04 V step between them, the integrals of the TS on the range of energies related to the bias window created by such voltages were evaluated and the average percentage difference between the results of DFT and the ones of EHT and Slater-Koster, calculated. To be more precise, for each applied voltage the percentage difference, considering that the integrals run from  $E_1$  to  $E_2$ , which represent the initial and final energies included in the bias window for that specific voltage, has been evaluated by means of:

$$\frac{|\int T_{DFT}(E)dE - \int T_{EHT}(E)dE|}{\int T_{DFT}(E)dE} \cdot 100$$

Performing this calculation for all the desired voltages, the average percentage variation has been derived by averaging the results over the total number of voltages applied.

In appendix B, the graph related to the integrals as well as a table with the results obtained are reported. As shown, the variations are quite high. Nevertheless, considering that the modification of the TS due to the applied voltage is expected to increase with increasing bias, and observing the graph just obtained, a much more meaningful comparison is derived if the range of voltages is restricted to go from 0.4 V to 2 V. In table 6.3 the results are reported for that case.

**Table 6.3:** Average percentage difference between the integrals of the TS of DFT and EHT or Slater-Koster for 2 V of applied voltage, starting from 0.4 V.

	<b>Slater-Koster</b>	<b>EHT</b>
<b>Clean</b>	6.44%	15.30%
<b>O<sub>2</sub></b>	7.99%	19.44%
<b>CO<sub>2</sub></b>	4.28%	14.61%
<b>N<sub>2</sub></b>	11.34%	15.22%
<b>H<sub>2</sub>O (O down)</b>	11.84%	15.78%
<b>H<sub>2</sub>O (O up)</b>	5.90%	5.94%
<b>Ar</b>		14.53%

As expected, Slater-Koster shows much lower differences with respect to those of EHT in comparison with DFT. However, in the final range of voltages taken into account, the results of EHT are quite close to the others, confirming the good behaviour of this method. It is also interesting to notice that EHT usually underestimates the TS, in accordance with what noted previously, that is to say the poor ability of EHT of replicating the TS for low energies. This trend is positive for the purpose of creating a sensor as, if a certain selectivity is revealed by EHT, DFT calculations may even show an increase of that property. On the other hand, Slater-Koster overestimates the variations, possibly suggesting the selectivity with respect to a specific target which is then not verified by DFT.

In light of this validation, considering that Slater-Koster could not be employed for the next analysis, and that the computational cost associated to out of equilibrium analysis with DFT made the studies unfeasible, it has been decided to proceed further by using EHT as the main tool for current analysis.

Before proceeding, it is important to understand how crucial it is to have good variations in the equilibrium properties of the system in correspondence of the Fermi level. Indeed, as demonstrated in the previous chapters, the bias window is centered around that energetic position. This means that it is possible, having good modifications there, to possibly work with the sensor at low bias conditions, thus keeping power consumption low. If that will be the case, also in the presence of common pollutants, it may also be reasonable to think of having a good sensitivity and hence a good sensor overall. Furthermore, for low biases, as just demonstrated, EHT is expected to provide better results.

### 6.3 Analysis out of equilibrium

Having verified the quality of the EHT method for equilibrium studies, it is time to analyze the behavior of the system when a voltage is applied between the two electrodes. Again, due to computational limitations of the employed machine, studies of this kind could not be performed with DFT and, since Slater-Koster would have provided incomplete results, the use of EHT was hence forced.

In figure 6.10 the  $I(V)$  characteristic is reported in the case of free air species present in the environment. The employed settings for the evaluation of it are reported in table 6.4. Notice that, since the developed device is symmetric, the range of applied voltages was just chosen on the positive side, as it is expected that also the current is symmetric with respect to positive or negative biases and that, given the validation check of before, the range of voltages has been limited below 3V.

As shown from the graph, and as expected from the analysis at equilibrium, the interaction with other species is well detected by the sensor, which presents a

variation of the current as a function of the species introduced and of the applied bias.

**Table 6.4:** IV curve block settings. If not specified, default settings have been employed.

	<b>IV curve</b>
<b>Voltage Bias</b>	$V_0 = 0 \text{ V}$ $V_1 = 3 \text{ V}$ Points: 11
<b>Energy range</b>	$E_0 = 0 \text{ eV}$ $E_1 = 2 \text{ eV}$ Points: 101
<b>k-point Sampling</b>	Grid Type: Monkhorst-Pack grid $n_a = 7$ $n_b = 7$

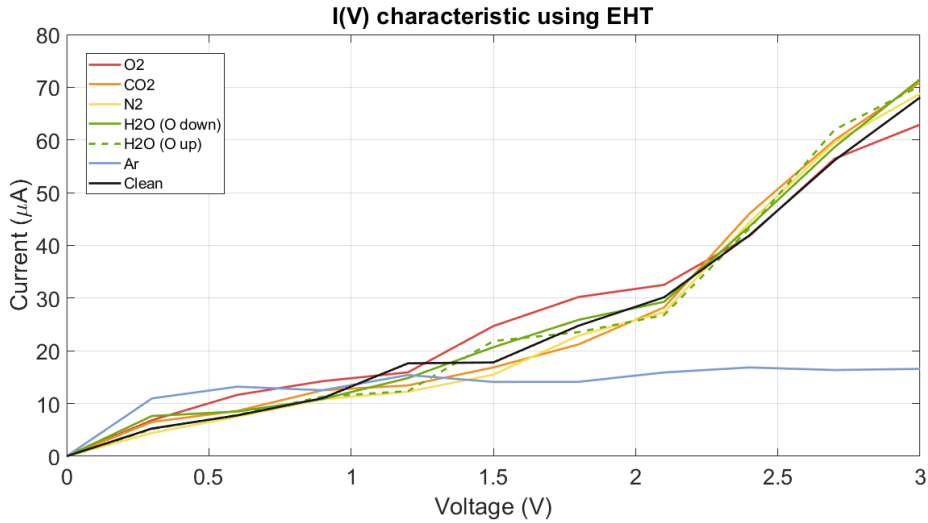


**Figure 6.10:** Current flowing as a function of the voltage applied in the presence of external species interacting with the channel using the EHT method.

Nevertheless, there does not seem to be a trend regarding the polarity or not of the molecule considered, as both the water molecule orientations provided a very similar modification in the properties, thus confirming the result from the Mulliken population analysis, that is the very small electric charge unbalance through the

system not being able to enforce the interaction with a more positively charged species like the water molecule with hydrogen pointing towards the negatively charged carbon atom.

Another thing to consider is that the interaction is not independent with respect to the bias applied, meaning that, fixed a specific species, its effect on the device is not always an increase or a decrease of the charge flowing. Furthermore, it is interesting the variation induced by the argon atom which, although providing a similar effect with respect to the one of other species at low bias, for voltages bigger than 1.5 V causes a stop in the increase of the current, which flats at an almost constant value.

Finally, while it is true that the transmission spectrum is dependent on the voltage applied, nevertheless for small bias the previously noted peak due to the O<sub>2</sub> molecule in the LUSO side may be considered as the main cause of a greater current in the region below 2 V. This point will be further discussed in the following. However, this further confirms that the sensor does not seem capable of modifying its characteristics in a specific way when a polar species is inserted in the channel, as the O<sub>2</sub> molecule is non-polar and a Mulliken population analysis did not suggest an electric charge unbalance within that molecule caused by the interaction with the sensor. It is to notice that the position at which the O<sub>2</sub> molecule has been placed with respect to the fullerene is quite similar to the one enforced on the N<sub>2</sub> molecule, which however did not provide the same variation in the current. This is reasonable if the possibility of having a stronger interaction with respect to simple physisorption is taken into account. In that regard, N<sub>2</sub> is an inert gas and should hence not react with other species, thus leading to small current variations in comparison to the one caused by O<sub>2</sub>, which instead is highly reactive and the carbon-oxygen bonding is known to be covalent for distances in the order of a nanometer. In that sense, maybe the specific C-O bonding is stronger than simple physisorption but not as strong as the one found in the CO molecule.

To sum it up, this first analysis with common species present in the atmosphere suggests that the sensor might be able to provide considerable current variations either when a high atomic number species is inserted in the channel, and that is the case of the argon atom, or when a reactive species is able to create a stronger bonding with the carbon atoms of fullerene, and that is the case of the oxygen molecule. If that is the case, the analysis in the presence of additional possible pollutants should confirm that only high atomic number based species would modify the current to a great extent, whereas low atomic number polar molecules do not.

To close this section, in order to provide a more concrete description of the behaviour of the system with an applied voltage the current variation and the percentage variation at each bias point have been evaluated and plotted in figure 6.11. Considering the good variation in the current observed at 1.5 V, this could be a good bias point for the sensor to work with, of course only in the case in which a

variation also occurs for other species and that that modification is different with respect to the one associated to free air molecules.

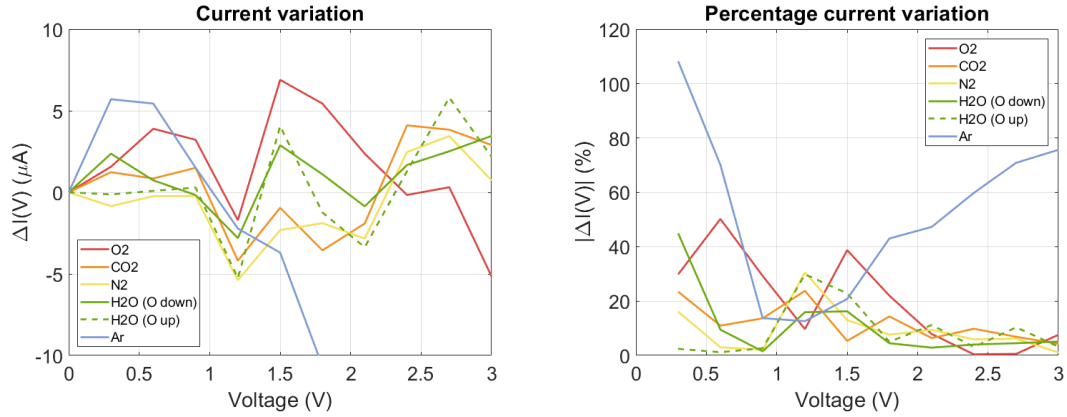


**Figure 6.11:** Current variations (left) and percentage variations (right) at each bias point in the presence of external species naturally found in the environment.

### 6.3.1 Oxygen molecule induced current variation

It is interesting, at this point, to understand more concretely what is the effect of the presence of the oxygen molecule.

Lets consider for example the current flowing with an applied voltage of 1.5 V. At this bias point, a good current variation is produced by the presence of that species nearby the channel. To understand why this occurs it is possible to consider the transmission spectrum, reported in figure 6.12, and analyze it in more details.

First of all, this transmission spectrum confirms what has been previously observed, that is that the increase in the current with respect to the clean sensor has to be addressed to the peak above the Fermi level, located at 0.68 eV. In fact, considering that this portion of the TS only enters in the bias window for the imposed voltage, it is reasonable to associate that peak to the increase of current. Furthermore, the peak at 0.42 eV is higher with respect to the clean sensor case.

Things are instead not that clear for energies below the Fermi level, where for certain energies the TS for the clean sensor shows higher peaks whereas in other positions the oxygen molecule provides more transmission.

The transmission spectrum can, at this point, be exploited for a much deeper study. For a specific energy a certain value of transmission is obtained. This value can be calculated either as the trace of the transmission matrix, or as the sum of the eigenvalues of such matrix [72]. This means that the flow of charges through the system does not occur as the motion in a channel with a transmission probability

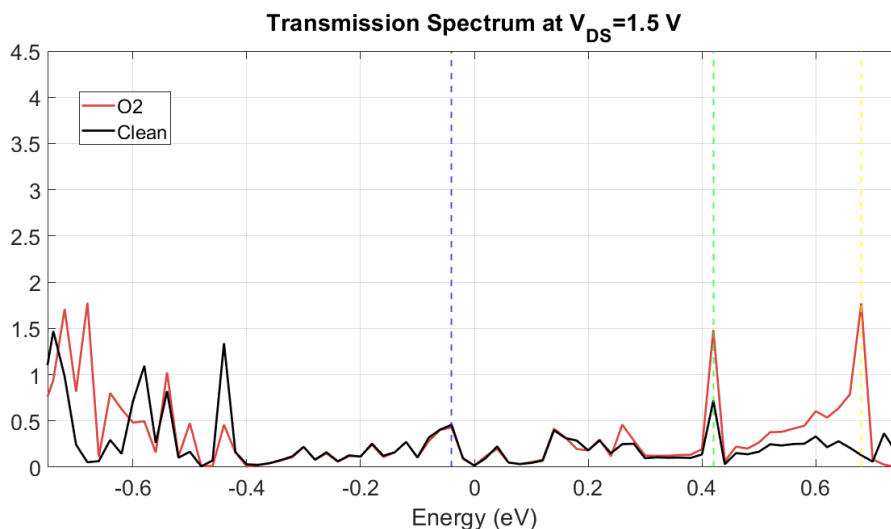


**Figure 6.12:** Comparison of the transmission spectrum at 1.5 V for the clean sensor and the sensor in the presence of oxygen. The dashed blue vertical line is fixed at  $-0.04$  eV, the green one at  $0.42$  eV and the yellow one at  $0.68$  eV.

comprised between 0 and 1. Instead, transport occurs by means of several channels, each having a specific eigenvalue and eigenfunction, which represents, in real space, the surface of iso-energy for transmission.

Furthermore, in order to have an even simpler insight of transmission, it is possible to divide the total transmission into single contributions between pairs of atoms, and show in real space the pathways followed by charges.

All these studies can be performed with the employed tool by choosing an energy value.

To begin with the analysis, let's focus on the small peak at  $-0.04$  eV. For this value of energy the presence of the oxygen molecule does not have an impact on the TS, so it is expected that the path followed by charges does not include oxygen. Exploiting the *TransmissionPathways* block in *ATK*, figure 6.13 has been achieved. As expected, there is no path connecting the  $O_2$  molecule and the fullerene, so that the transport in the system is basically unchanged with respect to the clean sensor case.

As far as the eigenvalues and eigenstates associated to that peak are concerned, only one eigenvalue greatly contributes in transmission, with a value of 0.21, whereas all the others are orders of magnitude lower and are not expected to contribute to a great extent. This is particularly evident by taking a look at the correspondent eigenstates, reported in figure 6.14. For the value just mentioned the eigenstate is displaced in the whole system, meaning that the incoming wave is able to propagate

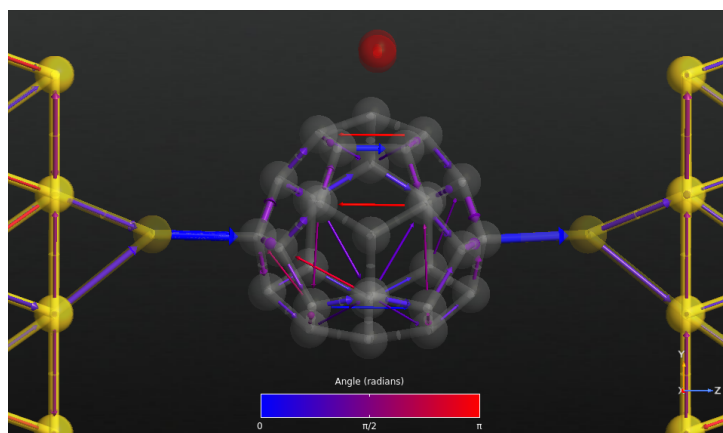


**Figure 6.13:** Transmission pathways for  $E = -0.04$  eV. Colors are related to the direction of propagation, so that blue arrows represent motion from left to right whereas red ones from right to left.

through the system and reach the second electrode. For the second eigenvalue, instead, propagation is limited and the eigenstate is localized nearby one electrode. Notice, however, that the presence of  $O_2$  does not contribute in the eigenstate, as the iso-energy surface involving the external molecule does not connect the left side of the fullerene to the right one.

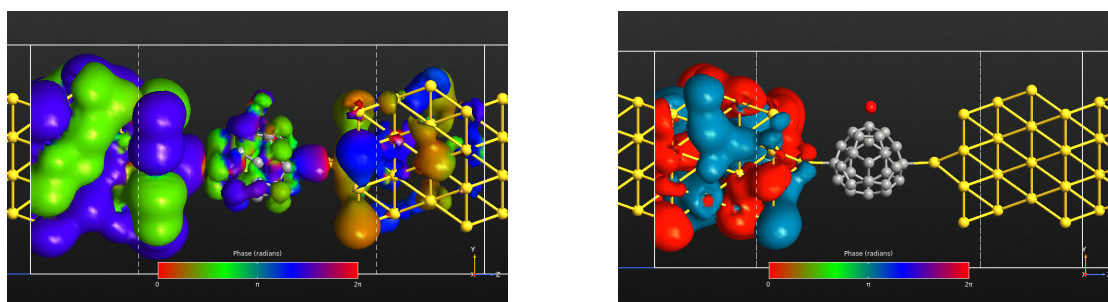


**Figure 6.14:** Transmission eigenstates at  $E = -0.04$  eV for the highest eigenvalue, equal to  $2.14e-1$  (left) and the following one, equal to  $1.55e-6$  (right), for applied voltage of 1.5 V in the presence of oxygen.

Quite different is the behaviour at 0.42 eV. Here the presence of the oxygen molecule is able to cause a great increase in the transmission. As before, however, only one eigenvalue represents the main contribution to the total transmission and

is thus the only one considered. In figure 6.15 the transmission eigenstates related to that eigenvalue are reported for the clean sensor and in the case of the presence of the oxygen molecule.

As expected, the eigenstate for the whole system is, in general, not affected, exception made for the top region of the fullerene, where the presence of  $O_2$  modifies the iso-energy surface, potentially creating a further region of transport, considering that it involves the left side of the fullerene as well as the right one, differently with respect to what happened with the previous considered value of energy. This is clear by looking at the pathways, shown in the same figure. With the presence of the oxygen molecule a new path for transmission is present, hence causing the observed increase in the TS.

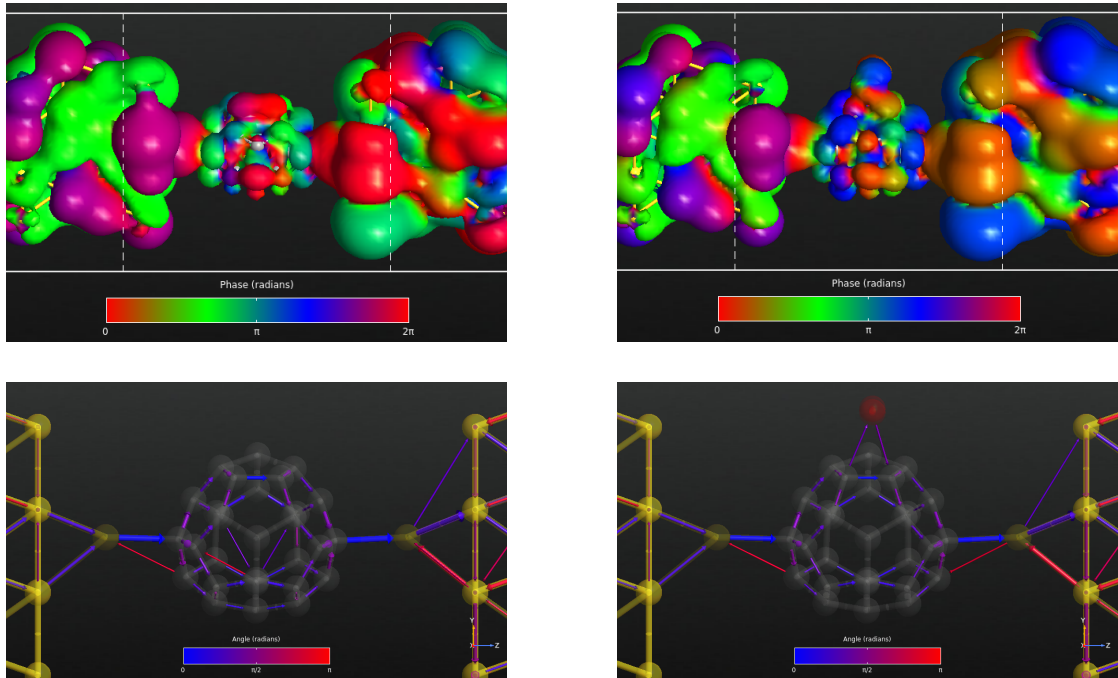


**Figure 6.15:** Transmission eigenstates and pathways at  $E = 0.42$  eV for the highest eigenvalue considering the clean sensor (left) and the presence of oxygen (right) for applied voltage of 1.5 V.

A final analysis which may be performed regarding the transmission for the case under analysis is the one on the MPSH, to understand which orbitals are involved the most during transport. This study may also allow to justify why the behaviour in the presence of oxygen is observed. In appendix B the MPSH related to the first HOSO and LUSO level is reported, as well as a zoomed image of the transmission eigenstate for the system. It is clear, from these images, that the transmission of

charges from one side to the other occurs by means of transmission channels which eigenstates resemble closely the MPSH for the HOSO level.

Furthermore, this system orbital is characterized by a good delocalization of the iso-energy surface which involves one lobe of the oxygen orbital and the one of carbon atoms in the fullerene, suggesting that the interaction is indeed stronger than physisorption. However, it is also important to highlight how the system orbitals nearby the oxygen molecule have a shape which can be associated to the typical one found in diatomic molecules, suggesting that, while a certain amount of delocalization may be present, it is however not as extended as to form a strong covalent bonding between carbon and oxygen, thus confirming, at least qualitatively, what previously said, that is that the variation in the current flowing through the system is caused by a stronger interaction.

# Chapter 7

## Target research

In the previous chapters a gold-C<sub>28</sub> molecular junction has been realized from the theoretical point of view and simulated in the presence of species commonly found in the atmosphere.

This allowed to verify its ability to modify its properties when external elements are inserted nearby the sensing region, that is the fullerene, suggesting however that the sensor is not expected to provide meaningful variations when simply polar molecules are considered but only when the interaction occurs with highly reactive species or species with an high atomic number. In this second case, which with free air species only occurred with argon, the modification of the system either takes place because of the inertness of the target (indeed argon does not react with other elements forming compounds) and so due to the steric effect related to overlapping electronic clouds [73], or due to the combined effect of the high atomic number and the creation of an induced dipole moment stronger with respect to those of other species. In the former case, the interaction with argon should be unique and not reproduced by any other pollutant, as long as atoms with incomplete octet are present, whereas in the latter case molecules made of atoms having an high atomic number may lead to similar variations.

To complete the characterization of the device, the purpose of this chapter is to check whether a possible analyte for the sensor exists, placing different possible pollutants nearby the sensor to study their effect on its I(V) characteristic.

To be more precise, in section 7.1 the analysis in the presence of pollutants which have been demonstrated in literature to pose a threat for health are performed. The species considered are CO, NO, NO<sub>2</sub>, SO<sub>2</sub>, NH<sub>3</sub>, CH<sub>4</sub>, C<sub>6</sub>H<sub>6</sub>, C<sub>7</sub>H<sub>8</sub>, C<sub>8</sub>H<sub>10</sub>, PbO and PbSO<sub>4</sub>.

Then, in section 7.2, the results obtained in this and in the previous chapter are put in comparison with the ones retrieved with a similarly conceived fullerene C<sub>60</sub> based sensor, in order to try finding a connection between the behaviour of devices exploiting fullerenes. This analysis will be carried both for the free air species of

the previous chapter and for some of the pollutants analyzed in section 7.1.

## 7.1 Possible targets analysis

In this section a series of pollutants are taken into account to find a possible target for the sensor. The positions at which such species have been placed in the channel are similar with respect to the ones used for free air species (refer to appendix C for further details). For ease of comparison with the  $C_{60}$  based sensor, the range of voltages reported is limited to 2 V.

### Carbon monoxide interaction

The first considered pollutant is carbon monoxide (CO). It is characterized by the presence of a triple covalent bond between carbon and oxygen and is formed by the incomplete combustion of carbonaceous materials or by the reduction of carbon dioxide [74]. Prolonged exposure to it may be fatal, and considering it is odorless, tasteless and colorless, its detection requires the use of specific sensors [74].

Of course, since the two atoms bonded to create such species have a difference in electronegativity higher than 0.4, the CO molecule is polar and so two different orientations have been considered.

In figure 7.1 the currents and the current variations with respect to the previously analyzed species are reported.

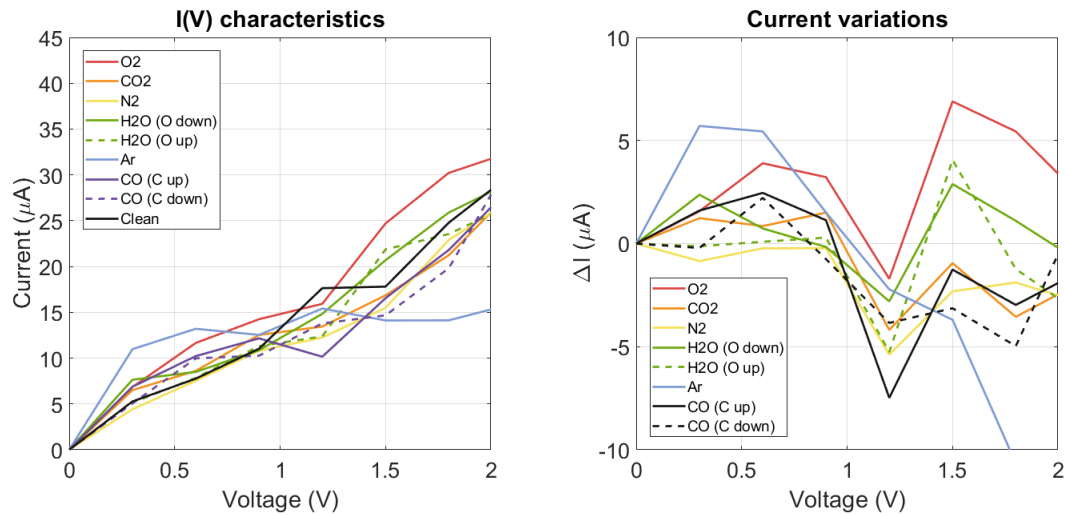


**Figure 7.1:** Currents (left) and current variations (right) at each bias point in the presence of carbon monoxide.

As expected from the discussion of the previous chapter, the interaction with this species does not provide too extended variations in the current.

However, at 0.6 V of applied bias, the selectivity of the sensor seems to be verified for both the orientations, possibly allowing its detection.

### Nitrogen monoxide interaction

The second pollutant inserted is nitrogen monoxide (NO), which is characterized by the presence of a double bond that however leaves an unpaired electron. For this reason it is a radical and expected to have a low lifetime, leading to the formation of nitrogen dioxide.

The reaction between oxygen and nitrogen to form this compound occurs at high temperatures, meaning that it is typically obtained from the combustion of coal and oil at electric power plants, but also during the combustion of gasoline in automobiles [75]. It is a colorless gas with high toxicity if inhaled or brought in contact with the skin [76].

As for the CO case the molecule is polar due to the difference in electronegativity between the two elements.

Considering figure 7.2, there does not seem to be a bias point for which both the orientations considered provide the same variation. However, if the possibility of having different modifications is taken into account, it may be possible to work at 0.9 V.

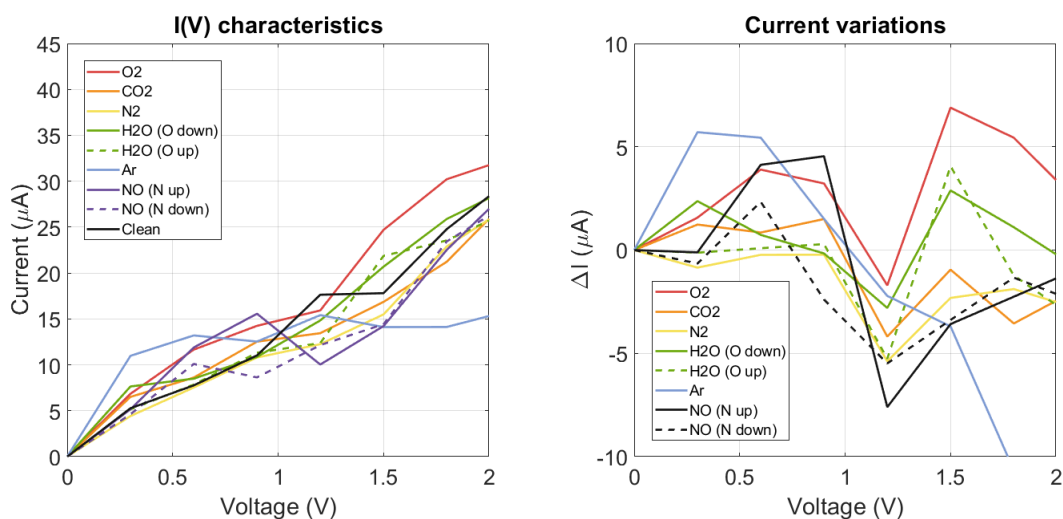


**Figure 7.2:** Currents (left) and current variations (right) at each bias point in the presence of nitrogen monoxide.

## Nitrogen dioxide interaction

As previously said, NO typically leads to the formation of nitrogen dioxide ( $\text{NO}_2$ ). In this case one oxygen atom is bonded to the nitrogen atom by means of a single bond whereas the other by a double bond. It is primarily released in the atmosphere from the burning of fuel, and hence from cars and trucks, but also from power plants and off-road equipment [77].

It is a highly poisonous gas, as the exposure to it produces inflammation of lungs which may result in an edema leading to death, and appears like a reddish brown gas [78].

As for other species, the molecule is polar with the nitrogen atom partially charged positively, whereas the oxygen atoms are charged negatively.

In figure 7.3 the currents and current variations are reported. Once again, there are no bias points for which the variation is detectable for both orientations, in agreement with the studies on free air species. Furthermore, it is important to notice how the variation of the current at 0.6 V for one orientation of both nitrogen dioxide and monoxide is very close to the one observed for carbon monoxide, thus removing that bias point from being a valid option for the detection of CO.

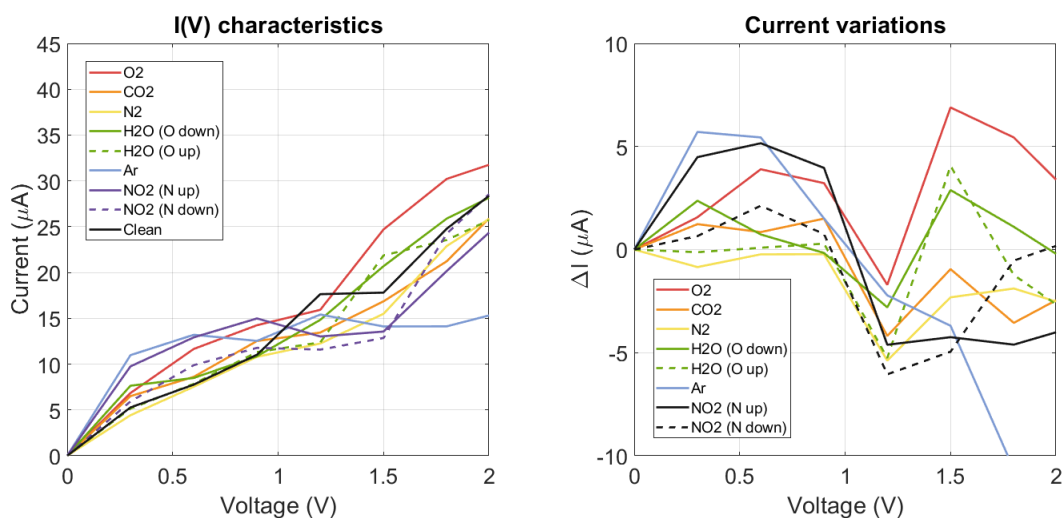


**Figure 7.3:** Currents (left) and current variations (right) at each bias point in the presence of nitrogen dioxide.

## Sulfur dioxide interaction

Sulfur dioxide ( $\text{SO}_2$ ) is a polar molecule constituted by two double bonds connecting the sulfur atom (which is positively charged) to the oxygen ones (which instead

are negatively charged).

It is mainly released in the environment through the burning of coal and oil at power plants or from copper smelting, presenting itself as a colorless gas with pungent odor [79]. It is toxic if inhaled and irritates eyes and mucous membranes [79].

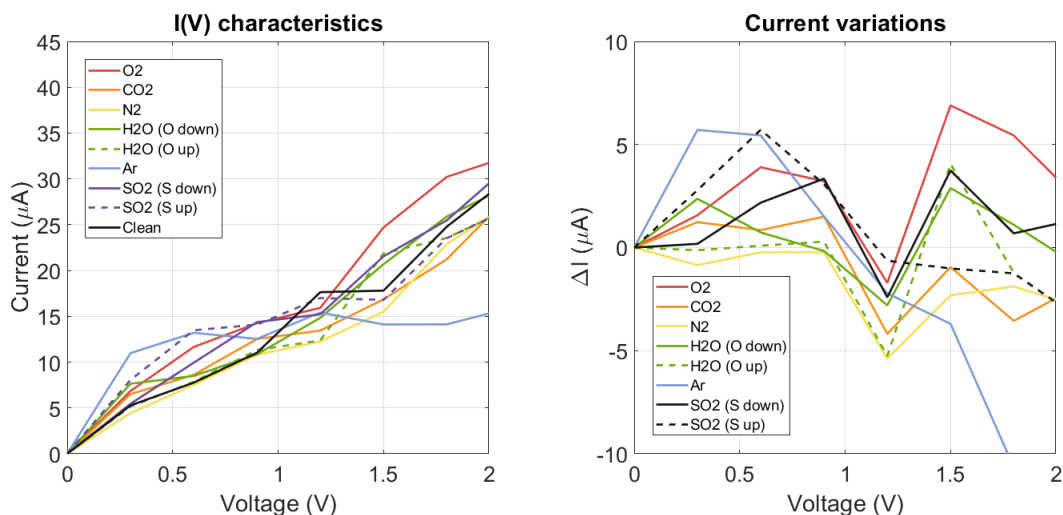


**Figure 7.4:** Currents (left) and current variations (right) at each bias point in the presence of sulfur dioxide.

In this case, the two considered orientations did not provide similar modifications on the current of the system, as shown in figure 7.4. Moreover, such variations are close to the ones caused by other species, hence removing this molecule from being a possible target for the sensor.

### Ammonia interaction

Ammonia ( $\text{NH}_3$ ) is a colorless gas with a strong odor made of a nitrogen atom bonded to three hydrogen atoms, leading to a polar molecule where the negative side is represented by the nitrogen atom.

Its main sources include agriculture, animal husbandry, industrial processes and vehicular emission [80]. As for the other species considered it may cause health issues if inhaled.

The analysis of the currents and current variations, reported in figure 7.5, shows that the sensor is not able to distinctly detect the presence of this molecule with respect to other species.

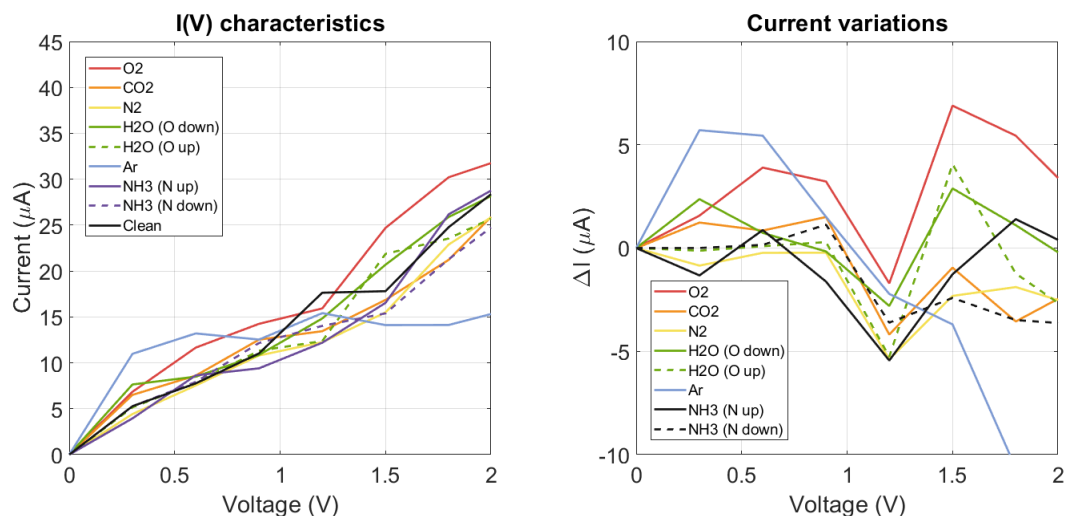


**Figure 7.5:** Currents (left) and current variations (right) at each bias point in the presence of ammonia.

### Hydrocarbons interaction

An important class of pollutants which detection may be of interest is the one of hydrocarbons, that is to say systems constituted by carbon and hydrogen atoms, bonded together by means of single, double or triple bonds. It is commonly accepted that they generally lead to important health issues. For example, benzene ( $C_6H_6$ ), toluene ( $C_7H_8$ ) and xylene ( $C_8H_{10}$ ) are known to be adsorbed through the lungs and transported by the bloodstream to the central nervous system, where they act as depressants [81]. Others, like methane ( $CH_4$ ), despite not being toxic, are flammable gases and contribute to the greenhouse effect.

As far as the main anthropogenic sources for hydrocarbons are concerned, methane is emitted from landfills, oil and natural gas activities, as well as agricultural activities, coal mining, wastewater treatment and industrial processes [82]; benzene, instead, is widely used in industrial processes for the production of plastics, resins, detergents and pesticides [83]; toluene is used for similar purposes with respect to those of benzene, but also to manufacture benzene itself [84].

In the viewpoint of studying their effect on the properties of the system developed thus far, methane, benzene, toluene and cyclooctatriene ( $C_8H_{10}$ ) have been taken into account. It is important to highlight that these species are not expected to be polar, and so only one orientation has been tested for each of them. This choice is also justified by their sizes, which are typically in the order of the ones of the fullerene and of the nanogap, thus limiting the interaction to the hydrogen atoms, as, in order to interact by means of carbon, they should be placed parallel to

the system, in a position which is unlikely to occur due to the aforementioned dimensions. Then, since the neighboring region of such hydrogen atoms is usually the same, variations in the position should not lead to great differences.

Looking at figure 7.6, where once again the currents and the current variations are reported for the species under analysis, the detection of the considered hydrocarbons seems to be possible for the toluene at 1.5 V (even though this variation is similar to the one enforced by the presence of  $\text{NO}_2$ ) and for cyclooctatriene at 1.8 V, which instead is considerably different with respect to what observed up to now.

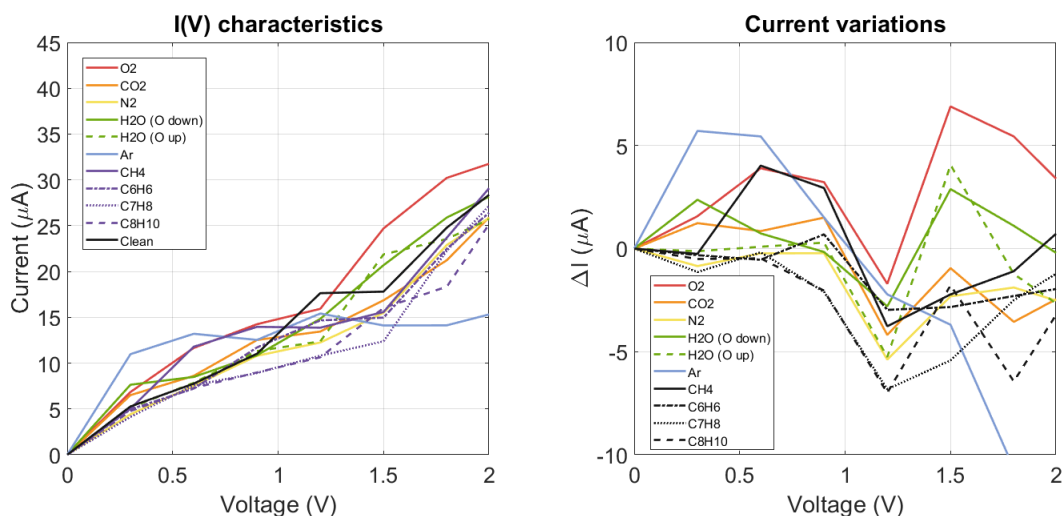


**Figure 7.6:** Currents (left) and current variations (right) at each bias point in the presence of different hydrocarbons of interest.

These results are quite interesting, considering the non polar nature of the species involved and the small atomic numbers of the various atoms. In fact, taking into account these two factors, the variations in the current should not be as extended as they are, once again pointing towards the direction of a stronger interaction with respect to simple physisorption.

### Lead based compounds interaction

Lead is typically released in the environment through burning of leaded petrol as well as smelting and refining of lead in specific industrial processes [85], even though its use has been greatly reduced in the last years. It is usually not found alone in the form of free atoms like in the case of argon but instead creates compounds like lead monoxide ( $\text{PbO}$ ) and lead sulfate ( $\text{PbSO}_4$ ), which have been considered as possible targets for the sensor. Both these compounds are constituted by an ionic

bond, which means that one side has a negative ion whereas the other a positive one, thus showing a strong polarity. Therefore, as in the case of polar covalent bond, two different orientations have been enforced.

Lead based compounds are expected to adversely affect the nervous system, kidney function, immune system, reproductive and developmental systems and the cardiovascular system, but also the oxygen carrying capacity of the blood [86].

If the hypothesis of having a strong modification in the properties of the sensor caused by the high atomic number of the atoms involved is correct, the interaction with the just mentioned compounds should provide a good variation in the current flowing and so the possibility of detecting such targets with a reasonable selectivity. In fact, lead has 82 electrons, meaning that its compounds are expected to cause quite extensive variations.

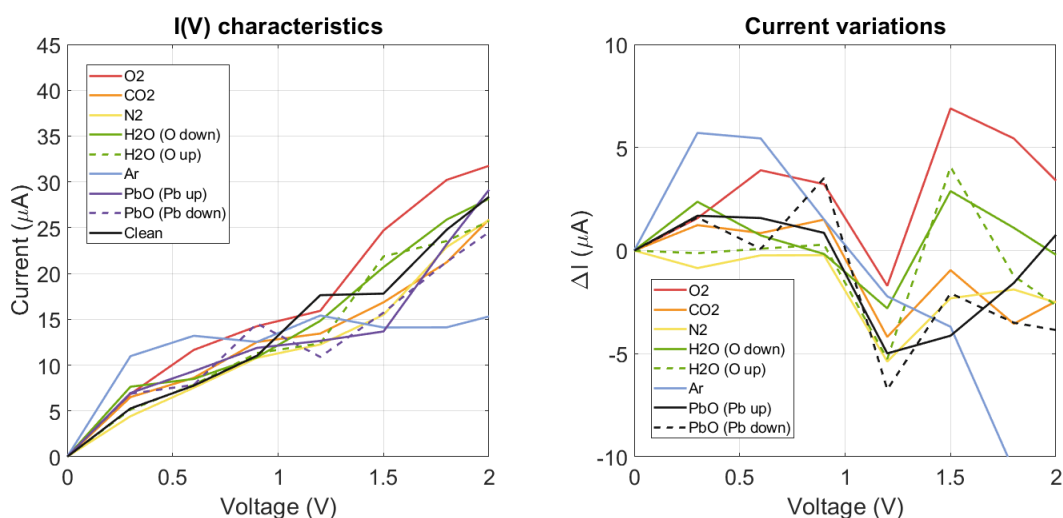


**Figure 7.7:** Currents (left) and current variations (right) at each bias point in the presence of lead monoxide.

As shown in figures 7.7 and 7.8, not only different orientations led to different variations, but these modifications are not univocally associable to the species introduced, thus not allowing the detection of PbO or PbSO<sub>4</sub> with a certain degree of selectivity. Moreover, the extensions of the variations are comparable, especially for PbO, to other polar and non polar species.

These analysis therefore disregard the C<sub>28</sub> sensor from being employed for the detection of molecules having an high atomic number and for which the Van Der Waals interaction caused either by the already present dipole moment or by the induced one may be revealed.

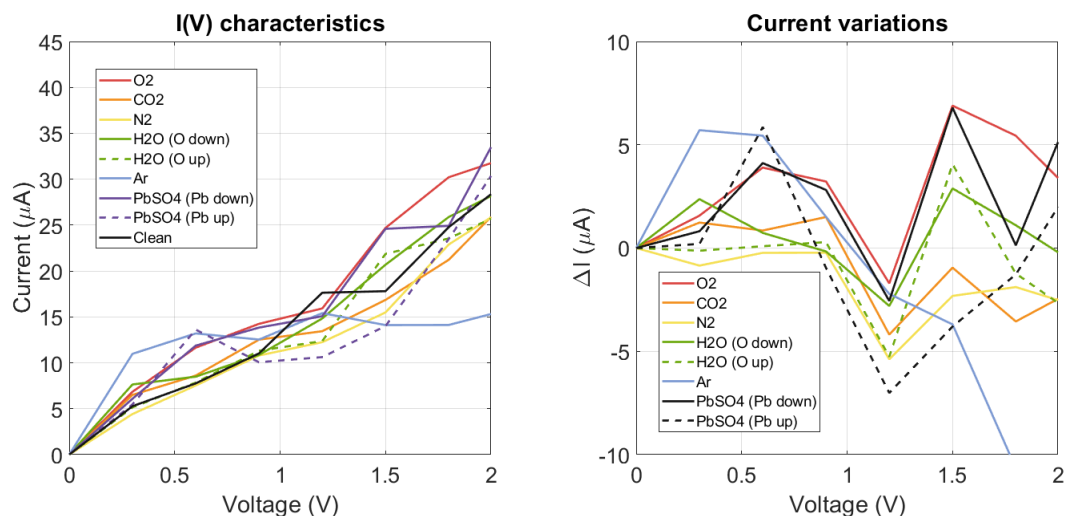


**Figure 7.8:** Currents (left) and current variations (right) at each bias point in the presence of lead sulfate.

## 7.2 Comparison of results with a fullerene $C_{60}$ based sensor

As shown in chapter 6, the  $C_{28}$  based sensor resulted to be able to modify its properties in the presence of free air species inserted nearby the fullerene. Those variations suggested that the device could be able to sense other species, either in the case of particularly reactive elements, as for the oxygen molecule, pointing towards the direction of a stronger interaction with respect to simple physisorption, or in the case of species having a high atomic number, leading to stronger Van Der Waals interaction caused by an induced dipole moment.

Then, in section 7.1, various pollutants have been considered and, as expected, the modifications exerted by polar pollutants having small atomic number atoms could not be identified with high enough selectivity. In fact, even though certain species, like CO, NO and  $C_7H_8$ , provided good modifications if considered separately, they however led to close effects if compared to other pollutants.

Unfortunately, also the hypothesis of having a good selectivity with respect to high atomic number atoms based species did not result to be true, as the interaction with lead compounds could not be detected, thus revealing the inadequacy of the gold- $C_{28}$  molecular junction structure developed in the previous chapters from being used as a sensor for a desired target.

To conclude the work, in this section the results obtained with the  $C_{28}$  sensor developed thus far are compared with the ones retrieved with a similarly conceived

fullerene  $C_{60}$  based sensor, which has been provided to me by one of my supervisors. The structure is very similar to the one employed in this work, that is to say a molecular junction with the contacts made of gold. Differently from the  $C_{28}$  system, however, the use of adatoms was not necessary, as the geometry optimization analysis revealed the stability of the molecule within the nanogap even in their absence.

Nevertheless, the various analysis performed on his part have been carried out with a methodology which closely resembles the one followed during this work, both in methods and tools employed.

Therefore, it may be interesting to compare the derived results to see if there is a common behaviour between the two systems, maybe allowing to pose a base for sensors exploiting fullerenes as the sensing region.

### 7.2.1 Free air species interaction

To begin with the comparison the interaction with free air molecules is considered in this part. Before proceeding it is important to notice that the range of voltages considered for the provided sensor was limited to 2 V, hence the reason for which the previously reported pollutants graphs have been also restricted to that range, even though the spacing of bias points is different.

In figure 7.9 the currents and the current variations are reported for the  $C_{60}$  based sensor.

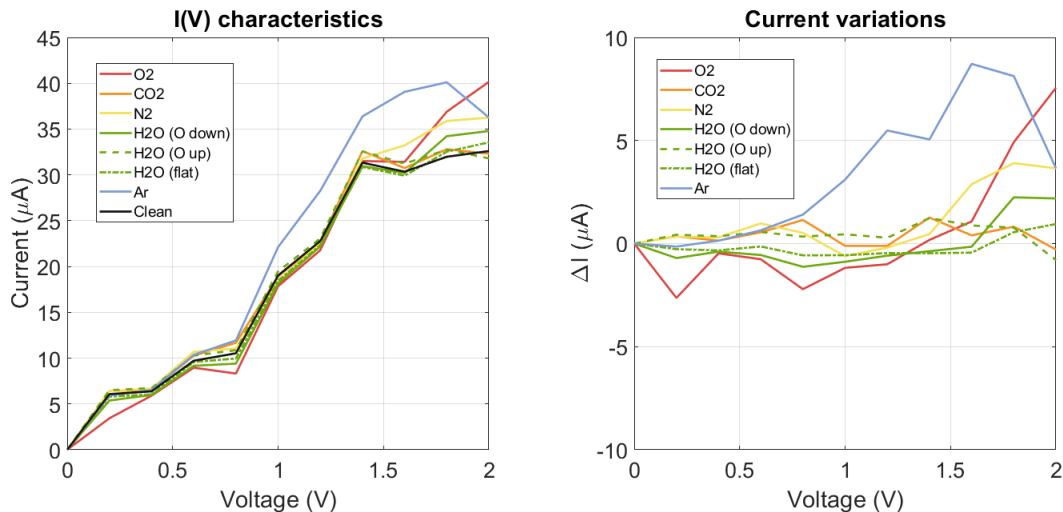


**Figure 7.9:** Currents (left) and current variations (right) at each bias point in the presence of free air species, for the  $C_{60}$  based sensor.

As shown, also this sensor is able to produce modifications on its  $I(V)$  characteristic due to the interaction with other species. Nevertheless, such modifications are far less extended with respect to those of the  $C_{28}$  sensor. The motivations for which this is the case are quite simple. First of all, the smaller fullerene is expected to be more reactive due to the radius of curvature and to the presence of the four unpaired electrons as individuated by literature studies. Furthermore, even if that was not the case, it is reasonable to observe a much wider variation in the current considering the smaller number of transmission pathways present in the system. While the  $C_{60}$  molecule is quite large (almost double in size) and so a lot of paths for transmission allow the flow of charges through it, for the  $C_{28}$  this number is smaller. Moreover, as shown with the analysis of the previous chapter on the induced effect of the  $O_2$  molecule, one of the main paths for transmission includes the top pentagon of the fullerene, nearby which all the additional species have been placed, and that also involves one of the atoms where the unpaired electron should be located, thus enhancing to a greater extent the interaction.

Different is the case of the  $C_{60}$  fullerene, for which, as shown in figure 7.10, the transmission pathways for the clean  $C_{60}$  sensor are distributed all over the system, with an high concentration also below the fullerene, far from the position at which the molecules have been placed (i.e. in the upper region of the sensor, in a similar fashion, both in distances and location, to the ones enforced for the  $C_{28}$  sensor).

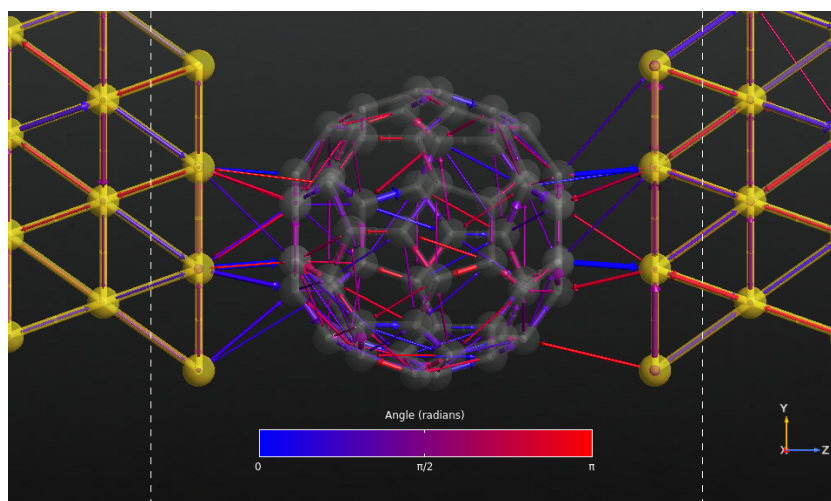


**Figure 7.10:** Transmission pathways in the  $C_{60}$  sensor for the highest peak in the transmission spectrum, located at  $0.4\text{ eV}$ , with  $1.4\text{ V}$  of applied voltage and in the absence of external molecules. As usual, colors represent the direction of motion.

While the variations are less extended, for the just mentioned reasons, the overall

behavior of the device is quite close to the one of this work. In fact, the same inconsistency for different voltages but for the same molecule are present, with an interaction that depends on the applied voltage, even though it has to be noted that the  $C_{28}$  sensor shows modifications already extended at low biases, whereas the  $C_{60}$  one only for higher ones.

It is also interesting to notice that the interactions with argon and with the oxygen molecule lead to bigger modifications in comparison to the one of other species, again in agreement with what observed with the  $C_{28}$  sensor, suggesting again that the sensing ability of fullerenes could be related to the reactivity of the introduced species and/or to the atomic number.

## 7.2.2 Interaction with pollutants

The provided  $C_{60}$  sensor was first envisioned having the purpose of detecting the presence of ammonia in the environment. Unfortunately, the variation induced by that molecule could not be identified with high enough selectivity with respect to free air species, thus removing it from being a possible analyte. It was first assumed, then, that the molecular mass and the number of electron states could be a discriminatory factor for the detection of species, and therefore the sensor was made to interact with methane and butane ( $C_4H_{10}$ ), leading to the results reported in appendix C. While only one of the hydrocarbons considered coincides with the ones used in the previous section, there is an important difference in the  $C_{60}$  sensor and the  $C_{28}$  one. In fact, in the former case the interaction with hydrocarbons almost does not modify the  $I(V)$  curve at all, whereas in the latter each of the introduced species caused good variations at different biases, even though the selectivity was just verified for  $C_7H_8$  and  $C_8H_{10}$  at one bias point. This further highlights the higher reactivity of the sensor working with the smaller fullerene.

Having discarded that option from being a possibility for the research of a target for the sensor, the analysis was then moved to polar molecules, which were assumed to be responsible for bigger variations. Indeed, as in the case of the  $C_{28}$  sensor, since the argon atom lead to big current variations, and considering it does not react in a chemical way with other atoms, it has been speculated that the atomic number and the polarizability of the target may be the cause of the current variations, which do not result to be extended for simply polar molecule but for molecules with atoms having an high atomic number, and for which a strong polarization may be induced.

Moving in that direction, species like CO, NO,  $NO_2$  and so on, caused selective variations, possibly allowing their detection for certain bias points, as shown in figure 7.11.

However, it is to notice that, similarly to what happens for the  $C_{28}$  sensor, different orientations of the target caused considerably different variations in the

current, and so the aforementioned selectivity is verified only if it is accepted that the variations for different orientations may not be the same, i.e. for a certain bias point one orientation provides, for example, a decrease in the current whereas the other an increase, but both are different with respect to other targets. In that sense, as noted previously, also the  $C_{28}$  sensor is able to detect the NO molecule at 0.9 V, since the two orientations imposed are well detectable with respect to free air species.

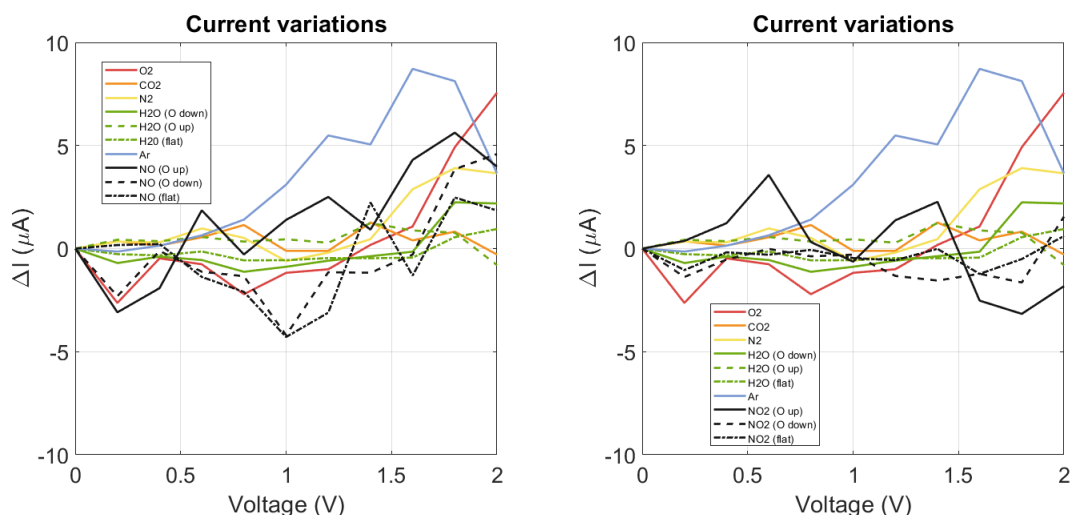


**Figure 7.11:** Current variations for NO (left) and  $NO_2$  (right) at each bias point for the  $C_{60}$  based sensor.

Proceeding with that hypothesis, heavy metals compounds, mainly lead based, were considered. In this case the selectivity is verified with the same conditions just mentioned, for all the lead based compounds, as shown in figure 7.12. In this case, their effect on the current are much more evident with respect to those observed with the  $C_{28}$  sensor, for which neither the lead monoxide or the lead sulfate caused significantly different variations in comparison with other species.

Again, as in the case of other pollutants and as for the  $C_{28}$  sensor, there is a strong dependence on the applied bias, as particularly evident from the interaction with  $PbCl_2$ , for which each voltage provides a different modification.

With the considerations made it is possible to draw some conclusions. First of all, the reactivity of the  $C_{28}$  sensor allowed the device developed in this work to produce much more extended current variations with respect to the ones of the  $C_{60}$  sensor. Both of them result to be particularly reactive to the oxygen molecule, which in both cases causes an increase of the current at around 2 V, and to argon, which in the  $C_{28}$  case provokes a decrease in the current, and moreover a stop in

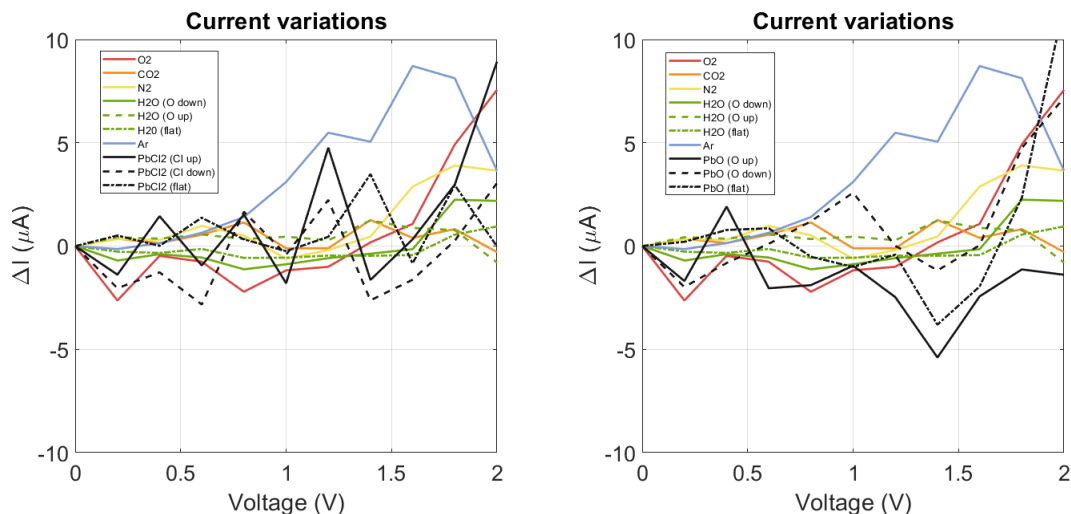


**Figure 7.12:** Current variations for  $\text{PbCl}_2$  (left) and  $\text{PbO}$  (right) at each bias point for the  $\text{C}_{60}$  based sensor.

the variation of it for higher voltages, whereas in the other case an increase of it, even though the trend suggests that for voltages higher than 2 V it may lead to a considerable decrease in the current or at least a variation more similar to the one of other molecules. As far as the  $\text{O}_2$  molecule induced current variation is concerned, it is reasonable to assume that the interaction may be intermediate between physisorption and chemisorption, as shown by the MPSH analysis for the  $\text{C}_{28}$  sensor, for both the sensors. Indeed, the  $\text{O}_2$  molecule does not show a spontaneous dipole moment, as it is not a polar molecule, but also considering the possibility of having an induced dipole moment, its extension could not justify the strong variations at high voltages. In fact, if that possibility is taken into account, a similar variation should be present also for the  $\text{N}_2$  molecule, which however does not lead to similar variations, especially for the  $\text{C}_{28}$  sensor.

Different is the story for the argon atom. For that target, as mentioned earlier, the interaction can only be due to Van Der Waals forces considering the complete octet of the argon species, or to the steric effect resulting from the high atomic number of argon. This suggested, for both sensors, that the interaction with high atomic number based species could lead to big modifications.

At this point, however, the two sensors behaved differently. While the interactions with pollutants provided similar variations for all the species introduced for the  $\text{C}_{28}$  sensor, for the  $\text{C}_{60}$  sensor the hypothesis of having good selectivity with respect to high atomic number targets seems to be confirmed. Again, this difference, assuming that fullerene based sensor may behave in a similar manner, is justified

by the higher reactivity of the  $C_{28}$ , where the presence of unpaired electrons may lead to intermediate interaction between physisorption and chemisorption, thus leading to essentially no differences between the pollutants.

There are however similitudes between the sensors. Firstly, there is a strong dependence on the applied bias, with variations that are unpredictable, even for the same species. Then, and this probably represents the most critical property, the position and the orientation at which the external species are placed nearby the sensors play a crucial role in determining the effect on the  $I(V)$  curve, meaning that, although for a certain species the selectivity has been verified either for the  $C_{28}$  or for the  $C_{60}$  sensor, it is not said that similar variations may occur for other species with positions not considered in this work or in the  $C_{60}$  one. This result has to be carefully considered for the future development of molecule based sensors.

## Chapter 8

# Conclusions and recommendations

To conclude the work, in this final chapter the procedure and the main results of the whole thesis project are summarized, in order to discuss the findings and provide possible ideas for future works related to the considered argument.

### 8.1 Conclusions

The goal of the study conducted was to create and analyze a molecule based system, and in particular a gas sensor, from the theoretical standpoint.

Firstly, before proceeding with the core of the thesis, the importance and the characteristics of this particular class of devices have been described, to show why their research and development may be of interest in the future. This allowed to further justify the choice of focusing on a sensor, where the technological reliability is not expected to be a limiting factor for its practical implementation. The desired properties of sensors have also been introduced, to understand how the final device should have behaved.

After this introduction an approximated and very simple theoretical model has been presented, with the purpose of establishing some of the primary concepts behind the electronic structure and transport properties of molecular systems. These concepts have then been deeply discussed in the successive chapters, to validate the choices made for the simulations settings of the practical parts of the work, where semi-empirical methods, like EHT and Slater-Koster, and the more precise DFT model, have been used.

Moving to the results obtained, the first step conducted regarded the research of possible configurations for the system, in order to find those structures which are expected to be stabler and hence more probable to occur. This part of the work is

of particular interest, both for understanding the general complexity at the core of the technologies employed for the realization of molecular structure, but also, and especially, for the systematic approach used, which represents a novelty for the employed  $C_{28}$  molecule, which use in literature is restricted to few structures usually intended to work as transistors. Very different configurations involving the two isomers of the  $C_{28}$ , with various orientations of the fullerene as well as distances between the electrodes, have been studied in terms of stability, allowing to find some potential candidates for the final device, among which one was chosen and fixed.

At that point, the resulting gold- $C_{28}$  molecular junction has been analyzed in an equilibrium condition, in order to verify the validity of the EHT method over the DFT one, but also to have a preliminary check of the reactivity of the sensor, i.e. to analyze whether the system could detect the presence of other species or not. Indeed, since sensors exploiting this molecule have not been found in literature, it was not said that the  $C_{28}$  could be used for sensing purposes. Subsequently, the system has been brought out of equilibrium in the presence of free air species, providing a certain modification of its properties, with variations pointing towards the ability of the sensor of reacting with a certain selectivity to high atomic number species.

Unfortunately, a further analysis on the interaction with chosen pollutants did not verify this possibility, essentially leading to a failure in the sensor, which, although providing a certain selectivity for some pollutants at specific applied voltages, does not seem able to detect a determined class of targets. Considering the uniqueness of the created sensor, it has not been possible to check whether this could be a problem related to the chosen structure, to the positions at which the pollutants were placed, or a general characteristic of the employed fullerene.

The only comparison which could be performed has been made between the developed sensor and a similar fullerene  $C_{60}$  sensor. While the general characteristics of the two devices seemed comparable for free air species, however the reactivity of the smaller fullerene made not possible the detection of species with high induced or permanent polarization moments, differently from the provided sensor. Nevertheless, this comparison also showed an important similarity, that is the strong dependence of the current variations on the applied bias and on the positions at which the targets were placed.

## **8.2 Future works**

Considering the discussed results and the inevitable limitations of the work, both in terms of time and raw power of the machine employed, the purpose of this final section is to present a series of possible analysis and studies which may be done

on the proposed structure or that can be interesting in general for molecule based systems.

First of all, the systematic analysis of  $C_{28}$  based structures employing gold as material for the contacts and the evidence of some possible stable configurations different with respect to the chosen one allows to have a series of geometries which can be independently studied to verify whether the inability of the sensor could be associated to the employed configuration or the fullerene itself. Furthermore, while the presence of a gate contact should not lead to considerably different results, a study on its effect on the  $I(V)$  characteristic may reveal the selectivity with respect to a certain target. Moreover, as it represents a primary component of transistors, its introduction may be of interest for the creation of a system of this kind, instead of forcing it to work as a sensor.

Regarding the structures studied, the choice of gold has been enforced since the beginning. A possible area of study concerning the same molecule therefore consists in analyzing the differences caused by the choice of other materials for the contacts, maybe using copper or silver.

Another interesting and maybe game changing investigation which can be performed involves the methodical study of adsorption of targets on the fullerene. Indeed, through the entire work the positions at which the external molecules have been placed were enforced. It is however not said that the species may place themselves in those positions to begin with and so it is reasonable that the polarity of the molecules may force them to approach the fullerene with a specific orientation, thus leading to a valuable sensor for the detection of highly polar molecules. This type of analysis is of course not limited to the system of this work but can be extended to all molecule based sensor.

Finally, due to time constraints it has not been possible to study the effect of multiple molecules placed nearby the sensor. In fact, cases of this kind may completely disregard not only the  $C_{28}$ , but also the  $C_{60}$  sensor from being valuable. The interaction with two oxygen molecules at the same time, for example, or with one nitrogen molecule and one water molecule, may cause variations similar to the desired target. In that sense the requirement of having a portion of the sensing region being reactive only with the chosen target may be mandatory.



# Appendix A

## Additional design pictures

This part of the appendix is devoted to all the additional graphs related to chapter 5.

First of all, in figure A.1 the constraints applied during the geometry relaxation simulations are specified, both for the configurations involving an adatom and those not employing it. In figure A.2, instead, the location and distance of the gold adatom for those configurations requiring it is provided. As said in chapter 5, two different cases have been considered.

Then, in section A.1, all the geometries and information associated to the  $D_2$  symmetry not reported in chapter 5 are present.

Finally, in section A.2, the same is done for the  $T_d$  symmetry. For specific details refer to captions.

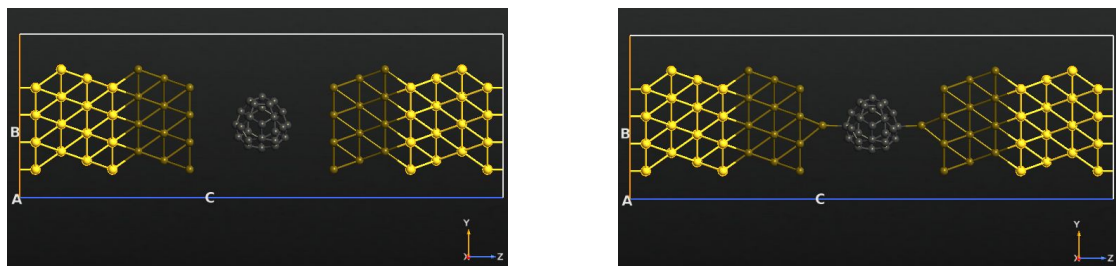


**Figure A.1:** Constraints applied during relaxation for all devices in absence of an adatom (left) and in the presence of it (right). The highlighted layers are fixed whereas the others are free to move. Notice that the adatom is free to move as well.

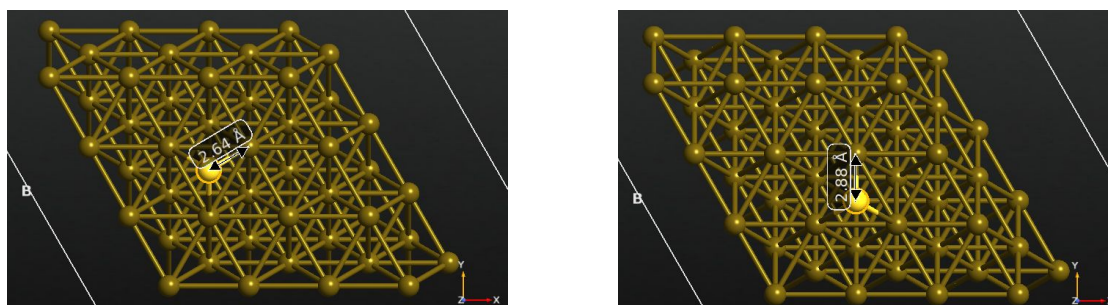


**Figure A.2:** Position of the gold adatom for the configurations requiring it (the highlighted atom is the adatom, whereas the others belong to the underlying layers).

### A.1 $D_2$ symmetry additional graphs

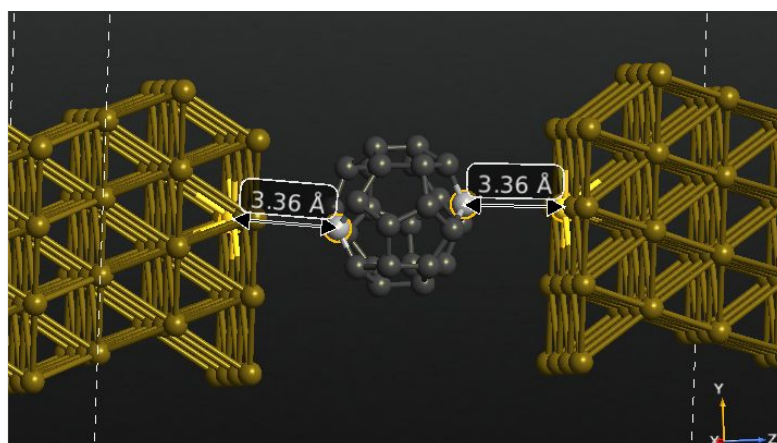


**Figure A.3:** Distance between the fullerene and the contacts for the  $D_2$  symmetry configuration of figure 5.3.

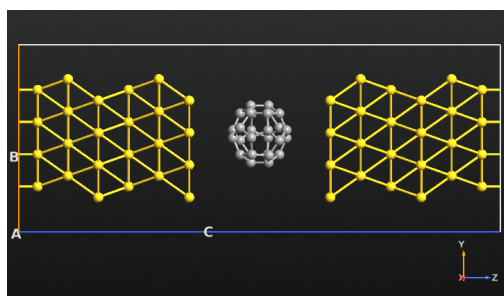


**Figure A.4:** Initial geometry with distance of 3.46 Å.

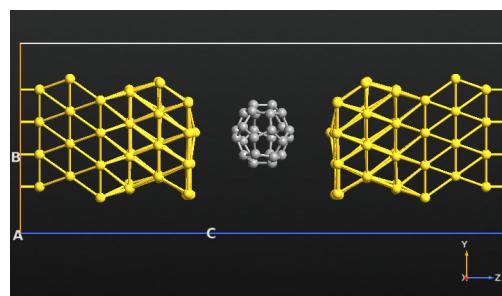


**Figure A.5:** Final geometry.

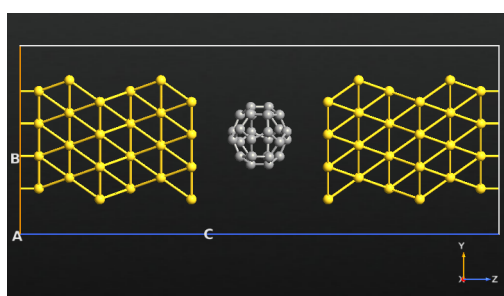


**Figure A.6:** Initial structure with distance of 3.26 Å.

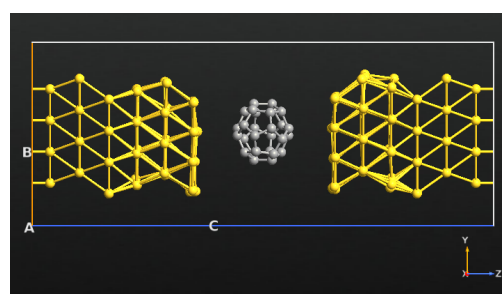


**Figure A.7:** Geometry after relaxation.

**Figure A.8:** These configurations are equal to the one of figure 5.3, but with different distances. None of them is expected to be stabler.

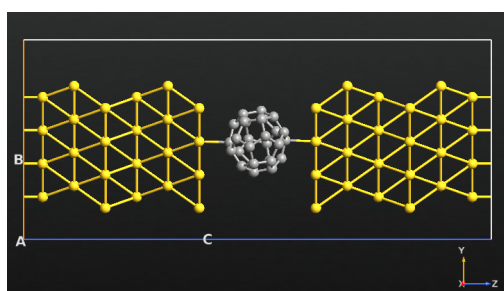


**Figure A.9:** Initial configuration with the fullerene placed at 2.31 Å from the gold contacts.

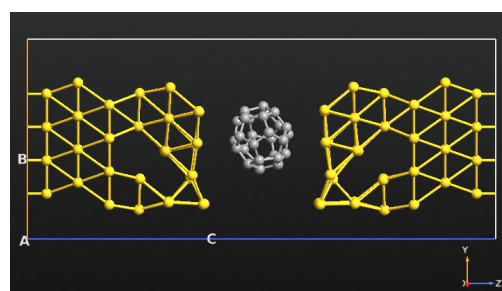


**Figure A.10:** Configuration after relaxation occurred. Notice the extreme deformation of the contacts.

## A.2 $T_d$ symmetry additional graphs

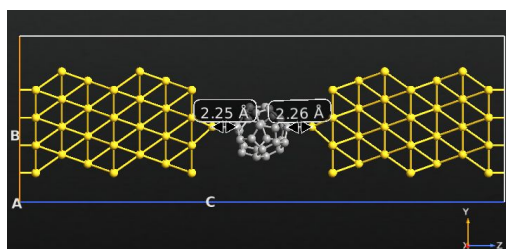
Additional  $T_d$  graphs are here reported. In particular, figure A.15 gives additional information about figure 5.14.

Figure A.22 includes initial and final configurations for the *MJ1* structure not inserted in chapter 5, with all the details about distances and deformations.

Then, figure A.27 reports the *MJ2* structure not inserted in 5 whereas figure A.28 is about the distances for figure 5.16.

Moving on to figure A.29, this is related to the *MJ3* structure analyzed and not reported in chapter 5. In fact, as shown in figure A.30, strong deformation occurred, thus rejecting it to be a possible stable configuration.

Finally, in figure A.31, the MPSH analysis performed on the chosen structure is reported.



**Figure A.11:** Starting Au-C bond length.

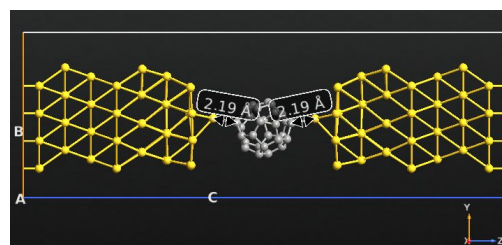


**Figure A.12:** Final Au-C bond length. Little deformation occurred in the distance.

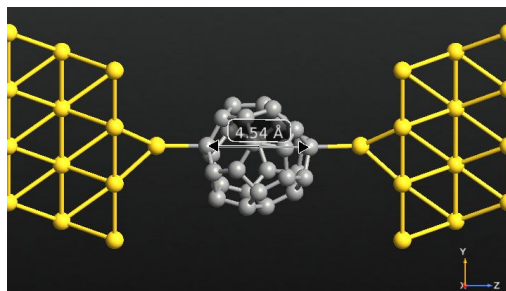


**Figure A.13:** Initial extension of the fullerene.

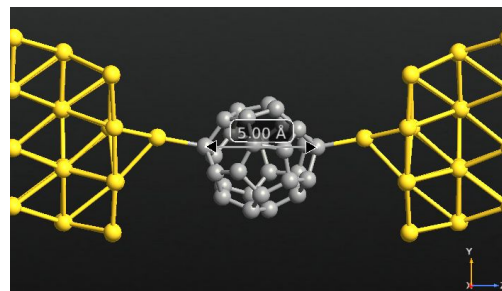


**Figure A.14:** Final fullerene extension.

**Figure A.15:** Second *MJ1* configuration (it is the one of figure 5.14). This is not expected to be a stable configuration.

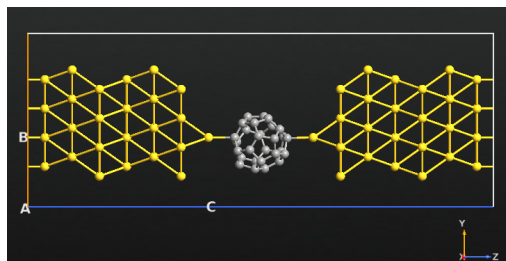


**Figure A.16:** Starting configuration for the *MJ1* system.

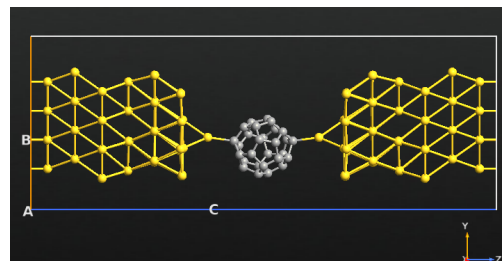


**Figure A.17:** Structure at the end of the relaxation process.

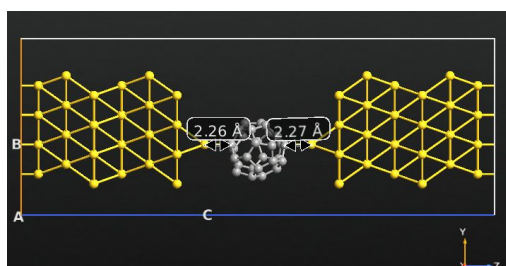


**Figure A.18:** Starting Au-C bond length.

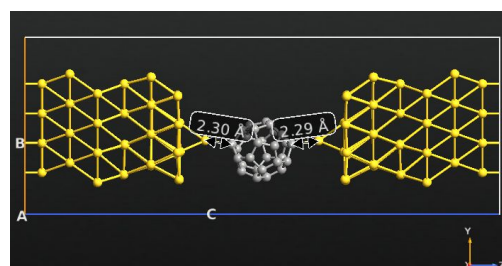


**Figure A.19:** Final bond length. Little deformation occurred in the distance.

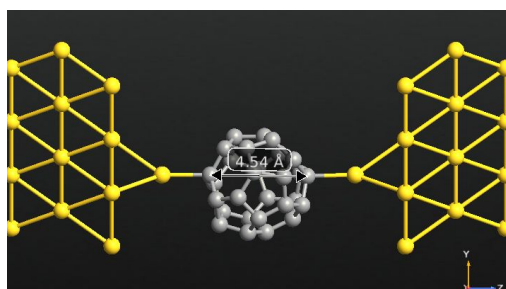


**Figure A.20:** Initial extension of the fullerene.

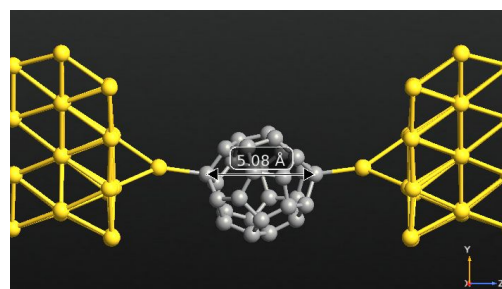


**Figure A.21:** Final fullerene extension.

**Figure A.22:** First *MJ1* configuration. This is not expected to be a stable configuration, due to the great elongation of the fullerene.

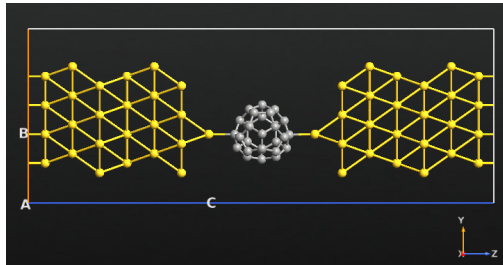


**Figure A.23:** Starting configuration for the system.

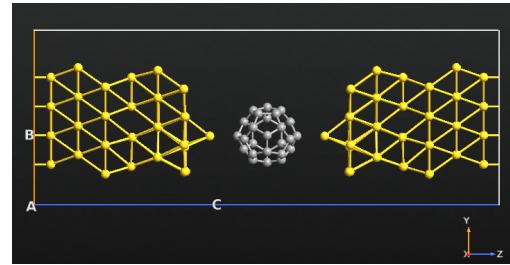


**Figure A.24:** Structure at the end of the relaxation process.

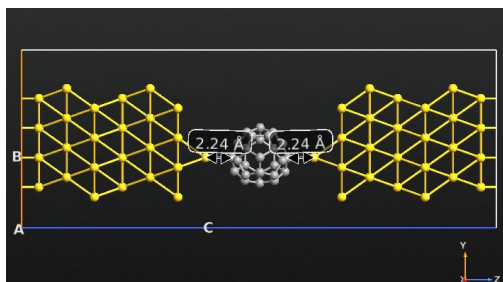


**Figure A.25:** Initial distance between carbon and gold atoms, set at 2.24 Å.

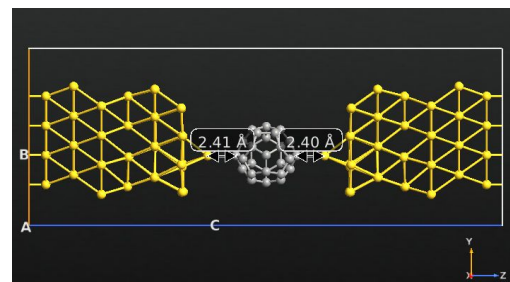


**Figure A.26:** The optimized structure suggests an Au-C bonding distance in the order of 10% bigger than the initial one.

**Figure A.27:** First *MJ2* configuration. This is not expected to be stabler than the one of chapter 5.

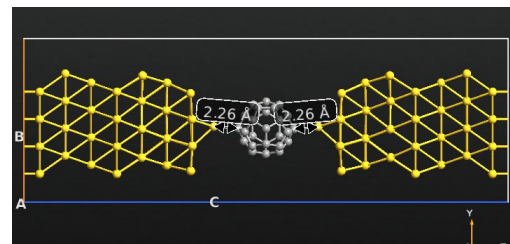
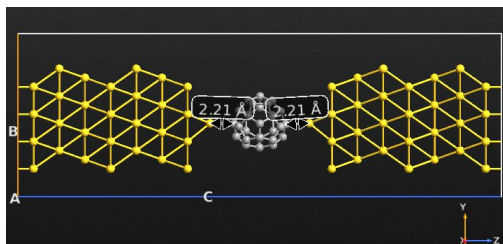


**Figure A.28:** Au-C distance in the initial configuration (left) and in the final one (right) for the second *MJ2* (the one of figure 5.16).

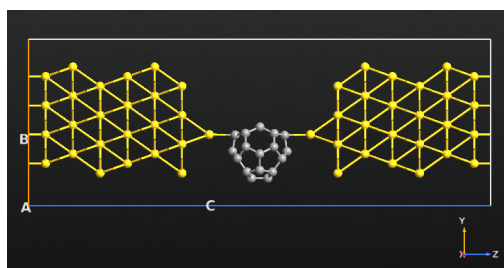


**Figure A.29:** *MJ3* junction initial configuration.

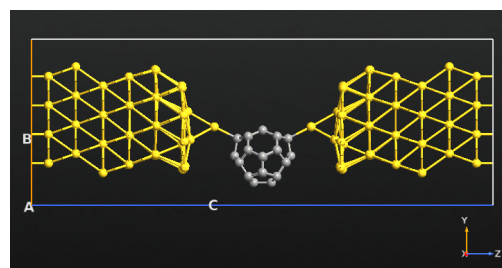


**Figure A.30:** Final configuration after relaxation.

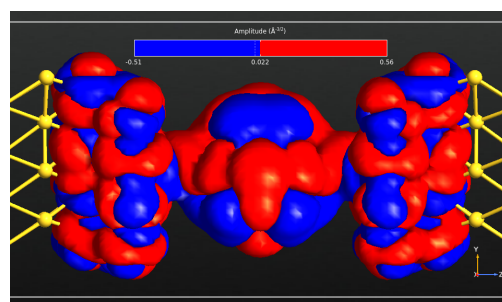
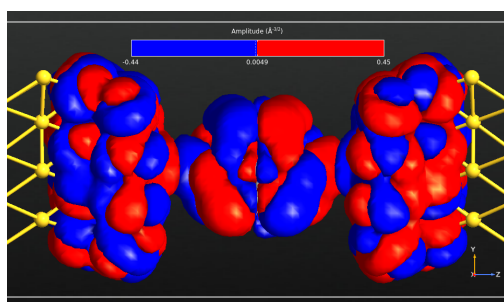


**Figure A.31:** MPSH analysis of the chosen structure (see figure 5.16) on the first HOSO level (left) and LUSO level (right). A good delocalization is present.

## Appendix B

# Additional free air analysis pictures

This part is devoted to additional graphs related to chapter 3 and 6.

More precisely, in section B.1 the comparison of tools performances introduced and described in section 3.3 is reported.

Then, the Mulliken population of the fullerene alone as evaluated by means of different methods in order to validate Slater-Koster results is shown in section B.2. Finally, the Van Der Waals spheres described in chapter 6, the distances of external species in the case of free air molecules and the variations in the DOS and the transmission spectrum between DFT, EHT and Slater-Koster considering each external molecule alone are reported in section B.3.

### B.1 DFT settings quick comparison

Starting with the comparison between results given by the various settings for the DFT calculations, in figures B.1 and B.2, the density of states and the transmission spectrum are evaluated by means of the D2 and D3 Van Der Waals corrections for the sensor in the presence of an oxygen molecule (there is not a particular reason for which this particular molecule has been used as it is expected that, if no difference is present, this would be the case of most of the molecules analyzed).

Since the curves are very close one to the other and since the D3 correction is more computationally involving, D2 correction has been used in the rest of simulations. Notice that, for both the DOS and the TS the rest of the calculator block has been kept equal. In particular, GGA-PBE, with FHI pseudopotential and DoubleZetaPolarized basis set has been used.

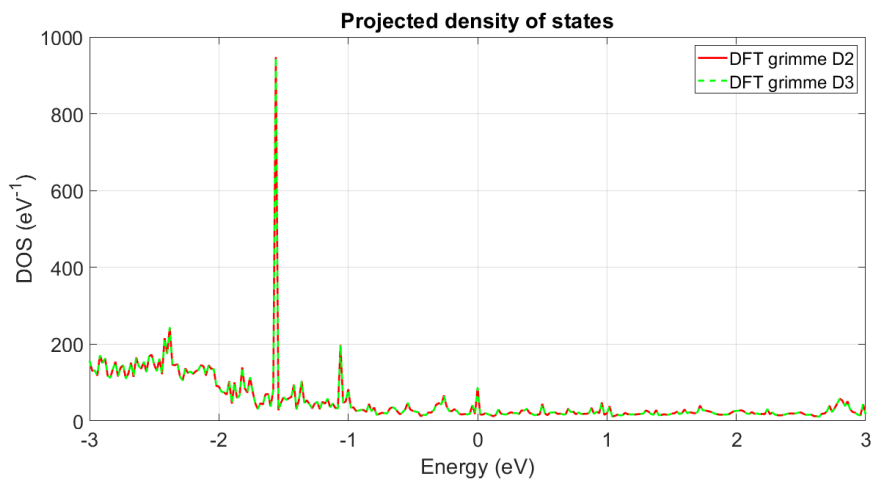


**Figure B.1:** Comparison of the density of states. The analysis is performed with the sensor in presence of O<sub>2</sub> molecule, to simulate the presence of Van Der waals interaction.

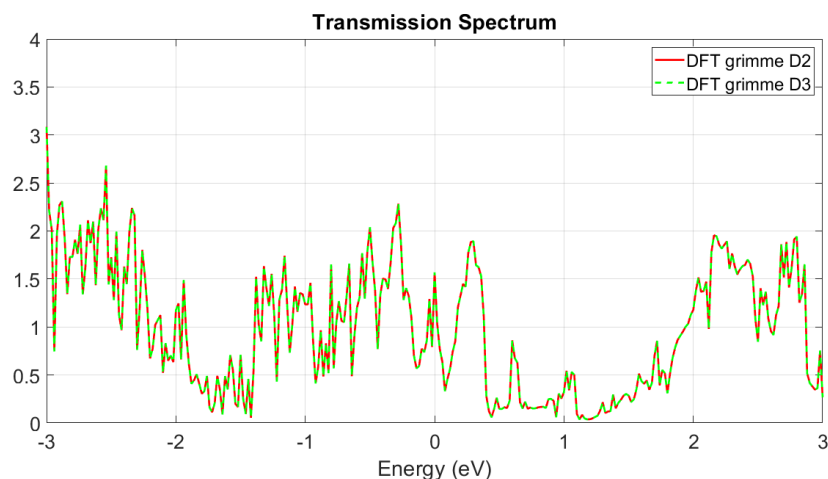


**Figure B.2:** Comparison of the transmission spectrum. The analysis is performed with the sensor in presence of O<sub>2</sub>.

## B.2 Mulliken population

Mulliken population studies employing different tools and basis sets are reported here for the fullerene alone to verify the effectiveness of such analysis. Although small variations are present in the effective amount of charge, they all agree on the

general behavior of all the atoms.

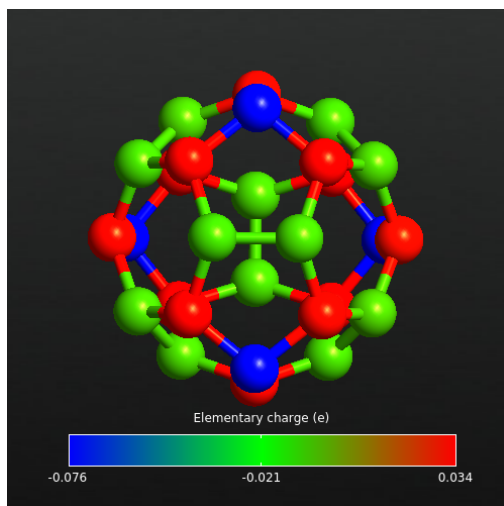


**Figure B.3:** Mulliken population analysis with GGA-BLYP functional, PseudoDojo pseudopotential and Ultra basis set settings.

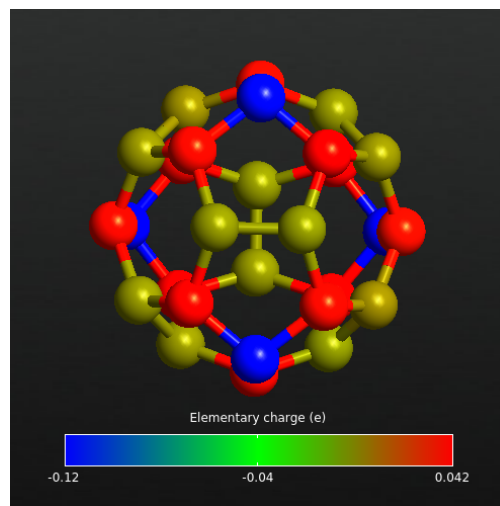


**Figure B.4:** Mulliken population analysis with GGA-BLYP functional, FHI pseudopotential and DZP basis set settings.

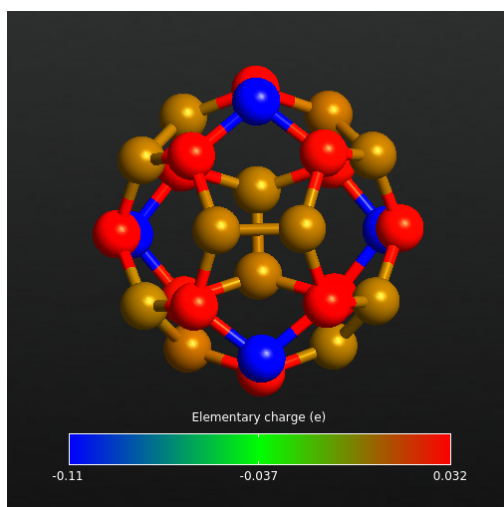


**Figure B.5:** Mulliken population analysis with HGGA functional, PseudoDojo pseudopotential and Ultra basis set settings.

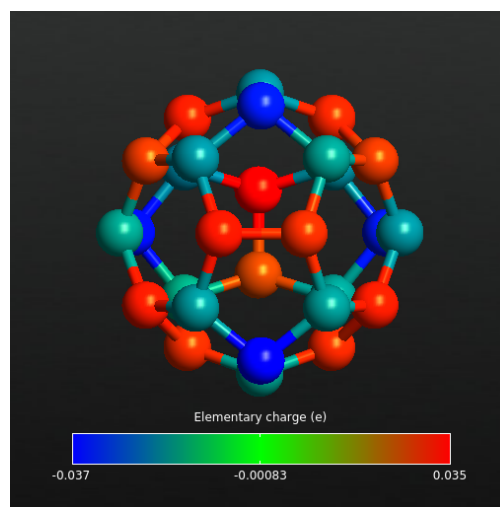


**Figure B.6:** Mulliken population analysis as evaluated by Slater-Koster. The result is compatible with the others.

## B.3 Free air additional graphs

### B.3.1 Van Der Waals spheres

As mentioned in chapter 6, the external molecules have been placed in order to ensure the overlapping of the Van Der Waals spheres of the carbon atoms related to the fullerene with the ones of interacting species.

In figure B.7, a schematic representation of the pentagon made of carbon atoms at the top of the fullerene (the one closer to the external species) is reported, giving an indication of what the distances reported in tables B.1, B.2, B.3, B.4, and B.5 refer to.

Instead, in figure B.14, all the molecules usually found in atmosphere are considered with their own Van Der Waals spheres.

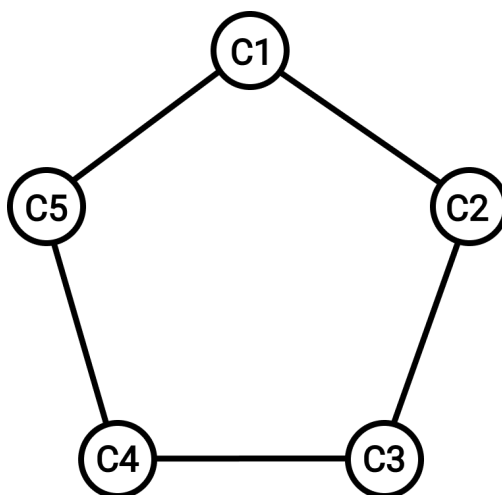


**Figure B.7:** Schematic of the carbon atoms pentagon.

**Table B.1:** Distance of Ar with respect to the carbon atoms of figure B.7.

	Argon
<b>C1</b>	2.32 Å
<b>C2</b>	2.49 Å
<b>C3</b>	2.57 Å
<b>C4</b>	2.59 Å
<b>C5</b>	2.52 Å

**Table B.2:** Distance of CO<sub>2</sub> with respect to the carbon atoms of figure B.7.

	Carbon	Oxygen	Oxygen
<b>C1</b>	2.10 Å	2.13 Å	2.69 Å
<b>C2</b>	2.49 Å	2.91 Å	2.63 Å
<b>C3</b>	2.82 Å	3.67 Å	2.32 Å
<b>C4</b>	2.81 Å	3.67 Å	2.31 Å
<b>C5</b>	2.48 Å	2.89 Å	2.62 Å

**Table B.3:** Distance of O<sub>2</sub> with respect to the carbon atoms of figure B.7.

	Oxygen	Oxygen
<b>C1</b>	2.10 Å	2.86 Å
<b>C2</b>	2.19 Å	2.63 Å
<b>C3</b>	2.25 Å	2.11 Å
<b>C4</b>	2.32 Å	2.18 Å
<b>C5</b>	2.29 Å	2.71 Å

**Table B.4:** Distance of N<sub>2</sub> with respect to the carbon atoms of figure B.7.

	Nitrogen	Nitrogen
<b>C1</b>	2.09 Å	2.64 Å
<b>C2</b>	2.38 Å	2.55 Å
<b>C3</b>	2.68 Å	2.27 Å
<b>C4</b>	2.73 Å	2.33 Å
<b>C5</b>	2.47 Å	2.63 Å

**Table B.5:** Distance of H<sub>2</sub>O (O down) relative to the carbon atoms of figure B.7.

	Oxygen	Hydrogen	Hydrogen
<b>C1</b>	2.15 Å	2.30 Å	3.07 Å
<b>C2</b>	2.31 Å	2.77 Å	3.01 Å
<b>C3</b>	2.37 Å	3.20 Å	2.69 Å
<b>C4</b>	2.37 Å	3.20 Å	2.68 Å
<b>C5</b>	2.31 Å	2.77 Å	3.01 Å

**Table B.6:** Distance of H<sub>2</sub>O (O up) relative to the carbon atoms of figure B.7.

	Oxygen	Hydrogen	Hydrogen
<b>C1</b>	2.96 Å	2.15 Å	3.06 Å
<b>C2</b>	3.06 Å	2.52 Å	2.88 Å
<b>C3</b>	2.97 Å	2.84 Å	2.36 Å
<b>C4</b>	2.97 Å	2.84 Å	2.36 Å
<b>C5</b>	3.06 Å	2.52 Å	2.88 Å

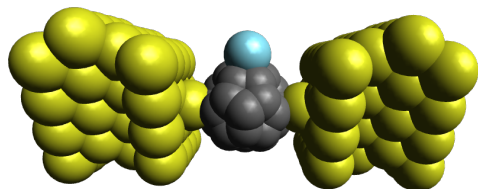


**Figure B.8:** Sensor in the presence of Argon (cyan sphere).

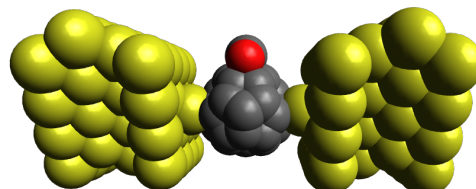


**Figure B.9:** Sensor in the presence of  $\text{CO}_2$  (the red spheres are related to oxygen atoms).

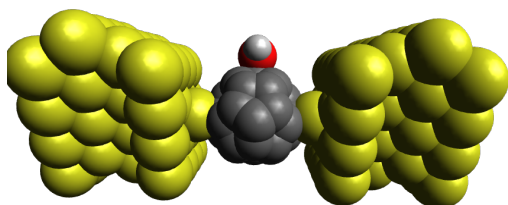


**Figure B.10:** Sensor in the presence of water vapor (hydrogen in light gray, oxygen in red). Notice that the O atom is placed down, whereas hydrogen is up.

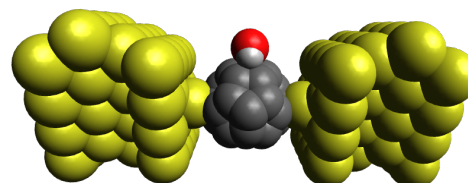


**Figure B.11:** Sensor in the presence of water vapor (hydrogen in light gray, oxygen in red). Notice that the O atom is placed up, whereas hydrogen is down.

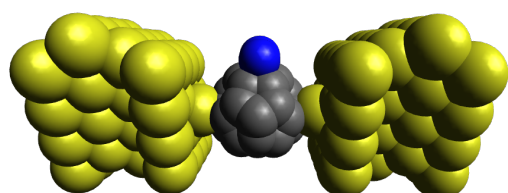


**Figure B.12:** Sensor in the presence of  $\text{N}_2$  (blue spheres).

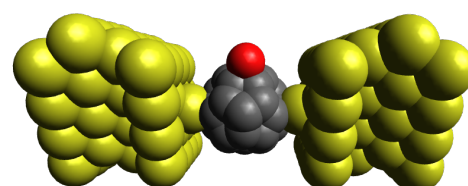


**Figure B.13:** Sensor in the presence of  $\text{O}_2$ .

**Figure B.14:** Graphical representation of the Van Der waals spheres.

### B.3.2 TS and DOS

In this section additional comparisons between the various calculation tools are reported. In particular, in figure B.15 the DOS for each molecule taken singularly are shown, whereas in figure B.16 the same is done for the transmission spectrum.

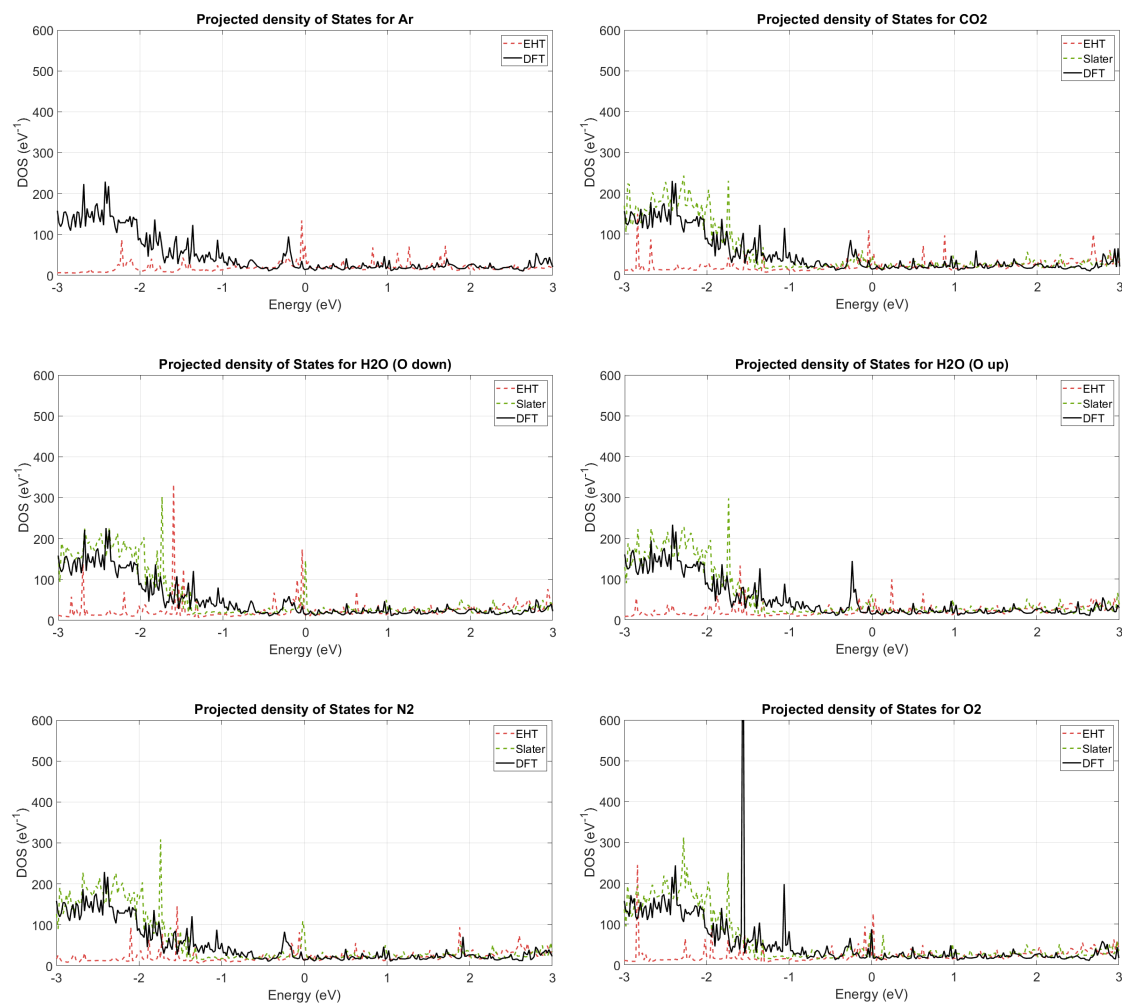


**Figure B.15:** Comparison of the DOS evaluated by DFT, EHT and Slater-Koster in the presence of external species nearby the sensor. From top left to bottom right: Ar, CO<sub>2</sub>, H<sub>2</sub>O (O down), H<sub>2</sub>O (O up), N<sub>2</sub>, O<sub>2</sub>.

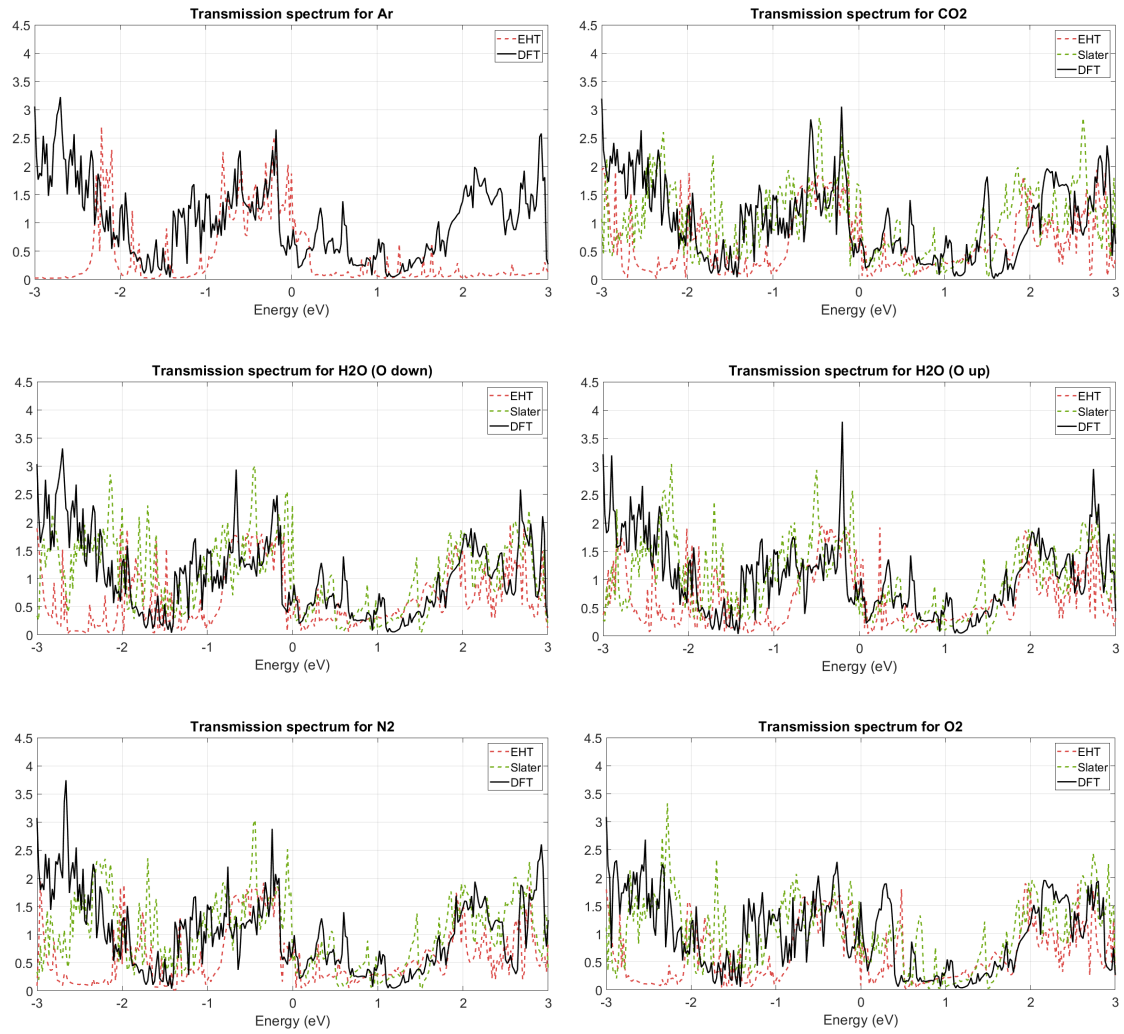


**Figure B.16:** Comparison of the TS evaluated by DFT, EHT and Slater-Koster in the presence of external species nearby the sensor. From top left to bottom right: Ar, CO<sub>2</sub>, H<sub>2</sub>O (O down), H<sub>2</sub>O (O up), N<sub>2</sub>, O<sub>2</sub>.

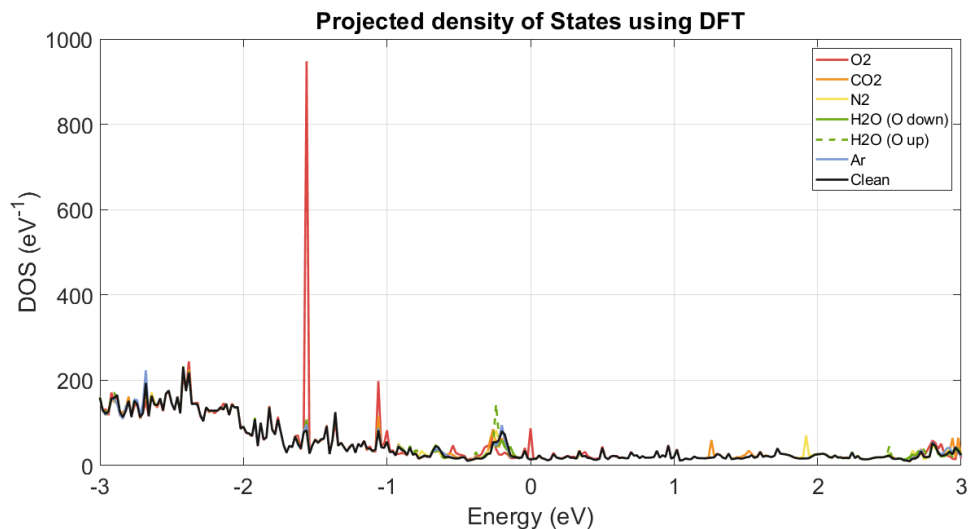


**Figure B.17:** Full picture of the free air DOS evaluated by DFT. Notice the peak in the HOSO side.

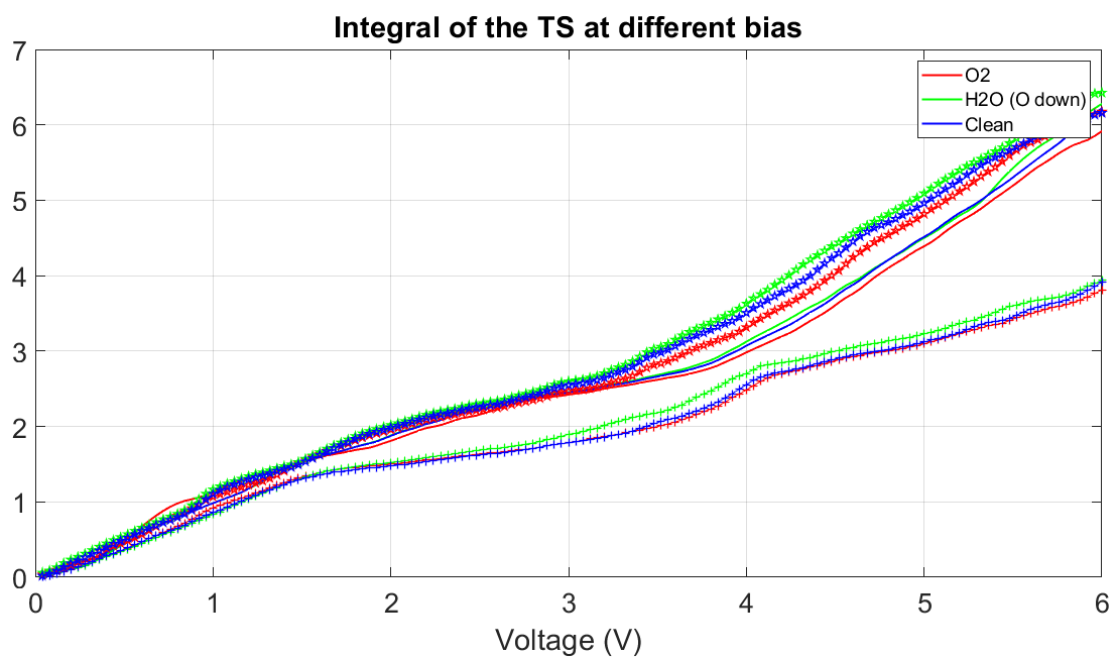


**Figure B.18:** Comparison of the integrals of the TS as evaluated by DFT (continued lines), Slater-Koster (starred lines) and EHT (marked lines). Notice the increase in variation starting from 2 V.

**Table B.7:** Average percentage difference between the integrals of the TS of DFT and EHT and Slater-Koster for 6 V of applied voltage, starting from 0.04 V.

	Slater-Koster	EHT
Clean	9.70%	23.44%
O <sub>2</sub>	8.03%	23.87%
CO <sub>2</sub>	11.12%	24.05%
N <sub>2</sub>	14.34%	21.62%
H <sub>2</sub> O (O down)	15.57%	21.46%
H <sub>2</sub> O (O up)	8.52%	21.47%
Ar		36.90%

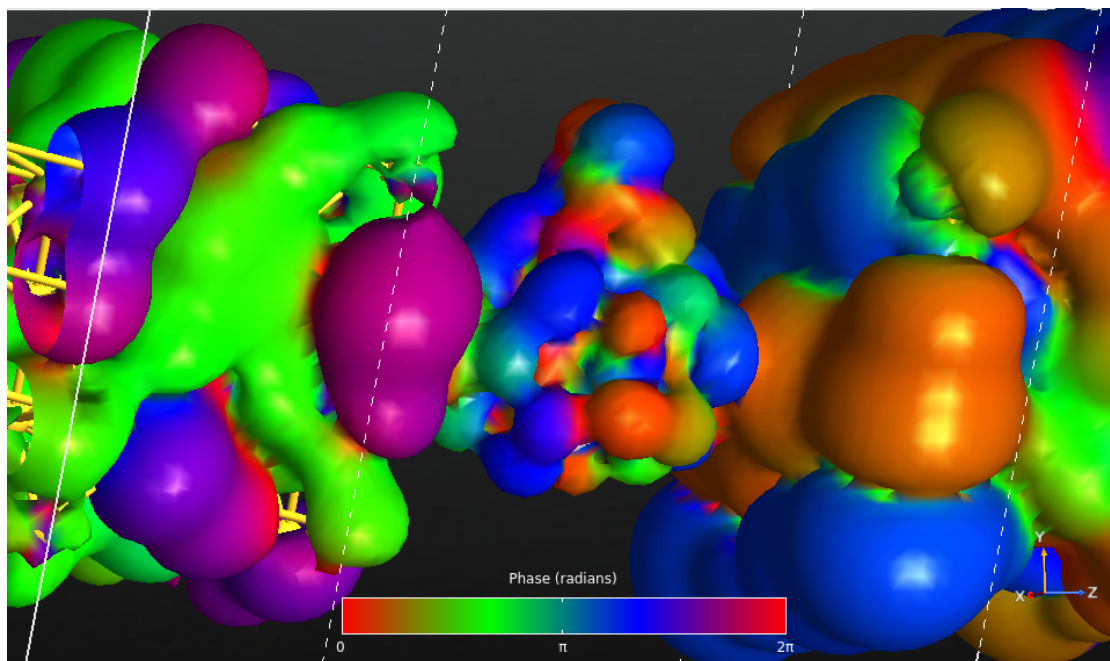


**Figure B.19:** Transmission eigenstate at 0.42 eV (zoom on the middle region of the system).

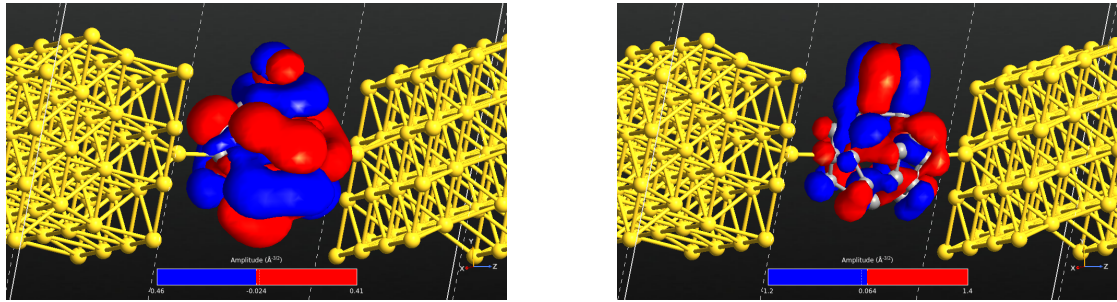


**Figure B.20:** MPSH for the HOSO state (left) and for the LUSO (right) for the fullerene in the presence of oxygen. Notice how the transmission eigenstate reported in figure B.19 closely resembles the HOSO level of the system.

# Appendix C

## Additional pollutants analysis information

This part of the appendix includes additional information on the configurations involving pollutants species.

### C.1 Positions of pollutants

In this section the positions at which the various pollutants have been placed for out of equilibrium studies are provided.

As far as hydrocarbons with a high number of atoms, like  $C_6H_6$ ,  $C_7H_8$  and  $C_8H_{10}$ , in order to provide the various distances in an understandable yet meaningful way, only the distances of a couple of atoms are provided.

The atoms for which the distances are reported are the ones highlighted in the figures of the various configurations, shown in C.1, C.2 and C.3.

Using the distances and the images it should be straightforward to retrieve the same structures. Further details are given in the captions.

**Table C.1:** Distance of CO with respect to the carbon atoms of figure B.7, in the case of oxygen pointing downwards.

	Carbon	Oxygen
<b>C1</b>	3.66 Å	2.13 Å
<b>C2</b>	3.77 Å	2.36 Å
<b>C3</b>	3.73 Å	2.59 Å
<b>C4</b>	3.76 Å	2.65 Å
<b>C5</b>	3.82 Å	2.46 Å

**Table C.2:** Distance of CO with respect to the carbon atoms of figure B.7, in the case of oxygen pointing upwards.

	<b>Carbon</b>	<b>Oxygen</b>
<b>C1</b>	2.13 Å	3.66 Å
<b>C2</b>	2.36 Å	3.77 Å
<b>C3</b>	2.59 Å	3.73 Å
<b>C4</b>	2.65 Å	3.76 Å
<b>C5</b>	2.46 Å	3.82 Å

**Table C.3:** Distance of NO with respect to the carbon atoms of figure B.7, in the case of nitrogen pointing downwards.

	<b>Nitrogen</b>	<b>Oxygen</b>
<b>C1</b>	2.14 Å	3.33 Å
<b>C2</b>	2.41 Å	3.55 Å
<b>C3</b>	2.69 Å	3.69 Å
<b>C4</b>	2.74 Å	3.72 Å
<b>C5</b>	2.50 Å	3.61 Å

**Table C.4:** Distance of NO with respect to the carbon atoms of figure B.7, in the case of nitrogen pointing upwards.

	Nitrogen	Oxygen
<b>C1</b>	3.33 Å	2.14 Å
<b>C2</b>	3.55 Å	2.41 Å
<b>C3</b>	3.69 Å	2.69 Å
<b>C4</b>	3.72 Å	2.74 Å
<b>C5</b>	3.61 Å	2.50 Å

**Table C.5:** Distance of NO<sub>2</sub> with respect to the carbon atoms of figure B.7, in the case of nitrogen pointing upwards.

	Nitrogen	Oxygen	Oxygen
<b>C1</b>	3.09 Å	2.11 Å	3.33 Å
<b>C2</b>	3.03 Å	2.42 Å	2.95 Å
<b>C3</b>	2.78 Å	2.73 Å	2.14 Å
<b>C4</b>	2.83 Å	2.78 Å	2.21 Å
<b>C5</b>	3.10 Å	2.51 Å	3.03 Å

**Table C.6:** Distance of NO<sub>2</sub> with respect to the carbon atoms of figure B.7, in the case of nitrogen pointing downwards.

	Nitrogen	Oxygen	Oxygen
<b>C1</b>	2.19 Å	2.45 Å	3.32 Å
<b>C2</b>	2.21 Å	2.85 Å	3.07 Å
<b>C3</b>	2.17 Å	3.25 Å	2.48 Å
<b>C4</b>	2.23 Å	3.29 Å	2.54 Å
<b>C5</b>	2.31 Å	2.92 Å	3.14 Å

**Table C.7:** Distance of CH<sub>4</sub> with respect to the carbon atoms of figure B.7.

	Carbon	Hydrogen	Hydrogen	Hydrogen	Hydrogen
<b>C1</b>	3.24 Å	2.20 Å	3.66 Å	3.94 Å	3.59 Å
<b>C2</b>	3.53 Å	2.54 Å	3.68 Å	4.09 Å	4.22 Å
<b>C3</b>	3.76 Å	2.83 Å	4.07 Å	3.95 Å	4.60 Å
<b>C4</b>	3.79 Å	2.83 Å	4.44 Å	3.86 Å	4.43 Å
<b>C5</b>	3.58 Å	2.55 Å	4.30 Å	3.96 Å	3.93 Å

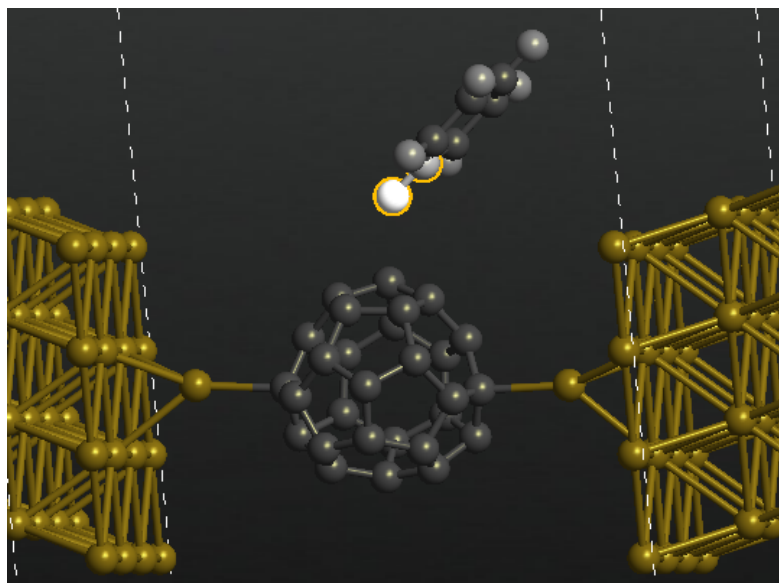


**Figure C.1:** Sensor in the presence of  $C_6H_6$  (zoom in the middle region). The two highlighted atoms are the ones which distances are provided.

**Table C.8:** Distance of the highlighted atoms of figure C.1 (related to  $C_6H_6$ ) with respect to the carbon atoms of figure B.7.

	Hydrogen	Carbon
<b>C1</b>	2.13 Å	3.01 Å
<b>C2</b>	3.00 Å	3.54 Å
<b>C3</b>	3.87 Å	4.41 Å
<b>C4</b>	3.86 Å	4.64 Å
<b>C5</b>	2.99 Å	3.97 Å

**Table C.9:** Distance of the highlighted atoms of figure C.2 (related to  $C_7H_8$ ) with respect to the carbon atoms of figure B.7.

	Hydrogen	Carbon
<b>C1</b>	2.11 Å	2.97 Å
<b>C2</b>	2.64 Å	3.21 Å
<b>C3</b>	3.10 Å	2.73 Å
<b>C4</b>	3.07 Å	3.98 Å
<b>C5</b>	2.59 Å	3.65 Å

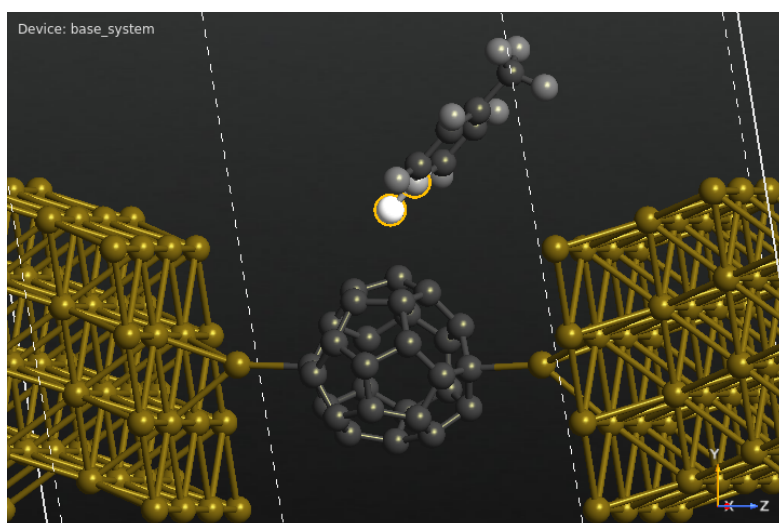


**Figure C.2:** Sensor in the presence of C<sub>7</sub>H<sub>8</sub> (zoom in the middle region). The two highlighted atoms are the ones which distances are provided.

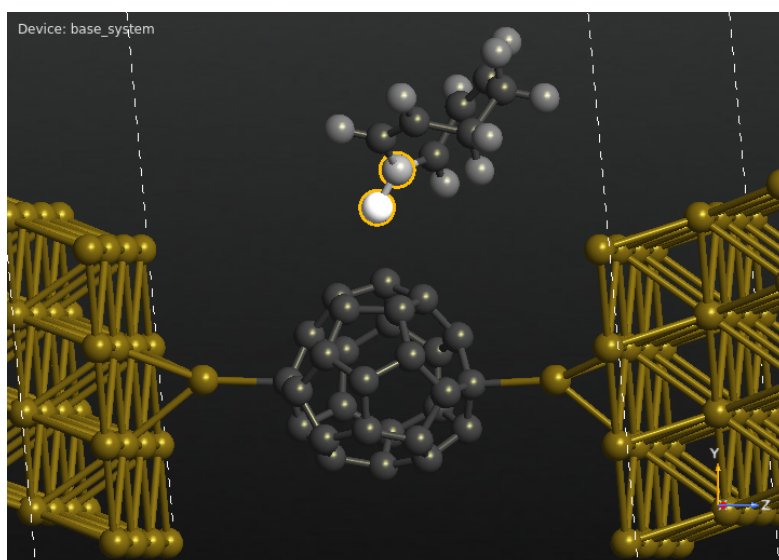


**Figure C.3:** Sensor in the presence of C<sub>8</sub>H<sub>10</sub> (zoom in the middle region). The two highlighted atoms are the ones which distances are provided.

**Table C.10:** Distance of the highlighted atoms of figure C.3 (related to  $C_8H_{10}$ ) with respect to the carbon atoms of figure B.7.

	<b>Hydrogen</b>	<b>Carbon</b>
<b>C1</b>	2.09 Å	2.99 Å
<b>C2</b>	3.13 Å	3.75 Å
<b>C3</b>	4.01 Å	4.61 Å
<b>C4</b>	3.89 Å	4.66 Å
<b>C5</b>	2.88 Å	3.84 Å

**Table C.11:** Distance of PbO with respect to the carbon atoms of figure B.7, in the case of lead pointing down. Notice that the distance of lead is bigger than the one usually employed as its Van der Waals radius is bigger.

	<b>Lead</b>	<b>Oxygen</b>
<b>C1</b>	2.42 Å	4.78 Å
<b>C2</b>	2.72 Å	4.93 Å
<b>C3</b>	2.94 Å	4.87 Å
<b>C4</b>	2.94 Å	4.87 Å
<b>C5</b>	2.74 Å	4.92 Å

**Table C.12:** Distance of PbO with respect to the carbon atoms of figure B.7, in the case of lead pointing up.

	<b>Lead</b>	<b>Oxygen</b>
<b>C1</b>	4.52 Å	2.17 Å
<b>C2</b>	4.66 Å	2.46 Å
<b>C3</b>	4.58 Å	2.67 Å
<b>C4</b>	4.57 Å	3.67 Å
<b>C5</b>	4.65 Å	2.46 Å

**Table C.13:** Distance of  $\text{PbSO}_4$  with respect to the carbon atoms of figure B.7, in the case of lead pointing down.

	Lead	Sulfur
<b>C1</b>	2.93 Å	5.83 Å
<b>C2</b>	3.07 Å	5.43 Å
<b>C3</b>	2.74 Å	5.63 Å
<b>C4</b>	2.48 Å	6.32 Å
<b>C5</b>	2.70 Å	6.50 Å

**Table C.14:** Distance of  $\text{PbSO}_4$  with respect to the carbon atoms of figure B.7, in the case of lead pointing upwards.

	Lead	Sulfur	Oxygen
<b>C1</b>	6.76 Å	3.48 Å	2.17 Å
<b>C2</b>	7.10 Å	3.83 Å	2.45 Å
<b>C3</b>	7.93 Å	4.17 Å	2.70 Å
<b>C4</b>	8.30 Å	4.22 Å	2.74 Å
<b>C5</b>	7.73 Å	3.92 Å	2.51 Å

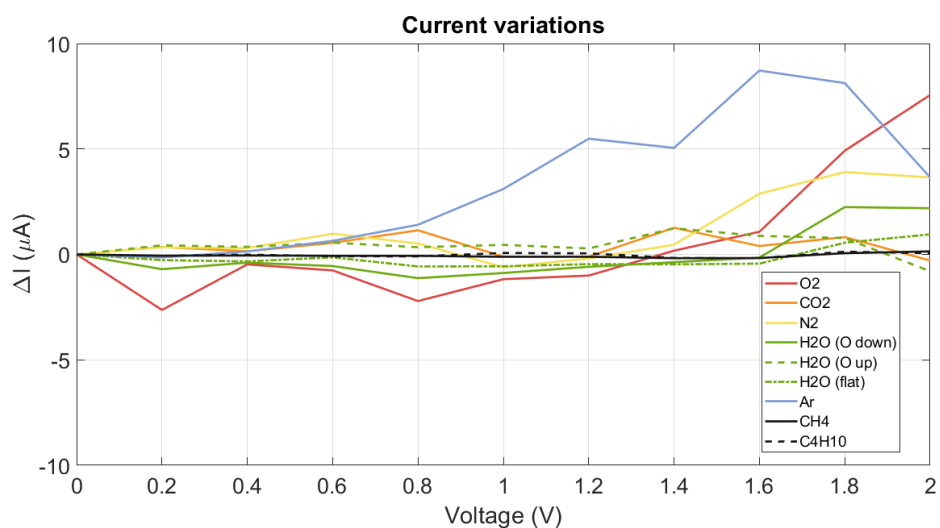


**Figure C.4:** Current variation for the  $\text{C}_{60}$  sensor in the presence of hydrocarbons (methane and butane)

# Bibliography

- [1] Jack S. Kilby. *Miniaturized Electronic Circuits*. June 1964. URL: <https://patents.google.com/patent/US3138743> (cit. on p. 1).
- [2] *The Nobel Prize in Physics 2000*. Oct. 2000. URL: <https://www.nobelprize.org/prizes/physics/2000/press-release/> (cit. on p. 1).
- [3] Gordon E. Moore. «Cramming more components onto integrated circuits». In: *Electronics*, Volume 38, Number 8 (Apr. 1965). DOI: 10.1109/N-SSC.2006.4785860 (cit. on p. 2).
- [4] Liming Xiu. «Time Moore». In: *IEEE Solid-State Circuits Magazine* (Feb. 2019), pp. 39–59. DOI: 10.1109/mssc.2018.2882285 (cit. on p. 2).
- [5] *5nm Technology*. 2020. URL: [https://www.tsmc.com/english/dedicatedFoundry/technology/logic/1\\_5nm](https://www.tsmc.com/english/dedicatedFoundry/technology/logic/1_5nm) (cit. on p. 2).
- [6] *International Roadmap For Devices And Systems - executive summary*. 2020. URL: <https://irds.ieee.org/editions/2020> (cit. on pp. 2–5).
- [7] *International Technology Roadmap For Semiconductors - executive summary*. 2005. URL: [https://www.semiconductors.org/wp-content/uploads/2018/08/20051\\_Executive-Summary.pdf](https://www.semiconductors.org/wp-content/uploads/2018/08/20051_Executive-Summary.pdf) (cit. on p. 2).
- [8] John Robertson and Robert M. Wallace. «High-K materials and metal gates for CMOS applications». In: *Materials Science and Engineering R: reports*, volume 88 (2015), pp. 1–41. DOI: 10.1016/j.mser.2014.11.001 (cit. on p. 4).
- [9] Kerim Yilmaz, Atieh Farokhnejad, Francisco Criado, Benjamín Iñíguez, François Lime, and Alexander Kloes. «Direct Source-to-Drain Tunneling Current in Ultra-Short Channel DG MOSFETs by Wavelet Transform». In: *2020 IEEE Latin America Electron Devices Conference (LAEDC) (2020)*. DOI: 10.1109/LAEDC49063.2020.9072953 (cit. on p. 4).
- [10] Hiroshi Iwai. «Future of nano CMOS technology». In: *Solid-State Electronics*, volume 112 (2015). DOI: 10.1016/j.sse.2015.02.005 (cit. on p. 4).
- [11] *International Roadmap For Devices And Systems - beyond CMOS*. 2020. URL: <https://irds.ieee.org/editions/2020> (cit. on p. 5).

- [12] Michael C. Petty. *Molecular Electronics: From Principles to Practice*. John Wiley and Sons, 2007. ISBN: 978-0-470-72389-0 (cit. on pp. 5–7).
- [13] Arieh Aviram and Mark A. Ratner. «Molecular rectifiers». In: *Chemical Physics Letters*, volume 29, issue 2 (Nov. 1974), pp. 277–283. DOI: 10.1016/0009-2614(74)85031-1 (cit. on p. 6).
- [14] Anish Mishra and Siddhesh Jagtap. «Moletronics». In: *International Journal of Scientific and Engineering Research*, Volume 7, Issue 2 (Feb. 2016), pp. 25–28 (cit. on p. 6).
- [15] Kwan S. Kwok and James C. Ellenbogen. «Molecular electronics - the future of computing». In: *Materials Today*, volume 5, issue 2 (Feb. 2002), pp. 28–37. DOI: 10.1016/S1369-7021(02)05227-6 (cit. on p. 6).
- [16] Mark Ratner. «A brief history of molecular electronics». In: *Nature Nanotechnology* volume 8 (2013), pp. 378–381. URL: <https://www.nature.com/articles/nnano.2013.110> (cit. on pp. 6–8).
- [17] C. Joachim, J. K. Gimzewski, and A. Aviram. «Electronics using hybrid-molecular and mono-molecular devices». In: *Nature* 408, pages (2000), pp. 541–548. URL: <https://www.nature.com/articles/35046000> (cit. on p. 6).
- [18] Christian Joachim, James K. Gimzewski, Reto R. Schlittler, and Corinne Chavy. «Electronic Transparency of a Single C60 Molecule». In: *Physical Review Letters* 74, number 11 (Mar. 1995), pp. 2102–2105. DOI: 10.1103/PhysRevLett.74.2102 (cit. on p. 6).
- [19] James C. Ellenbogen and J. Christopher Love. «Architectures for Molecular Electronic Computers: 1. Logic Structures and an Adder Designed from Molecular Electronic Diodes». In: *Proceedings of the IEEE*, volume 88, number 3 (Mar. 2000), pp. 386–426. DOI: 10.1109/5.838115 (cit. on p. 6).
- [20] Xu Zhang and Tao Li. «Molecular-scale electronics: From device fabrication to functionality». In: *Chinese Chemical Letters* 28, issue 11 (Nov. 2017), pp. 2058–2064. DOI: 10.1016/j.cclet.2017.09.008 (cit. on p. 7).
- [21] Tan Seng Ghee and Jalil Mays. «Nanoscale physics and electronics». In: *Introduction to the Physics of Nanoelectronics* (2012), pp. 23–77. DOI: 10.1533/9780857095886.23 (cit. on p. 7).
- [22] Nadine Gergel-Hackett, Christopher D. Zangmeister, Christina A. Hacker, Lee. J. Richter, and Curt. A. Richter. «Demonstration of Molecular Assembly on Si (100) for CMOS-Compatible Molecule-Based Electronic Devices». In: *Journal of the American Chemical Society*, volume 130, number 13 (2008), pp. 4259–4261. DOI: 10.1021/ja800378b (cit. on p. 7).
- [23] Mark A. Reed. «Molecular-Scale Electronics». In: *Proceedings Of The IEEE*, vol. 87, No. 4 (Apr. 1999), pp. 652–658 (cit. on p. 7).

- [24] Dong Xiang, Xiaolong wang, Chuancheng Jia, Takhee Lee, and Xuefung Guo. «Molecular-Scale Electronics: From concept to Function». In: *Chem. Rev.*, volume 116, number 7 (2016), pp. 4318–4440. DOI: 10.1021/acs.chemrev.5b00680 (cit. on p. 7).
- [25] Usman Yaqoob and Mohammad I. Younis. «Chemical Gas Sensors: Recent Developments, Challenges, and the Potential of Machine Learning—A Review». In: *Sensors*, volume 21, number 8, article number 2877 (2021), pp. 1–40. DOI: 10.3390/s21082877 (cit. on p. 10).
- [26] Zhang and Hoshino. «Introduction to Molecular Sensors». In: *Molecular Sensors and Nanodevices* (2019), pp. 1–42. DOI: 10.1016/B978-0-12-814862-4.00001-6 (cit. on p. 10).
- [27] Kurt Stokbro, Dan Erik Petersen, Søren Smidstrup, Anders Blom, and Mads Ipsen. «Semiempirical model for nanoscale device simulations». In: *Physical Review B* 82, issue 7 (2010), pp. 075420-1-075420-7. DOI: 10.1103/PhysRevB.82.075420 (cit. on p. 40).
- [28] David M. Hanson, Erica Harvey, Robert Sweeney, and Theresa Julia Zielinski. *Semi-Empirical Methods - Extended Hückel*. 2021. URL: <https://chem.libretexts.org/@go/page/1972> (cit. on pp. 40, 51).
- [29] *Semi Empirical*. URL: <https://docs.quantumatk.com/manual/SE.html> (cit. on p. 42).
- [30] M. Elstner, D. Porezag, G. Jungnickel, J. Elsner, M. Haugk, Th. Frauenheima, S. Suhai, and G. Seifert. «Self-consistent-charge density-functional tight-binding method for simulations of complex materials properties». In: *Physical review B*, vol. 58, number 11 (1998), pp. 7260–7268. DOI: 10.1103/PhysRevB.58.7260 (cit. on p. 42).
- [31] Matthias Hofmann and Henry F. Schaefer. «Computational Chemistry». In: *Encyclopedia of Physical Science and Technology (Third Edition)*. Ed. by Robert A. Meyers. Academic Press, 2003, pp. 487–506. DOI: 10.1016/B0-12-227410-5/00129-0 (cit. on p. 45).
- [32] *Pseudopotentials and basis sets available in QuantumATK*. URL: [https://docs.quantumatk.com/manual/technicalnotes/atk\\_pseudo\\_basis/atk\\_pseudo\\_basis.html](https://docs.quantumatk.com/manual/technicalnotes/atk_pseudo_basis/atk_pseudo_basis.html) (cit. on pp. 45, 46).
- [33] L. Vitos, J. Kollar, and H.L. Skrivera. «Local density approximation versus generalized gradient approximation: full charge density study of the atomic volume of the light actinides». In: *Journal of Alloys and Compounds* 271–273 (1998), pp. 339–341. DOI: 10.1016/S0925-8388(98)00084-X (cit. on p. 46).
- [34] *DFT-D2*. URL: <https://www.vasp.at/wiki/index.php/DFT-D2> (cit. on p. 46).

- [35] *DFT-D3*. URL: <https://www.vasp.at/wiki/index.php/DFT-D3> (cit. on p. 46).
- [36] Serge I. Gorelsky. «Ab initio and Semiempirical Methods». In: *Encyclopedia of Inorganic and Bioinorganic Chemistry* (2011), pp. 1–12. DOI: 10.1002/9781119951438.eibc0377 (cit. on p. 47).
- [37] P.G. Jambrina and J. Aldegunde. «Computational Tools for the Study of Biomolecules». In: *Tools For Chemical Product Design*. Ed. by Mariano Martín, Mario R. Eden, and Nishanth G. Chemmangattuvalappil. Elsevier, 2016. Chap. 20, pp. 583–648 (cit. on p. 47).
- [38] Supriyo Datta. *Quantum Transport: Atom to Transistor*. Cambridge University Press, 2005. ISBN: 9780521631457 (cit. on pp. 49, 62).
- [39] *Poisson solvers*. URL: [https://docs.quantumatk.com/manual/technicalnotes/poisson\\_solvers/poisson\\_solvers.html](https://docs.quantumatk.com/manual/technicalnotes/poisson_solvers/poisson_solvers.html) (cit. on p. 65).
- [40] R. C. Haddon. «The fullerenes: powerful carbon-based electron acceptors». In: *The Royal Society Publishing*, Volume 343, Issue 1667 (Apr. 1993). DOI: 10.1098/rsta.1993.0040 (cit. on p. 66).
- [41] D. R.M. Walton and . Harold W. Kroto. *Fullerene*. Mar. 2019. URL: <https://www.britannica.com/science/fullerene> (cit. on p. 66).
- [42] H. W. Kroto. «The stability of the fullerenes C<sub>n</sub>, with n=24, 28, 32, 36, 50, 60 and 70». In: *Nature* 329 (Oct. 1987), pp. 529–531. DOI: 10.1038/329529a0 (cit. on p. 67).
- [43] E. Albertazzi, C. Domene, P. W. Fowler, T. Heine, G. Seifert, C. Van Alsenoyd, and F. Zerbettoe. «Pentagon adjacency as a determinant of fullerene stability». In: *Phys. Chem. Chem. Phys.* 1 (1999), pp. 2913–2918. DOI: 10.1039/A901600G (cit. on p. 67).
- [44] Jan M.L. Martin. «C<sub>28</sub>: the smallest stable fullerene?» In: *Chemical Physics Letters*, volume 255 (Mar. 1996), pp. 1–6. DOI: 10.1016/0009-2614(96)00354-5 (cit. on pp. 67, 68).
- [45] I. V. Davydov, A. I. Podlivaev, and L. A. Openov. «Anomalous Thermal Stability of Metastable C<sub>20</sub> Fullerene». In: *Physics of the Solid State*, volume 47 (Apr. 2005), pp. 778–784. DOI: 10.1134/1.1913997 (cit. on p. 67).
- [46] Horst Prinzbach, Andreas Weiler, and Peter Landenberger et al. «Gas-phase production and photoelectron spectroscopy of the smallest fullerene, C<sub>20</sub>». In: *Nature* 407 (Sept. 2000), pp. 60–63. DOI: 10.1038/35024037 (cit. on p. 67).
- [47] Jie An, Li-Hua Gan, Jian-Qiang Zhao, and Rui Li. «A global search for the lowest energy isomer of C<sub>26</sub>». In: *The journal of chemical physics*, volume 132 (Apr. 2010). DOI: 10.1063/1.3364801 (cit. on p. 67).

- [48] Stefan Portmann, John M. Galbraith, Henry F. Schaefer, Gustavo E. Scuseria, and Hans Peter Lüthi. «Some new structures of  $C_{28}$ ». In: *Chemical Physics Letters* 301, issues 1-2 (Dec. 1999), pp. 98–104. DOI: 10.1016/S0009-2614(98)01435-3 (cit. on pp. 67, 68).
- [49] Shu-Wei Tang, Ying-Fei Chang, Li-Li Sun, Hao Sun, Zhong-Min Su, and Rong-Shun Wang. «Stabilities, Electronic Properties of Exohedral Fluorine and Trifluoromethyl Derivatives for  $T_d$   $C_{28}$  Fullerene  $C_{28}F_{4-n}(CF_3)_n$  ( $n = 0,1,2,3,4$ )». In: *International Journal of Quantum Chemistry*, volume 108, issue 8 (Feb. 2008), pp. 1391–1398. DOI: 10.1002/qua.21630 (cit. on pp. 68, 85).
- [50] Rama K. Mishra, Ying-Ting Lin, and Shyi-Long Lee. «Theoretical studies of the fullerene growth mechanism: Ring-collapse model to  $C_{28}$  and cascade bond formation». In: *The journal of chemical physics*, volume 112 (Apr. 2000), pp. 6355–6364. DOI: 10.1063/1.481196 (cit. on p. 68).
- [51] Rama K. Mishra, Ying-Ting Lin, and Shyi-Long Lee. «Growth mechanism of  $C_{28}$   $T_d$  fullerene: energetics and transition-state structures analysis». In: *Chemical Physics Letters* 313, issue 3-4 (Nov. 1999), pp. 437–444. DOI: 10.1016/S0009-2614(99)01023-4 (cit. on p. 68).
- [52] Rama K. Mishra, Ying-Ting Lin, and Shyi-Long Lee. « $C_{28}$  ( $D_2$ ): Fullerene Growth Mechanism». In: *International Journal of Quantum Chemistry*, volume 84, issue 6 (Aug. 2001), pp. 642–648. DOI: 10.1002/QUA.1419 (cit. on p. 68).
- [53] Gotthard Seifert, Andrey N. Enyashin, and Thomas Heine. «Solid-State Structures of Small Fullerenes». In: *Handbook of Nanophysics*. Jan. 2011, pp. 1–13. DOI: 10.1201/9781420075557-35 (cit. on p. 68).
- [54] Rupan Preet Kaur, Ravinder Singh Sawhney, and Derick Engles. «Electrical characterization of  $C_{28}$  fullerene junctions formed with group 1B metal electrodes». In: *Journal of Molecular Graphics and Modelling*, volume 79 (July 2017), pp. 296–304. DOI: 10.1016/j.jmgm.2017.07.018 (cit. on pp. 69, 75).
- [55] Ke Xu, Jing Huang, Zhaoyong Guan, Qunxiang Li, and Jinlong Yang. «Transport spin polarization of magnetic  $C_{28}$  molecular junctions». In: *Chemical Physics Letters*, volume 535 (2012), pp. 111–115 (cit. on pp. 69, 76–78).
- [56] Sayantanu Koleya, Sabyasachi Senb, and Swapan Chakrabartia. «Role of molecule-electrode coupling strength in inducing inelastic transmission spectra of  $Hf@C_{28}$ ». In: *Chemical physics* 539 (Nov. 2020). DOI: 10.1016/j.chemphys.2020.110930 (cit. on p. 69).
- [57] A.Pahuja and S.Srivastava. «Electronic Transport Properties of Doped  $C_{28}$  Fullerene». In: *Physics Research International* 2014 (Nov. 2014), pp. 1–7. DOI: 10.1155/2014/872381 (cit. on pp. 69, 75).

- [58] Ke Xu, Tie Yang, Yu Feng, Xin Ruan, Zhenyan Liu, Guijie Liang, and Xiaotian Wang. «Endohedral Fullerene Fe@C<sub>28</sub> Adsorbed on Au(111) Surface as a High-Efficiency Spin Filter: A Theoretical Study». In: *Nanomaterials*, volume 9, number 1068 (2019). DOI: 10.3390/nano9081068 (cit. on pp. 69, 72, 75).
- [59] Matthias Thommes, Katsumi Kaneko, Alexander V. Neimark, James P. Olivier, Francisco Rodriguez-Reinoso, Jean Rouquerol, and Kenneth S. W. Sing. «Physisorption of gases, with special reference to the evaluation of surface area and pore size distribution (IUPAC Technical Report)». In: *Pure Appl. Chem.*, volume 87, number 9-10 (2015), pp. 1051–1069. DOI: 10.1515/pac-2014-1117 (cit. on p. 71).
- [60] Fang Deng, Xu-Biao Luo, Lin Ding, and Sheng-Lian Luo. «Application of Nanomaterials and Nanotechnology in the Reutilization of Metal Ion from Wastewater». In: *Nanomaterials for the Removal of Pollutants and Resource Reutilization* (2019), pp. 149–178. URL: <https://doi.org/10.1016/B978-0-12-814837-2.00005-6> (cit. on p. 71).
- [61] *Adsorption*. URL: <https://www.britannica.com/science/adsorption> (cit. on p. 71).
- [62] Hong-Tao Liu, Xiao-Gen Xiong, Phuong Diem Dau, Yi-Lei Wang, Dao-Ling Huang, Jun Li, and Lai-Sheng Wang. «Probing the nature of gold–carbon bonding in gold–alkynyl complexes». In: *Nature communications* 4, number 2223 (June 2013), pp. 1–8. DOI: 10.1038/ncomms3223 (cit. on pp. 72, 75).
- [63] Nadja Sandig and Francesco Zerbetto. «Molecules on gold». In: *Chem. Commun.*, 46 (2010), pp. 667–676. DOI: DOI:10.1039/b915580e (cit. on p. 72).
- [64] Shundong Yuan, Chunlei Dai, Jiena Weng, Qunbo Mei, Qidan Ling, Lianhui Wang, and Wei Huang. «Theoretical Studies of Electron Transport in Thiophene Dimer: Effects of Substituent Group and Heteroatom». In: *J. Phys. Chem. A*, volume 115, number 17 (2011), pp. 4535–4546. DOI: DOI: 10.1021/JP201038F (cit. on p. 74).
- [65] Shundong Yuan, Shiyang Wang, Qunbo Mei, Qidan Ling, Lianhui Wang, and Wei Huang. «First-Principles Study of Rectification in Bis-2(5-ethynylthienyl) ethyne Molecular Junctions». In: *J. Phys. Chem. A*, volume 115, number 32 (2011), pp. 9033–9042. DOI: DOI:10.1021/JP204161Z (cit. on p. 74).
- [66] Vu Thi Thu Huong, Truong Ba Tai, Jyh-Chiang Jiang, and Minh Tho Nguyen. «Spin-polarized transport properties in some transition metal dithiolene complexes». In: *Physical Chemistry Chemical Physics*, 19, issue 48 (2017), pp. 32536–32543. DOI: DOI:10.1039/C7CP05962K (cit. on p. 74).
- [67] *Why are so many k-points needed in the transport direction in a device calculation?* URL: [https://docs.quantumatk.com/tutorials/transport\\_kpoints/transport\\_kpoints.html](https://docs.quantumatk.com/tutorials/transport_kpoints/transport_kpoints.html) (cit. on p. 80).

- [68] E. Glueckauf. «The composition of atmospheric air». In: *Compendium of Meteorology*, 3–10 (1951). DOI: doi:10.1007/978-1-940033-70-9\_1 (cit. on p. 84).
- [69] Kenneth B. Wiberg and Paul R. Rablen. «Atomic Charges». In: *The Journal of Organic Chemistry*, volume 83, number 24 (2018), pp. 15463–15469. DOI: 10.1021/acs.joc.8b02740 (cit. on p. 85).
- [70] J. Cioslowski, P. J. Hay, and J. P. Ritchie. «Charge Distributions and Effective Atomic Charges in Transition-Metal Complexes Using Generalized Atomic Polar Tensors and Topological Analysis». In: *J. Phys. Chem.*, 94 (1990), pp. 148–151. DOI: 10.1021/j100364a022 (cit. on p. 85).
- [71] R.G. Keil and L.M. Mayer. «12.12 - Mineral Matrices and Organic Matter». In: *Treatise on Geochemistry (Second Edition)*. Ed. by Heinrich D. Holland and Karl K. Turekian. Second Edition. Elsevier, 2014, pp. 337–359. DOI: 10.1016/B978-0-08-095975-7.01024-X (cit. on p. 86).
- [72] *TransmissionEigenvalues*. URL: <https://docs.quantumatk.com/manual/Types/TransmissionEigenvalues/TransmissionEigenvalues.html#transmissioneigenvalues-c> (cit. on p. 95).
- [73] *Steric Effect*. URL: [https://doi.org/10.1007/978-3-642-11274-4\\_1517](https://doi.org/10.1007/978-3-642-11274-4_1517) (cit. on p. 100).
- [74] *Carbon monoxide*. URL: <https://pubchem.ncbi.nlm.nih.gov/compound/Carbon-monoxide#section=RTECS-Number> (cit. on p. 101).
- [75] *Sources of Nitrogen Oxides*. URL: [https://chem.libretexts.org/Bookshelves/Environmental\\_Chemistry/Supplemental\\_Modules\\_\(Environmental\\_Chemistry\)/Acid\\_Rain/Sources\\_of\\_Nitrogen\\_Oxides](https://chem.libretexts.org/Bookshelves/Environmental_Chemistry/Supplemental_Modules_(Environmental_Chemistry)/Acid_Rain/Sources_of_Nitrogen_Oxides) (cit. on p. 102).
- [76] *Nitric oxide*. URL: <https://pubchem.ncbi.nlm.nih.gov/compound/Nitric-oxide> (cit. on p. 102).
- [77] *Nitrogen Dioxide (NO<sub>2</sub>) Pollution*. URL: <https://www.epa.gov/no2-pollution/basic-information-about-no2#WhatIsNO2> (cit. on p. 103).
- [78] *Nitrogen dioxide*. URL: <https://pubchem.ncbi.nlm.nih.gov/compound/Nitrogen-dioxide> (cit. on p. 103).
- [79] *Sulfur dioxide*. URL: <https://pubchem.ncbi.nlm.nih.gov/compound/Sulfur-dioxide> (cit. on p. 104).
- [80] Sailesh N. Behera, Mukesh Sharma, Viney P. Aneja, and Rajasekhar Balasubramanian. «Ammonia in the atmosphere: a review on emission sources, atmospheric chemistry and deposition on terrestrial bodies». In: *Environmental Science and Pollution Research* volume 20 (20142013), pp. 8092–8131. DOI: <https://doi.org/10.1007/s11356-013-2051-9> (cit. on p. 104).

## BIBLIOGRAPHY

---

- [81] L. M. Tormoehlen, K. J. Tekulve, and K. A. Nañagas. «Hydrocarbon toxicity: A review». In: *Clinical Toxicology*, 52(5) (2014), pp. 479–489. DOI: 10.3109/15563650.2014.923904 (cit. on p. 105).
- [82] *Importance of Methane*. URL: <https://www.epa.gov/gmi/importance-methane> (cit. on p. 105).
- [83] *Facts About Benzene*. URL: <https://emergency.cdc.gov/agent/benzene/basics/facts.asp> (cit. on p. 105).
- [84] *Toluene (methylbenzene)*. URL: <http://www.npi.gov.au/resource/toluene-methylbenzene> (cit. on p. 105).
- [85] R. M. Harrison, Laxen, and D. P. H. «Lead in the atmosphere». In: *Lead Pollution: Causes and control*. 1981, pp. 7–32. DOI: 10.1007/978-94-009-5830-2\_2 (cit. on p. 106).
- [86] *Basic Information about Lead Air Pollution*. URL: <https://www.epa.gov/lead-air-pollution/basic-information-about-lead-air-pollution> (cit. on p. 107).